



**University of Bremen**

**The functional Role of Gamma-Band  
Synchronization in selective Routing and Network  
Configuration within the visual Cortex**

---

A thesis submitted to obtain the degree  
Doctor of Natural Sciences (Dr. rer. nat.),

submitted by  
Eric Drebitz M.Sc.

to the Department of Biology and Chemistry at the  
University of Bremen

Bremen, October 2019

Gutachter: Prof. Dr. Andreas K. Kreiter

Prof. Dr. Michael Koch

Dissertationskolloquium: 29.11.2019

## **ERKLÄRUNG**

Hiermit erkläre ich, dass ich die Doktorarbeit mit dem Titel:

**The functional Role of Gamma-Band Synchronization in selective Routing and Network Configuration within the visual Cortex**

selbstständig verfasst und geschrieben habe und außer den angegebenen Quellen keine weiteren Hilfsmittel verwendet habe.

Ebenfalls erkläre ich hiermit, dass es sich bei den von mir abgegebenen Arbeiten um drei identische Exemplare handelt.

---

Eric Drebitz

## Publication List

Below articles and posters are listed that have arisen from my work in the course of my Ph.D. period. The present cumulative thesis is based upon those manuscripts labeled by an asterisk (\*).

### Scientific articles:

- \* **Drebitz, E.**, Haag, M., Grothe, I., Mandon S., Kreiter A.K. Attention configures synchronization within local neuronal networks for processing of the behaviorally relevant stimulus. *Front. Neural Circuits*. Published August 2018
- \* **Drebitz, E.**, Schledde, B., Kreiter A.K., Wegener D. Optimizing the Yield of Multi-Unit Activity by Including the Entire Spiking Activity. *Front. Neuroscience*. Published February 2019
- \* **Drebitz, E.**, Rausch L-P, Kreiter A.K. A novel approach for removing micro-stimulation artifacts and reconstruction of broad-band neuronal signals. *Journal of Neuroscience Methods* (under review)
- \* **Drebitz, E.**, Rausch, L-P., Kreiter A.K. Signal transmission between monkey areas V2 and V4 is causally dependent on phase synchronization. (in preparation)

### Scientific Posters

**Drebitz E**, Haag M., Grothe I., Mandon S., Kreiter A.K. Attention Dependent Gamma-Band Synchronization as a dynamic Mechanism for local Network Configuration in Monkey Area V4. 11th FENS Forum, Berlin, Germany (2018).

Rausch L-P., Harnack D., **Drebitz E.**, Ernst U., Kreiter A.K. Facilitatory and suppressive effects of selective spatial attention on neuronal stimulus representation in V2 of the macaque monkey. The 11th Primate Neurobiology Meeting. Tübingen, Germany (2018)

**Drebitz E.**, Rausch L-P., Stemmann H., Kreiter A.K. Signal transmission between monkey areas V2 and V4 is causally dependent on phase synchronization. 13th Meeting of the German Neuroscience Society, Göttingen, Germany (2017)

Lisitsyn, D., **Drebitz, E.**, Grothe, I. et al. Dissecting gamma phase and amplitude-specific information routing in V4 of macaque during selective attention. *BMC Neurosci* (2017) 18(Suppl 1): 014. 26th Annual Computational Neuroscience Meeting. Antwerp, Belgium. <https://doi.org/10.1186/s12868-017-0370-3>

**Drebitz E.**, Rausch L-P., Stemmann H., Kreiter A.K., (2017). Effectiveness of electrically evoked input depends on the gamma-phase of the receiving population in monkey area V4. *Cosyne Abstracts 2017*, Salt Lake City, UT, USA.

**Drebitz E**, Rausch L-P., Stemmann H., Kreiter A.K Behavioral effects of electrical stimulation in monkey visual cortex depends on the phase of gamma-band activity. 10th FENS Forum, Copenhagen, Denmark (2016).

**Drebitz, E.** Haag M., Grothe I., Mandon, S., Kreiter A.K. Attentional Modulation of Phase Coupling in V4 as dynamic Mechanism for Selective Information Processing and Routing. 11th Meeting of the German Neuroscience Society, Göttingen, Germany (2015)

**[Drebitz E.**, Schledde B., Wegener D., Kreiter A.K.]. [Mapping RFs from chronically recorded low-

SNR signals in monkey visual cortex]. Program No. 60.28. 2014 Neuroscience Meeting Planner. Washington, DC: Society for Neuroscience, (2014).

Gordillo González V., Wegener D., **Drebitz E.**, Galashan F.O., Kreiter AK. A new and effective procedure for mapping monkey V1 receptive fields built on induced responses. European Conference on Perception (2013), Bremen, Germany.

# Contents

<b>Abstract .....</b>	<b>1</b>
<b>Zusammenfassung.....</b>	<b>3</b>
<b>Introduction.....</b>	<b>5</b>
1.1 General Introduction.....	5
1.2 The Visual Cortex .....	6
1.3 Concepts of attention.....	10
1.4 Neuronal correlates of attention .....	12
1.5 Concepts of attention-dependent routing.....	13
1.5.1 The normalization model of attention .....	14
1.5.2 Balanced excitation and inhibition model .....	16
1.5.3 Routing by Synchrony.....	17
<b>Chapter 2 .....</b>	<b>22</b>
2.1 Signal transmission between monkey areas V2 and V4 is causally dependent on gamma phase synchronization .....	22
2.2 Materials and Methods .....	29
2.3 Supplements .....	35
<b>Chapter 3 .....</b>	<b>37</b>
3.1 Attention Configures Synchronization within Local Neuronal Networks for Processing of the Behaviorally Relevant Stimulus.....	37
3.1.1 Abstract .....	38
3.1.2 Introduction .....	39
3.1.3 Materials and Methods .....	40
3.1.4 Results .....	48
3.1.5 Discussion .....	59
3.1.6 Conclusion.....	62
3.1.7 Author Contributions.....	63
3.1.8 Funding.....	63
3.1.9 Acknowledgments .....	63
3.2 Supplements.....	64
<b>Chapter 4 .....</b>	<b>66</b>
4.1 Optimizing the Yield of Multi-Unit Activity by Including the Entire Spiking Activity .....	66

4.1.1 Abstract .....	67
4.1.2 Introduction .....	68
4.1.3 Materials and Methods .....	70
4.1.4 Results .....	75
4.1.5 Discussion .....	81
4.1.6 Author Contributions.....	84
4.1.7 Funding.....	85
4.1.8 Acknowledgments .....	85
<b>Chapter 5 .....</b>	<b>86</b>
5.1 A novel approach for removing micro-stimulation artifacts and reconstruction of broad-band neuronal signals.....	86
5.1.1 Abstract .....	87
5.1.2 Introduction .....	88
5.1.3 Materials and Methods .....	90
5.1.4 Results .....	98
5.1.5 Discussion .....	103
5.1.6 Acknowledgments .....	106
<b>General Discussion .....</b>	<b>107</b>
<b>Acknowledgments .....</b>	<b>113</b>
<b>Bibliography .....</b>	<b>115</b>
<b>Supplementary Materials and Methods .....</b>	<b>134</b>
Implantation and Development of Recording Chamber.....	135
Recording procedure and experimental design .....	141

## Abstract

First psychophysical experiments performed more than 100 years ago by the German psychologist and physicist Hermann von Helmholtz<sup>1,2</sup>, showed that visual attention is a central component of perception and, therefore, of substantial relevance for successful behavior<sup>3</sup>. In the decades that followed, much research has been performed to investigate how attention modulates neuronal activity in order to explain the effects of attention on behavior and perception<sup>4</sup>. A well-described finding is that visual neurons responding to the same attended object synchronize their activity in the gamma ( $\gamma$ ) -frequency range (30 – 100 Hz)<sup>5</sup>.

In chapter 2, I present the results of an experiment that was designed to find evidence for a causal role of  $\gamma$ -band synchronization in selective information routing and processing. The underlying idea is that neurons, which synchronize their activity deliver their respective outputs (spikes) more precisely at times the receiving neuron is sensitive for it, i.e. the incoming spikes are more likely to evoke spikes of the receiving neuron<sup>6</sup>. The selective synchronization between input and receiver neurons representing an attended and therefore relevant object could constitute a powerful selection mechanism. To test this I recorded neuronal activity in area V4 of two macaque monkeys while applying single electrical pulses to neurons located in area V2. Those V2 neurons delivered afferent input to the recorded V4 population, including the electrically evoked spikes. By relating the effects of these electrically evoked spikes to the  $\gamma$ -oscillation in V4, I could show that the impact of stimulation on behavior and neuronal activity is causally dependent on the  $\gamma$ -phase.

In chapter 3, I investigated whether the effective processing of a given object requires a specific level of  $\gamma$ -band synchronization within a local neuronal population. I hypothesized that different objects require different combinations of neurons of the same population to be functionally coupled with one another for effective processing. Furthermore, we hypothesized that this dynamic establishment of functional connections is implemented by  $\gamma$ -band synchronization, resulting in a specific level of  $\gamma$ -band synchronization for a specific stimulus. I tested these predictions by first recording neuronal activity in area V4 and quantifying the level of  $\gamma$ -synchronization in response to two different single stimuli, which had to be attended. Second, I compared these levels to the level of  $\gamma$ -synchronization when neurons received input of both stimuli simultaneously, and one of them was attended. The level of  $\gamma$ -synchronization was almost “as if” the attended stimulus was presented alone, strongly indicating that the processing of this stimulus requires this specific  $\gamma$ -synchronization level.

## Abstract

Chapter 4 describes and characterizes a method that I used for analyzing multi-unit activity in area V4. It does not rely on setting up an amplitude-threshold for separating spikes from background noise as standard procedures do. Thus, this measure takes the entire spike activity into account, which I, therefore, refer to as ESA. I used semi-chronically recorded data of five macaque monkeys in order to quantify the sensitivity of the ESA to detect neuronal responses. The ESA-signal was significantly more sensitive than the standard procedures, especially for data with low signal-to-noise ratio, but preserves information about receptive field sizes and orientation selectivity of the underlying neuronal population.

The fifth chapter is describing a method for offline stimulation-artifact removal and restoration of the original broadband neuronal signal. I could show that in contrast to existing methods the here described procedure does not disturb the original signal and therefore allows for analysis of neuronal activity even shortly after electrical stimulation.

In summary, the results presented here give further insight into the functional roles of  $\gamma$ -band synchronization. I could show that (1)  $\gamma$ -phase synchronization plays a causal role in selective information processing and routing, and (2) that a specific pattern of intra-areal  $\gamma$ -synchronization is required for effective processing of a given stimulus.

## Zusammenfassung

Erste psychophysische Experimente des deutschen Psychologen und Physikers Hermann von Helmholtz zeigten bereits vor 100 Jahren das visuelle Aufmerksamkeit ein zentraler Bestandteil der Wahrnehmung ist<sup>1,2</sup> und daher von substantieller Bedeutung für erfolgreiches Verhalten ist<sup>3</sup>. In den darauffolgenden Dekaden wurde viel daran geforscht wie Aufmerksamkeit sich auf die neuronalen Aktivitätsmuster auswirkt, um die Effekte von Aufmerksamkeit in Bezug auf Verhalten und Wahrnehmung erklären zu können<sup>4</sup>. Ein gut beschriebenes Ergebnis ist, dass visuelle Neurone, welche auf das gleiche attendierte (mit Aufmerksamkeit belegte) Objekt antworten, ihre Aktivität im Gamma ( $\gamma$ ) Frequenzband synchronisieren<sup>5</sup>.

In Kapitel 2 zeige ich Ergebnisse eines Experiments, welches entworfen wurde um den kausalen Nachweis einer funktionalen Rolle von  $\gamma$ -Band Synchronisation für die selektive Informationsweiterleitung und Verarbeitung zu erbringen. Die dem zugrunde liegende Idee war, dass Neurone welche ihre Aktivität synchronisieren ihre jeweiligen Aktionspotentiale (APs) präziser zu Zeitpunkten generieren, an denen das empfangende Neuron sensitiv dafür ist. Das bedeutet, dass die Wahrscheinlichkeit einlaufender APs ein AP im empfangenden Neuron auszulösen höher ist<sup>6</sup>. Die selektive Synchronisation zwischen Input- und empfangenden Neuronen, welche ein attendiertes und dementsprechend relevantes Objekt repräsentieren, könnte daher einen leistungsfähigen Selektionsmechanismus darstellen. Um dies zu testen habe ich die neuronale Aktivität in Areal V4 zweier Makaken gemessen, während Neurone in Areal V2 mit einzelnen elektrischen Pulsen stimuliert wurden. Diese V2 Neurone lieferten APs als Input an die aufgenommenen Neurone in V4, dementsprechend auch die elektrisch generierten APs. Durch Verknüpfung der Auswirkung dieser elektrisch evozierten APs zur jeweiligen Phase der  $\gamma$ -Oszillation in V4, konnte ich zeigen, dass die Effekte der Stimulation auf Verhalten und neuronale Aktivität kausal von der  $\gamma$ -Phase abhängt.

In Kapitel 3 untersuche ich ob das effektive Verarbeiten eines gegebenen Objektes einen spezifischen Grad an  $\gamma$ -Band Synchronisation innerhalb einer lokalen neuronalen Population benötigt. Unsere Hypothese war, dass verschiedene Objekte jeweils andere Kombinationen von funktional verbundenen Neuronen benötigen, um effizient verarbeitet werden zu können. Die Hypothese besagte des Weiteren, dass diese dynamische Etablierung spezifischer funktionaler Verbindungen durch  $\gamma$ -Band Synchronisation erzeugt wird, was zu einem objektspezifischen Grad an  $\gamma$ -Band Synchronisation führen würde. Ich habe diese Vorhersage getestet, indem ich zunächst die neuronale Aktivität in Areal V4 gemessen habe und den Grad der  $\gamma$ -Synchronisation als Antwort auf zwei unterschiedliche Einzelreize quantifiziert habe.

## Zusammenfassung

Daraufhin habe diesen Grad an Synchronisation verglichen mit dem Grad an Synchronisation wenn beide Reize gleichzeitig gezeigt wurden und jeweils einer davon attendiert war. Der Grad an Synchronisation war fast „als ob“ nur der attendierte Reiz gezeigt wurde, was stark darauf hinweist, dass das Verarbeiten dieses Reizes dieses spezifische Niveau an  $\gamma$ -Synchronisation benötigt.

Kapitel 4 beschreibt und charakterisiert eine Methode welche ich zur Analyse der APs multipler Neurone (Multi-Unit Activity) in Areal V4 genutzt habe. Diese Methode benötigt im Gegensatz zu Standardmethoden keinen Schwellenwert welcher von APs überschritten werden muss, um diese vom Hintergrundrauschen zu separieren. Aus diesem Grund bezieht diese Methode alle generierten APs mit ein, weshalb ich sie ESA (Entire Spiking Activity) benannt habe. Zur Quantifizierung der Sensitivität von ESA bei der Detektion neuronaler Antworten habe ich Daten von fünf Makaken genutzt, welche unter semi-chronischen Bedingung aufgenommen wurden. Die Analyse zeigte, dass das ESA-signal deutlich sensitiver als Standardmethoden ist, insbesondere bei Daten mit kleinem Signal zu Rausch Verhältnis, jedoch erhält es die Informationen über rezeptive Feldgrößen oder Orientierungsselektivität der zugrundeliegenden neuronalen Population.

Das fünfte Kapitel beschreibt eine Methode zur Entfernung von Stimulationsartefakten und Wiederherstellung des originalen neuronalen Breitbandsignals. Ich konnte zeigen das im Gegensatz zu existierenden Methoden, die hier beschriebene Methode das Originalsignal nicht verzerrt und es daher erlaubt neuronale Aktivität schon kurz nach einer elektrischen Stimulation zu analysieren.

Zusammengefasst geben die vorgestellten Resultate weitem Einblick in die funktionalen Rollen von  $\gamma$ -Band Synchronisation. Ich konnte zeigen, dass (1)  $\gamma$ -Phasen Synchronisation eine kausale Rolle für die selektive Informationsverarbeitung und Weiterleitung spielt und (2), dass ein spezifisches Muster intraarealer  $\gamma$ -Synchronisation notwendig ist um einen gegebenen Reiz effektiv zu verarbeiten.

## Introduction

### 1.1 General Introduction

A strong motivation for my scientific work on selective information processing within the brain is that I experienced by myself quite frequently that our perception of the environment is modified and even fragmentary. It is adjusted by the brain for specific reasons, ranging from physiological constraints of the brain itself to improving the chances of surviving by highlighting relevant aspects while simultaneously suppressing distracting ones.

An impressive example of a difference between our percept and the actual physical surround is the so-called “Gorillas in our midst” paradigm by Simons and Chabris (1999)<sup>7</sup>. In this paradigm, subjects were asked to observe a movie scene on a screen. The scene contained two teams passing basketballs and moving around randomly. After a while, a person in a gorilla costume walks through the group of basketball players (Fig. 1). Observers were instructed before to

count mentally the number of passes of one of the teams or to count the number of aerial and bounce passes separately. The appearance of the gorilla was not mentioned to the observers. After the movie ended, people were asked to tell the results of their counting and besides whether they noticed something unusual during the movie scene. 64 % of the observers performing the easy task (counting passes of one team) saw the person in the gorilla costume crossing the scene, but only 45 % of the observers performing the more difficult task (counting aerial and bounce passes separately) perceived the crossing gorilla. This popular paradigm illustrates that we are surprisingly



**Figure 1:** A single frame of a movie sequence shown to observers. The frame was taken at the time when a person in a gorilla costume walked through the scene.

*Adapted and reprinted from: Perception, 28, Simons and Chabris: Gorillas in our midst: sustained inattention blindness for dynamic events (1999)<sup>7</sup>, with permission from SAGE Publications.*

unaware of details in our environment to which we pay no attention. In this specific example, the basketball was the relevant object, and observers paid attention to its location. Information about the surrounding, like the gorilla, also reached the retina and was transmitted further to the brain but did not become part of the observers’ percept. This vivid example depicts the psychophysical consequences of attention-dependent and selective information processing

## Introduction

within the brain. Hence, several questions regarding the neuronal implementation of such selective processing arise. For example, how is the relevant information regarding the basketball prioritized in comparison to information representing the irrelevant gorilla? In addition, why did observers performing the easy task detect the gorilla more often than observers performing the difficult task although all of them saw the same movie scene? There are many other interesting questions which one can derive from this experiment, but the ones mentioned are closely related to my scientific work and hence to this thesis.

The scientific work presented here revolves around the attention-dependent processing of relevant visual information on the neuronal level. To stay with the example, I was investigating neuronal mechanisms that might explain the selective processing of information regarding the basketball while information related to the gorilla is filtered out.

This thesis is divided into five main parts. The results of investigations on two different aspects of attention-dependent processing of visual information are presented in chapters 2 and 3. Chapters 4 and 5 deal with procedures developed for performing my research, introducing the respective areas of application, characteristics and potential constraints. In the following subchapters, I will give a detailed introduction into the visual system as well as the current state of scientific research regarding attention-dependent information processing, and based on that the objectives of my work.

### **1.2 The Visual Cortex**

In order to investigate neuronal mechanisms of attention-dependent processing of relevant information, I performed intra-cortical recordings in the visual cortex of macaque monkeys (*Macaca mulatta*). In the following, I will introduce the anatomical and functional structure of the macaque's visual system.

The visual system of primates is highly complex and build up by dozens of cortical and subcortical structures, forming a strongly interconnected processing network for the sensory input<sup>8-10</sup>. Visual information is translated into neuronal signals at the retinas, which deliver the output to four subcortical nuclei in parallel<sup>11</sup>. These nuclei are part of distinct networks with different functions such as eye movement<sup>12-14</sup> or the control of the circadian rhythm<sup>15</sup>. In the context of information processing within the visual cortex, the lateral geniculate nucleus (LGN,

## Introduction

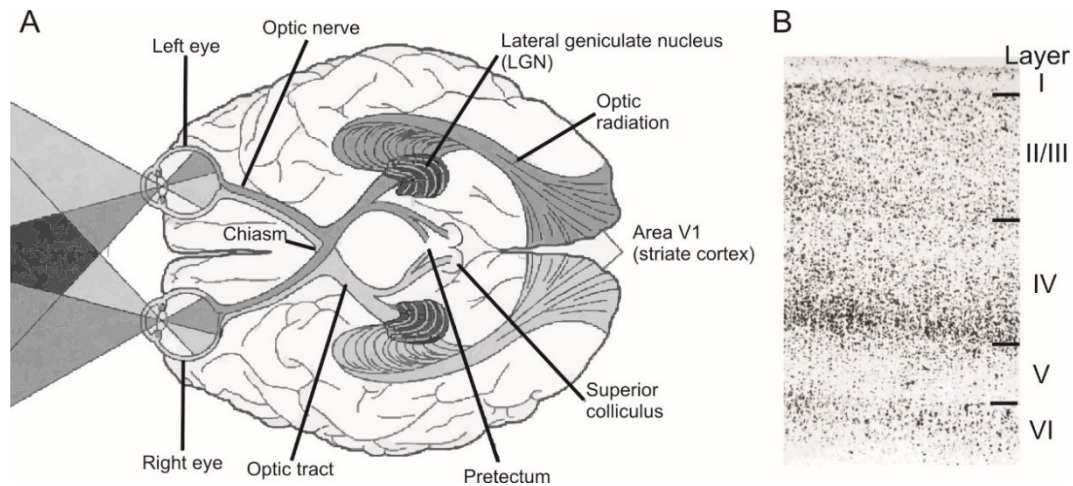


**Figure 2:** overview of the visual system and laminar structure of the cortex. **(A)** Schematic illustration of the human visual system from the retina to cortical area V1, seen from below. Adapted from and with permission of: Daw, N.W., 2006<sup>19</sup>: *Visual development; (Vol. 9)*. New York: Springer. **(B)** 40  $\mu$ m section of cortical area V1 of a macaque monkey in cresyl violet-stain. Layers are labeled by Roman numerals and vertical bars indicate their borders. Note that in area V1 layer IV is further divided into sub-layers IV A, IV B and IV C $\alpha$  and IV C $\beta$  (not shown here). These separation is unique for V1 and therefore not exemplarily for the laminar structure of the cortex in general. Adapted from and with permission of: Lund et al., 1997<sup>18</sup>: *Journal of Comparative Neurology* (384), John Wiley and Sons.

Fig. 2 A) is the most important retinal projection site since it is the “relay-station” to the visual cortex<sup>16</sup>. The main target of LGN projections is the first stage within the visual cortical processing hierarchy, namely area V1 or the striate cortex (Fig. 2A).

The visual cortex, as the cortex in general, is composed of six distinct layers (Fig. 2 B/ Fig. 3). The upstream input arrives mainly at neurons located in layer four (but also three, see Fig. 3), which in turn project to layers two and three of the same area<sup>17,18</sup> (Fig. 3, right: intrinsic connections). Neurons located in layers two and three provide the output to the following downstream areas of the processing pathway, but also back to layer four and layer five. Neurons located in layers five and six project back to subcortical regions such as the superior colliculus and the LGN. The actual connections between all neurons of the different layers are much more complex (as indicated by Fig. 3), but for an overview, this scheme is sufficient since it covers the main projections between cortical layers<sup>19-22</sup>. For this work, it is important to highlight, that neurons located in layers two and three deliver the main output to downstream cortical areas. This output arrives within layer four of the respective downstream areas.

Based on lesion studies in macaques and on human patients with partly damaged cortical tissue, it has been proposed that in cortical area V1, two anatomically and functionally distinct processing streams emerge. Namely, the dorsal and ventral processing streams, each of them comprising multiple visual areas<sup>23-26</sup>. The dorsal stream is associated with the processing of spatial information about objects (motion, speed, direction) and has therefore initially been

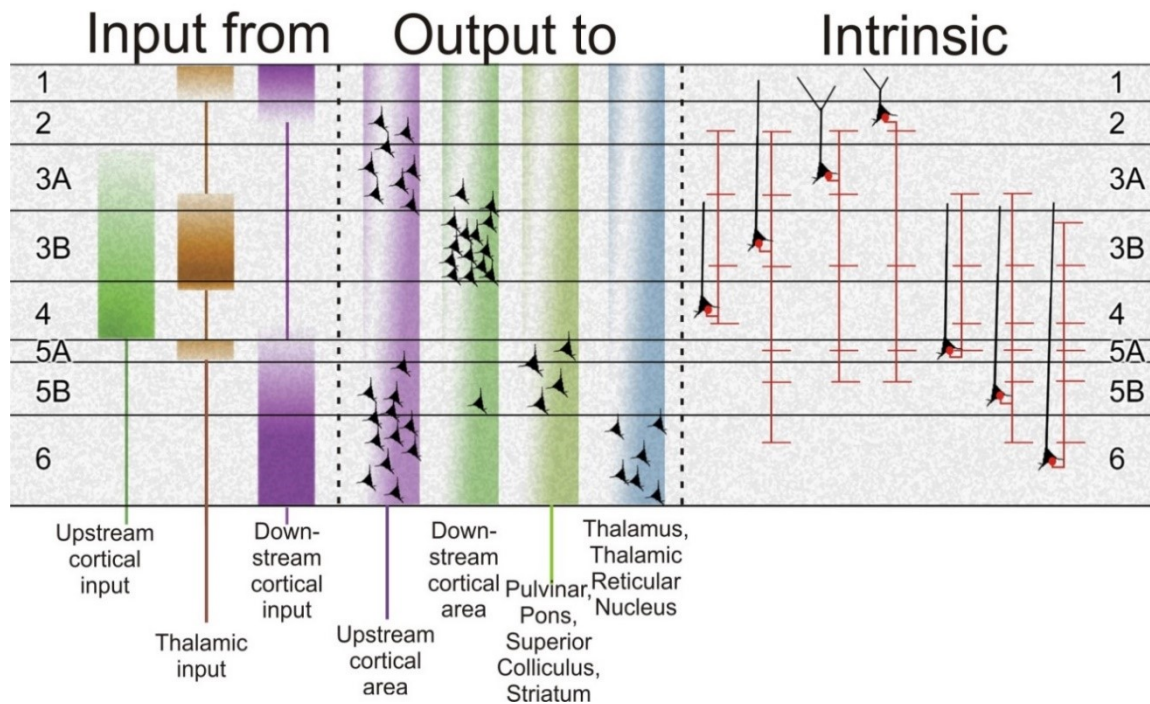


**Figure 3:** Connection scheme of excitatory neurons within a generic (not V1) visual cortical area of a primate. The inputs of the excitatory cells located within the six different layers and their origin is shown on the left. The outputs are shown in the middle part. The cell somas represent the connection sites of laminar outputs. On the right, the intrinsic connections between excitatory neurons (illustrated by their soma) to other neurons within the same cortical column are shown (horizontal red bars). Reprinted from: *Current Biology*, 17/12, Shipp S: *Structure and function of the cerebral cortex*, p: R445, © 2007, with permission from Elsevier<sup>22</sup>.

named “where” stream. This designation later changed to “how” stream, since its primary difference to the ventral stream is its relevance for visuomotor control<sup>25,27,28</sup>. The ventral– or “what” – stream is associated with object recognition by the processing of specific object features (orientation, color, brightness, curvature)<sup>23,24,28–32</sup>. A separation into parallel processing streams has been observed in different species of primates including humans<sup>29,33,34</sup>. The proposed strict functional distinction between both streams has been vigorously challenged in recent years. Several findings give evidence that areas located in the dorsal stream are also engaged in object recognition<sup>27,35,36</sup>, whereas areas of the ventral stream also deliver information about the size and position of objects<sup>37,38</sup>. Each of these attributes was assigned to the other processing stream before.

Besides, the more and more disputed strict functional distinction between processing streams, there are undisputed differences between both streams. It has been shown, for example, that the dorsal stream responds faster to visual stimulation than the ventral stream<sup>10,39,40</sup>, which is thought to reflect the different thalamocortical inputs to both streams<sup>28</sup>. The dorsal stream receives 95 % of its afferent inputs from the faster responding magnocellular layers of the LGN,

## Introduction

whereas the ventral stream receives inputs of a balanced combination of magno- and parvocellular layers. Most anatomical projections (90 %) culminating into the dorsal stream are routed through layers 4 C $\alpha$  and 4 B of area V1 (these layer classification is unique for V1 and therefore not illustrated in Fig. 2B and Fig. 3) directly to the middle temporal cortex (MT). The other afferents of MT originate in areas V2 and V3<sup>41-43</sup>. MT-neurons, in turn, deliver most afferent connections to downstream areas in the posterior parietal cortex. Thalamocortical projections to the ventral stream are also relayed via area V1 but arrive in layers 4 C $\beta$  and 4 A, which then project to area V2 (layer 4) and further downstream to area V4. Note here, that V4 neurons receive their primary afferent input from neurons located in area V2<sup>44,45</sup>, these projections are of particular interest for this work. V4 neurons then project downstream to inferior temporal cortex (IT)<sup>8,23,29,46</sup>.

A sequential routing and processing along both streams is, of course, a simplification. Recent studies showed that the connectivity pattern, especially for the ventral stream, resembles rather a highly interconnected network with several bypasses and other non-hierarchical patterns (for a review see Kravitz et al., 2014<sup>47</sup>). Nevertheless, both streams exhibit hierarchical characteristics. The response latencies, as well as the complexity of stimulus selectivity increases along both streams from low hierarchical levels (V1, V2) to middle- (V4, MT) and higher levels (MST, TEO)<sup>47-52</sup>. Furthermore, the area of the visual field to which neurons respond to (receptive field, RF) increases gradually from upstream to downstream stages of the hierarchy<sup>47,53</sup>. This increase enables complex processing at higher stages of the hierarchy since information of several stimulus features like color and orientation over a certain spatial area can be integrated. The increase of RF-sizes along the visual processing streams is implemented by convergent anatomical connections between downstream neurons and their afferent input neurons. More precise, several upstream neurons with small RFs deliver convergent input to the same downstream neurons, which therefore respond to a larger proportion of the visual space as the individual upstream neurons<sup>8,54</sup>.

This gradual increase of RF sizes induces one of the fundamental questions concerning information processing within the visual system: Since neurons at higher visual areas respond to larger proportions of the visual field, they will inevitably receive at one-point signals representing multiple independent objects. In the “Gorilla in our Midst” paradigm, this means neurons might receive signals representing the basketball, body parts of players, or even the man in the gorilla costume simultaneously. However, those simultaneously arriving signals cannot be processed and routed by individual neurons simultaneously<sup>55-57</sup>, which raises the question of how these neurons behave when confronted with multiple competing inputs. The

## Introduction

“Gorilla in our Midst” paradigm points to a mechanism, which seems to be involved in resolving this conflict. As mentioned before, when participants attended the basketball, they were able to solve the task efficiently, while often not detecting the man in the gorilla costume. These results indicate that the signals representing an attended object are processed and routed along the visual cortex, while the signals representing an unattended object are suppressed. However, how this attention-dependent selection of relevant information is implemented on the neuronal level is still under substantial debate and subject of my investigations.

### 1.3 Concepts of attention

My experience is what I agree to attend to.  
Only those items which I notice shape my mind.”

William James (1890)<sup>58</sup>

William James was an American philosopher and regarded as one of the cofounders of psychology as a scientific discipline in the USA<sup>59</sup>. He was also one of the first scientists stating that attention is an indispensable mechanism for navigating and interacting with our physical surround<sup>58</sup>. However, he based his statements and theories on introspection, meaning he described his own experiences without empirical or statistical evaluation. In contrast, Herman von Helmholtz performed psychophysical experiments with human subjects to investigate the influence of attention on perception. In one of his experiments, participants were asked to fixate a central fixation spot on a board in a dark room. There were also random letters written on that board, which were unrecognizable until the room was illuminated for a brief period. The participants had to hold fixation onto the central spot and simultaneously discriminate the letters written on the board. Von Helmholtz found that participants were able to discriminate those letters located at regions, which they covertly attended before the light was switched on. However, the spatial extent in which discrimination was possible was restricted, i.e. not all letters were discriminable<sup>60</sup>. These findings illustrate the link between attention and selective information processing. Besides this, Helmholtz is also considered to be the first investigating the effects of covert attention, i.e. attention is focused on a location that differs from the center of gaze<sup>4</sup>.

To avoid giving a false impression, nowadays the term attention is not understood as describing a single entity or single neuronal mechanism. It evolved as a collective term for different aspects

## Introduction

of biasing sensory selection for goal-directed behavior<sup>61</sup>. In general, attention is divided into endogenously- and exogenously controlled attention. Furthermore, endogenously controlled attention is further subdivided into either being intentionally or unintentionally deployed<sup>62</sup>.

As described above in the experiment of von Helmholtz in the late 19<sup>th</sup> century, attention can be directed intentionally (overtly and covertly) to a specific region within the visual field. This spatially limited mechanism was named spatial attention. Events or other stimulus-related characteristics located within the attended region can be detected faster, and the sensitivity for detecting a change increases<sup>63-65</sup>, the same holds, when attending a non-spatial feature (feature-based attention) of a stimulus such as color or shape<sup>66</sup>. In contrast to spatial attention, the feature-based mechanism works globally, such that all objects exhibiting the attended feature receive a positive selection bias, indicated for example by faster reaction- and detection times and the increased discriminability of these objects<sup>67,68</sup>. The third intentional mechanism is called object-based attention<sup>69</sup>. It is seen as a mechanism that enhances and integrates processing of all features of an attended object (color, motion, form) resulting in higher efficiency (faster reaction- detection times, higher accuracy) of behavior related to the attended object<sup>69-71</sup>.

These three intentional endogenous mechanisms are contrasted with unintentional endogenous mechanisms delivering selection biases based on unconscious probabilistic evaluations of stimulus and reward history<sup>62</sup>. Several studies showed that a stimulus that has been relevant in the past and delivered reward is processed more effectively than a novel stimulus without reward history<sup>72-76</sup>. This enhancement can even counteract intentional mechanisms<sup>77-79</sup>.

In contrast to the above-described endogenously controlled attention mechanisms, are exogenously controlled attentional mechanisms based on external, stimulus-driven characteristics. In this context, the term saliency is often used to characterize the degree an object differs in its feature space (color, shape, contrast, motion) from surrounding objects. An object with high saliency is processed preferentially and detection times are short, as compared to objects with low saliency<sup>80-82</sup>. This can best be illustrated using an example: A person observing the night sky will quickly recognize a shooting star, although the object itself is not larger or brighter than other objects in the sky. However, the fast movement makes the shooting star unique in that scene, which means it has a high saliency in comparison to the other objects. Another good example of exogenously controlled attention is a classical visual search task. In general the amount of time required to detect a specific target of unknown location increases linearly with the number of distractor objects presented simultaneously (display size effect)<sup>83,84</sup>. However, if the target object is briefly highlighted (e.g. fast increase and decrease in

luminance), detection times dramatically decrease, and participants easily recognize the target object, irrespective of the number of distractor objects on screen<sup>85</sup>.

### 1.4 Neuronal correlates of attention

The concepts above of visual attention have one thing in common: attention delivers a selection bias for the attended stimulus feature (location, color, object) or even feature dimension<sup>86</sup>, which results in faster RTs, increased sensitivity, or higher accuracy of subjects performing a task.

Over the past decades, many researchers addressed the question of how these psychophysical results are reflected in the visual system. A common finding at multiple stages of the visual processing pathways was that single neurons representing an object exhibiting an attended feature show an enhanced mean firing rate, as compared to when this feature was unattended<sup>87-92</sup>. This increase in firing rates improves the individual neurons signal-to-noise ratio (SNR)<sup>93,94</sup>. Other studies showed that the reliability of neuronal responses of individual neurons is enhanced by a decreased variance of firing rates<sup>86,95-97</sup>. The effect size of these improvements is modest, which makes it unlikely that they can account for the substantial attention-dependent improvements of performance alone<sup>98</sup>. Indeed Mitchell and colleagues (2009) stated that the attention-dependent increase of firing-rates accounts only for 9.5 % of the overall SNR improvement in their data<sup>96</sup>.

They also investigated the attention dependent reduction of correlated noise between neurons encoding an attended stimulus. The authors assumed this the main contributor to the overall SNR improvement. The idea behind is that for an upstream neuron the individual noise of afferent neurons cancels out over all of its inputs, whereas correlated noise, i.e. multiple neurons exhibiting the same noise pattern, does not and would thereby substantially decrease the input SNR<sup>98-100</sup>. The authors found indeed that the correlated low-frequency neuronal activity was significantly reduced when neurons represented an attended stimulus. The reduction was most prominent in a frequency range below 5 Hz, and its share of the overall attention-dependent SNR improvement was 39 %<sup>96</sup>.

Besides this reduction of correlated oscillatory activity in the low-frequency range, many studies reported an attention-dependent increase in synchronization of neurons representing an attended stimulus in the  $\gamma$ -frequency range (30-100 Hz)<sup>101-108</sup>. This high-frequency synchronization is enhancing the impact of these neurons onto their receiving down-stream neurons since their spikes arrive temporally well-aligned and are therefore likely to induce

## Introduction

spikes at neurons receiving this input<sup>109-112</sup>.

The aforementioned physiological effects of attention on neuronal responses were based on experiments with only one stimulus within the RF. However, the strongest effects of attention on mean firing-rates have been reported when neurons received input of multiple independent stimuli<sup>54,90</sup>. Moran and Desimone (1985)<sup>54</sup> recorded neuronal activity in macaque monkey's area V4 and IT while the animals performed a match to sample task. In some trials, two stimuli were placed inside the same RFs of neurons located in area V4 or IT (inferior temporal cortex), one of them eliciting high firing-rates (effective stimulus), the other one weak firing-rates (ineffective stimulus). Each stimulus could become target in the upcoming trial, while the other stimulus was a non-relevant distractor. They compared trials with both stimuli within the RF to trials with only one of the two stimuli present and found that neurons responded very similar in trials where the same stimulus was attended, irrespective of the presence of a distractor. Neurons responded weakly when the ineffective stimulus was attended even when the stimulus evoking high firing-rates was present in the V4 RF. Correspondingly, they responded strongly when the effective stimulus was attended even though the ineffective stimulus was present as well<sup>54</sup>. These findings based on firing-rates in area V4 and IT have been replicated and extended to other visual areas both in the ventral and dorsal processing pathways<sup>90,91,113-115</sup>. These studies deliver evidence for an attention-dependent modulation of neuronal responses in favor of the attended stimulus when multiple stimuli compete for processing.

### 1.5 Concepts of attention-dependent routing

Moran and Desimone (1985)<sup>54</sup> were the first to investigate a central motif of information processing with the visual system: the conflict of competing convergent inputs to neurons. This conflict arises from the anatomical connectivity pattern of the cortex, which is characterized by a convergence of synaptic connections from upstream to downstream areas<sup>116</sup> (as explained in chapter 1.2). Thus, down-stream neurons are often confronted with competing input signals representing multiple separate objects, which cannot be processed and integrated in parallel<sup>55,117</sup>. As the results of Moran and Desimone (1985) indicate, attention is involved in resolving this conflict in favor of the attended stimulus. In line, it has been shown recently that attention selectively gates signals representing an attended stimulus to a receiving neuronal population, while signals of non-attended stimuli are almost entirely blocked<sup>118</sup>. This “winner

takes all” like impact of neuronal populations representing an attended stimulus on receiving neurons at the expense of other populations representing non-attended stimuli can hardly be attributed to the modest effects of attention on input populations alone (chapter 1.4). The attention-dependent increases in firing rates and improvement of SNR rather improve stimulus representation than prevent other neuronal populations from interfering at the receiving neurons<sup>116,119</sup>. Thus, besides improving local stimulus representation, attention is also involved in the selective routing of relevant information while simultaneously suppressing irrelevant ones. There are several explanatory approaches for such attention-dependent selection. Part of my work is to find causal evidence that helps to clarify which of them proves correct. In the following subchapters, I will give an outline of the different theoretical approaches and explain the embedment of my work into this field of scientific research.

### **1.5.1 The normalization model of attention**

The first concept for explaining the attention-dependent routing of relevant information is the so-called normalization model of attention<sup>120,121</sup>. It originates from an earlier model based on a normalization of neuronal responses, which does not incorporate attention<sup>122</sup>. This earlier model was designed to explain physiological findings in area V1: Neurons decreased their firing-rate in response to the same stimulus when further stimuli were presented close to the neurons RFs. In the model, these findings are explain by lateral inhibition of the recoded neurons originating from neighboring cells. The more stimuli are present, the more neurons are activated and in turn inhibit neighboring neurons. Thus, the individual neurons firing-rates are scaled-down in dependence on the overall population activity. In the model, the overall population activity works as a divisor by which individual responses are normalized.

Reynolds and Heeger (2009)<sup>121</sup> and independently Lee and Maunsell (2009)<sup>120</sup> extended the model to explain the various attention-dependent response modulations for single neurons and populations of neurons respectively<sup>120,121</sup>. This theoretical model now incorporates three independent components: The first component is the stimulus drive (Fig. 4, middle panel); it represents the responses of each neuron of a population to a given stimulus. In the example depicted in Figure 4, two vertical gratings are eliciting neuronal responses at separate locations, which vary according to the orientation preference of the individual neurons (Fig.4, middle panel). The second component is the attention field, which represents the attentional gain of neurons under attentional focus. In the example, spatial attention enhances responses of neurons representing the location of the right grating, irrespective of their orientation tuning. The model

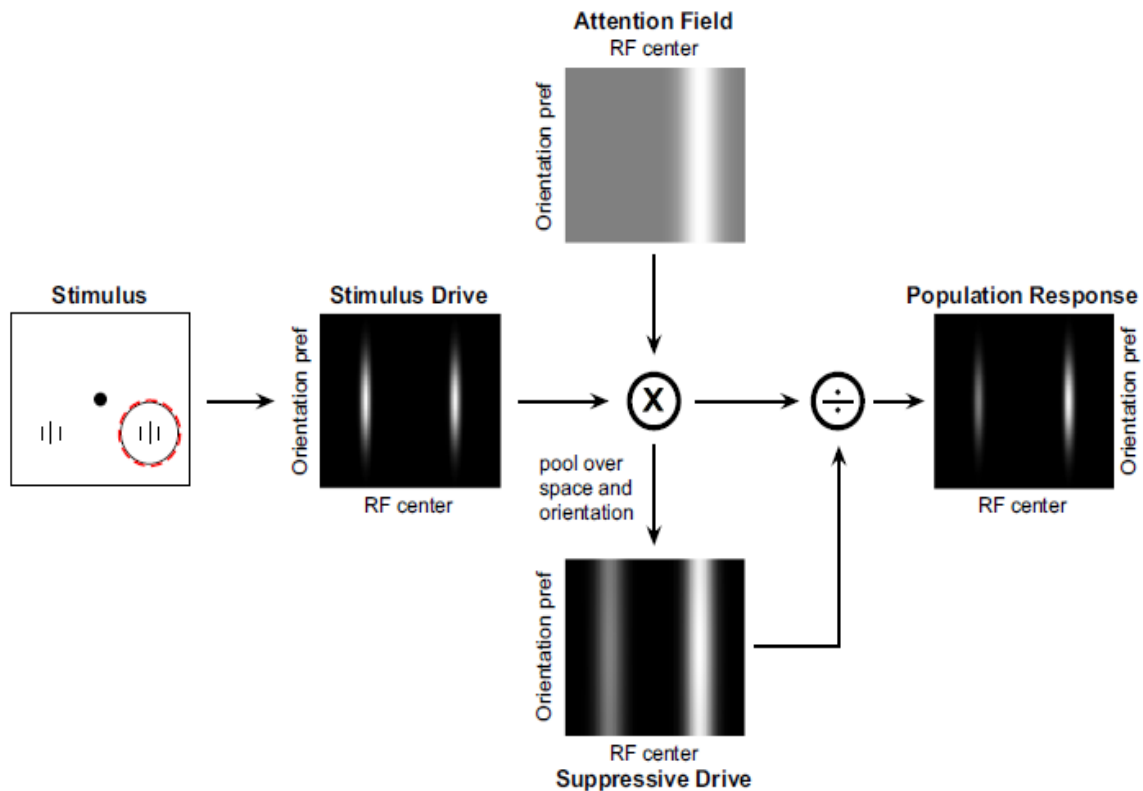


**Figure 4:** Normalization model of attention. The pair of vertical oriented gratings (left most panel, Stimulus) represents the sensory input. The black dot is the fixation point, the black solid circle the RF of an exemplary neuron. The red dashed circle depicts the attentional field (spatial attention), which is focused on the right grating. The next panel (Stimulus Drive) illustrates the responses of a neuronal population to the sensory input. Neurons are aligned according to their spatial location (x-axis) and orientation preference (y-axis). The brightness encodes the strength of individual neuronal responses to the gratings. Low brightness indicates weak response strength and higher brightness strong responses, respectively. The uppermost panel represents the attentional enhancement (Attention Field) for neurons representing the attended location, without orientation specificity. Darker areas represent the value 1, white represents values larger than 1. The matrices of “Attention Field” and “Stimulus Drive” are multiplied pointwise (indicated by arrows and operator  $\times$ ). The suppressive drive (bottom panel) depicts this product of multiplication. For normalization of neuronal responses, the mean over orientation and space of the “Suppressive Drive” is taken and the “Stimulus Drive” normalized by division with the mean “Suppressive Drive” (indicated by division operator). The right panel depicts the normalized response of the population including the attentional gain.

Reprinted from *Neuron*: 61/2, Reynolds JH and Heeger DJ: “The Normalization Model of Attention”, p. 169, © 2009, with permission from Elsevier.

assumes a multiplication of the stimulus drive with the attention field. All responses of neurons located outside the spatial focus of attention are multiplied by a factor of one and thus do not change their response strength. Responses of neurons within the attentional focus are multiplied by a factor larger than one (bright area in Attention Field), which corresponds to an attentional

## Introduction

enhancement of responses. The third component of the model is the suppressive field (lower panel, Fig. 4), which is the product of the attention field and stimulus drive. The neuronal responses represented by the suppressive field are then pooled across all locations and along feature space. This pooled neuronal activity becomes the divisor for the normalization of the actual neuronal responses (stimulus drive). The division results in a normalized population response with an attentional bias for the spatial location that was attended<sup>121</sup>. More generally, the model works as a weighted average, based on the division of individual neuronal responses by the pooled overall activity across a population of neurons representing a large proportion of visual space.

The larger the multiplication factor representing the attentional gain is chosen, the more responses of neurons representing non-attended stimuli are scaled down in relation to neurons representing attended stimuli. By choosing a large factor, the model can explain the “winner takes all” effect observed for input neurons representing an attended stimulus on receiving neurons. The authors do not state or discuss how attention provides this required large gain. The attentional gain on mean firing rates in V1, for example, is in most studies described to be around 20 %<sup>96</sup> or less<sup>54,90</sup> (factor 1.2), which would be insufficient to scale down all responses representing non-attended stimuli by normalization.

### **1.5.2 Balanced excitation and inhibition model**

Another theoretical approach to explain the attention-dependent selection and processing of relevant information while suppressing irrelevant ones is the model of balanced excitation and inhibition proposed by Vogels and Abbott (2009)<sup>123</sup>. Their work is based on earlier models that addressed the question of how synchronous spiking activity is generated and propagated within and between cortical networks and how the anatomic circuitry of inhibitory and excitatory neurons needs to be organized for fulfilling these functions<sup>124-127</sup>. The model of Vogels and Abbott (2009) is built upon this framework of neuronal signal propagation and went beyond by addressing the question of how multiple signals are gated and controlled within such a network since they cannot be processed and routed in parallel. The model is based on prior experimental<sup>128,129</sup> and theoretical findings<sup>130,131</sup>, which showed that on a global scale the average firing rate is kept constant, indicating that there is a balance between excitation and inhibition. Vogels and Abbott proposed that not only the brain as a whole but also local populations of neurons are generally in a balanced state, i.e. the excitatory and inhibitory inputs are balanced, in order to keep neurons below spiking threshold. This balance is kept constant

## Introduction

by fine-tuning of inputs of these local populations, if neurons receive more excitatory input from some subsets of inputs, the amount of inhibitory input is adapted such that it cancels out again, and neurons stay in the balanced, non-responding state<sup>128,129</sup>.

In order to selectively route and process relevant information, the authors suggest that this fine-tuned balance is disrupted. They propose that those neurons connected with subsets of afferent inputs representing relevant information, the gain of inhibitory inputs is diminished (or excitatory drive is increased and inhibitory drive stays constant). Thus, EPSPs (excitatory postsynaptic potentials) can sum up and evoke spikes at the receiving neuron, while other subsets of inputs representing non-relevant information are still blocked. In theory, this can explain the attention-dependent gating of relevant information between input- and receiver neurons. However, this model assumes a very fine control of individual subsets of afferent connections and very distinct sender and receiver pathways.

### 1.5.3 Routing by Synchrony

Another theory for explaining selective routing of relevant information is based on modulations of the temporal structure of neuronal responses. When scientists started investigating the stochastic relations between spike-trains of nearby neurons theoretically and experimentally, they found that these spike trains are not independent of one another<sup>132-135</sup>. Gerstein and Perkel, for example (1972)<sup>135</sup> investigated the dependency of spikes recorded in auditory cortex of cats (anesthetized) and in the pleural ganglions of Californian sea slugs (*Aplysia californica*). The authors found different patterns of temporal correlations between neurons, by computing cross-correlation histograms between their spike times. Due to these different patterns of spike correlations, they differentiated between different types of anatomical connections: Neurons that showed simultaneous spiking activity received likely common input. Neurons with a fixed temporal offset between spike times were likely in a receiver sender relation with one another. The analysis and interpretation of correlation patterns between neurons for investigating anatomical connections have since been used in other species as well, as in the striate cortex of cats (area 17)<sup>136-139</sup> and macaques<sup>140,141</sup>.

Espinosa and Gerstein (1988)<sup>142</sup> were one of the first who gave experimental evidence that cross-correlations are not only reflecting anatomical connections between neurons but are also stimulus-dependent. The authors recorded spike trains of several neurons in the primary auditory cortex of sedated cats. While recording neuronal activity, they played three-tone sequences to the animals and analyzed if and how the cross-correlation between neurons'

## Introduction

activity changed in dependence of the auditory stimuli. The pattern of neurons, which showed correlated spiking activity, differed in dependence of the stimulus that was played. Based on this and other experimental results, Aertsen et al., (1989)<sup>143</sup> coined the term “effective connectivity” for the dynamic and stimulus-dependent formation of neuronal assemblies based on correlated activity. They proposed that by including the temporal domain (correlated activity) neuronal assemblies might be formed dynamically, which also allows the same neurons to take part in different assemblies.

The dynamic formation of assemblies was furthermore seen as a possible solution for the so-called combinatorial problem. It arises from the almost infinite number of different settings and object-combinations, forming a visual scene<sup>144</sup>. The visual system is capable of recognizing the same object, in different colors or angles of view, as well as in different scenes, although each of these different settings results in different patterns of firing rates across the visual cortex. Hence, the visual system either provides the same number of neurons as there are objects in every imaginable combination of visual scenes (grandmother cells)<sup>145,146</sup> or it somehow couples neurons encoding specific objects together, irrespective of the actual scene they are in<sup>147-150</sup>.

Thus, neuroscientists and theoreticians turned their focus on further investigations of dynamic neuronal assembly formation and distributed coding<sup>147,148,151-156</sup>. Subsequent experimental findings supported the idea of a stimulus-specific formation of neuronal assemblies, which are functionally coupled by temporal synchronization (correlated activity) of their spiking activity<sup>138,157,158</sup>. Gray and colleagues (1989)<sup>159</sup>, for example, recorded multi-unit activity in area 17 of cats at multiple sites simultaneously. They found that neurons sharing the same stimulus preference synchronize their activity in a frequency band between 40 – 60 Hz. Equidistant neurons with a different orientation preference showed no synchronized activity. Furthermore, neurons separated by more than 7 mm synchronize their activity, although each of them was stimulated with an individual moving bar. However, they only synchronized when those bars moved in the same direction<sup>159</sup>. Other studies showed that neurons synchronize their activity in a specific frequency band when they are activated by separate objects, which together form a unified shape. Neurons, which respond to objects which do not form a coherent shape, showed almost no synchronization<sup>138,159-161</sup>.

Eckhorn et al. (1988)<sup>158</sup> and later also Engel et al. (1991)<sup>161</sup>, reported that not only nearby neurons synchronize their activity, but also neurons located in different areas of the cat’s visual cortex. Together, these experimental findings and previously published theoretical considerations<sup>162,163</sup> gave rise to the so-called “binding by synchrony”- theory. This theory states that neurons, which encode different features of the same stimulus, synchronize their

## Introduction

activity in time, in order to form a functional processing network.

Kreiter and Singer (1996)<sup>164</sup> gave strong support for this theory when investigating the synchronization of neurons with overlapping RFs, but different tuning for direction of movement, in monkey visual area MT. They presented either one or two moving bars on a screen. When only one bar was presented, the direction of movement was not the preferred for both recorded neurons, but both responded sufficiently well. In the two-bar condition, the directions of movement of both bars were chosen such that they matched the preferred directions of both recorded neurons (both bars moved in different directions). The authors reported that neurons synchronized their responses when only one bar with non-optimal direction of movement for both neurons was present. In cases where both bars moved in different directions, each of them optimal for one of the two neurons, they showed almost no synchronization of responses. These findings indicated that in the case of only one bar, both neurons were integrated into the same processing network by synchronizing their activity, since both delivered information about features of the stimulus. In the cases with two stimuli present, both neurons encoded one of the two bars better, suggesting that these neurons are integrated into two distinct functional assemblies with individual patterns of synchronization. However, it is worth pointing out here that there are studies that failed to find evidence for a dynamic formation of functional assemblies based on synchronization<sup>165-169</sup>. Also, several studies reported a strong dependence of synchronization (amplitude, frequency) on stimulus properties such as size and speed of motion<sup>108,170,171</sup>, which raised doubts whether synchronization is relevant for information processing or merely reflecting the neuronal circuit organization without any functional relevance<sup>172</sup>. This controversy between scientists interpreting synchronization as an epiphenomenon of anatomical network architecture and others who believe in the functional significance is far from being resolved (for an extensive review see: Bosman et al., (2014)<sup>173</sup>). There have been many studies, which gave strong evidence for not only one, but several functional roles of synchronization in information processing<sup>173</sup>.

Synchronization became, for example, a candidate mechanism for attention-dependent selective information routing across the cortex. Roelfsema et al., (1997)<sup>174</sup> were the first to show that synchronization of neurons located in different areas of the cat's visual cortex increased in the  $\gamma$ - and beta ( $\beta$ , 12.5 – 30 Hz) frequency-band when the cats performed a visual task. This synchronization vanished when the animals rested or ate. Moreover, Steinmetz et al. (2000)<sup>175</sup> found that many pairs of neurons recorded in somatosensory cortex of macaque monkeys changed their degree of synchronization in dependence of which sensory modality (tactility or vision) was relevant for successful task performance. In line, Fries et al., (2001)<sup>102</sup> showed that

## Introduction

spikes of V4 neurons responding to an attended stimulus, correlate with a specific phase of the V4  $\gamma$ -band of the local field potential (LFP) whereas spikes of the same neurons in response to the same stimulus but without attention focused on it were not aligned to a specific phase. This finding of attention-dependent modulations of  $\gamma$ -band synchronization has been replicated and extended to further visual areas<sup>103,105,176</sup>. Furthermore, Gregoriou et al., (2009)<sup>107</sup> showed that V4 neurons and upstream FEF (frontal eye fields) neurons synchronized their activity in the  $\gamma$ -frequency band when they represented an attended stimulus. The same neuronal populations showed significantly less  $\gamma$ -synchronization when the stimulus was not attended.

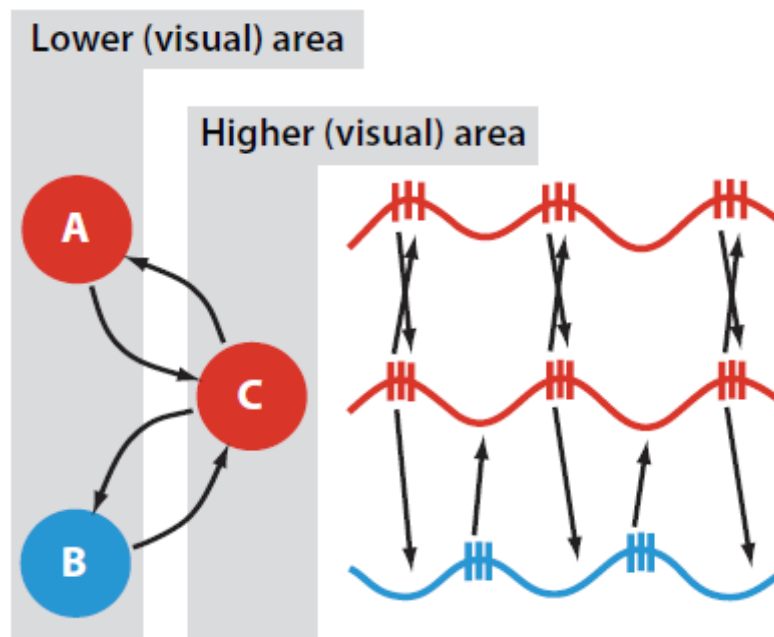


**Figure 5:** Scheme of CTC-hypothesis. Two input populations (A, B) deliver convergent input to a downstream receiver population (C). As indicated by the equal color, populations A and C synchronize their activity and deliver output at the other neurons' effective phases. Population B delivers input at ineffective phases of receiver population C.

Reprinted and with permission from: *Annual review of neuroscience*: 32, Fries, P: "Neuronal gamma-band synchronization as a fundamental process in cortical computation", p. 214© 2009.

The attention dependent modulations of synchronous neuronal activity in the  $\gamma$ -band gave rise to a hypothesis explaining the attention-dependent routing of information by modulations of synchronization between neurons: the so-called "Communication through Coherence (CTC)" hypothesis<sup>6,177</sup>. The CTC-hypothesis assumes that the observed attention-dependent enhancement of  $\gamma$ -band synchronization corresponds to a synchronization of neurons' activity cycles. An activity cycle comprises periods of high effectivity for input signals (Fig. 5 peaks), i.e., incoming spikes are likely to generate spikes (neuron close to spiking threshold), and periods when incoming spikes are unlikely to generate spikes (Fig. 5 troughs, hyperpolarization

## Introduction

of receiving neurons)<sup>178</sup>. Thus, downstream receiver neurons are more likely to respond to input signals arriving within the effective phase (Fig. 5 neurons A to C). Neurons delivering their spikes to non-effective phases would fail to gain influence on the receiving neurons (Fig. 5, neurons B to C). In theory, this selective synchronization between neurons representing relevant information could constitute an efficient selection mechanism for relevant information, which is supported by results of several theoretical studies<sup>179-182</sup>.

In line, experiments of Grothe and colleagues (2012)<sup>183</sup> and also of Bosman and colleagues (2012)<sup>184</sup> showed that attention modulates the  $\gamma$ -synchronization between input populations (V1) and the receiving neurons (V4) in macaque visual cortex. They recorded the neuronal activity of two V1 populations delivering convergent input to the same V4 population (which was also recorded). Independently of one another, they found, that in dependence of attention, the synchronization in the  $\gamma$ -frequency band switched between both input populations and the receiving V4 population. Besides, Grothe and colleagues (2012)<sup>183</sup> could also show, that spikes of V4 single neurons are synchronized selectively with the  $\gamma$ -band activity of input populations representing the attended stimulus.

All these theoretical and experimental findings delivered evidence for the potential functional roles of  $\gamma$ -band synchronization for selective and attention-dependent routing of relevant information. However, as stated above, this is one interpretation of the physiological findings reported by many scientists; others interpret them as simple epiphenomenon arising from the anatomy of neuronal networks without functional relevance<sup>172</sup>.

In chapter 2, I am presenting the results of my work on the potentially causal relevance of  $\gamma$ -band synchronization for attention-dependent and selective processing of relevant information. In contrast to the previous investigations, our experimental design allowed to conclude whether or not  $\gamma$ -band synchronization plays a causal role in selective information processing within the visual system.

## Chapter 2

### 2.1 Signal transmission between monkey areas V2 and V4 is causally dependent on gamma phase synchronization

Declaration on the contribution of the candidate to a multi-author article, which is included as a chapter in the submitted doctoral thesis.

Experimental concept and design:	30 %
Data acquisition:	65 %
Data analysis:	100 %
Data interpretation:	75 %
Preparation of Figures and Tables:	100 %
Drafting of the manuscript:	90%

Date:

Signature:

This chapter is a finalized manuscript for submission in a scientific journal.

## **Signal transmission between monkey areas V2 and V4 is causally dependent on phase synchronization**

Eric Drebitz<sup>1</sup>, Lukas-Paul Rausch<sup>1</sup>, Andreas K. Kreiter<sup>1</sup>

<sup>1</sup> Brain Research Institute, Center for Cognitive Sciences, University of Bremen

**Successful behavior relies on the brain's ability to adapt its processing fast and flexible to changing behavioral demands. A characteristic example of such adaptations is the attention-dependent and selective processing of behaviorally relevant information. On the neuronal level, this is reflected by changes in neuronal responses in dependence of attention. Neurons receiving signals from multiple objects respond almost "as if" only the attended object is present within their receptive fields (RFs), disregarding the presence of further objects<sup>54,90,183,185</sup>. The neuronal mechanism behind this selection of relevant information is still under debate. Various theoretical approaches have been proposed to explain the selective routing and processing of relevant information<sup>121,123,177,186</sup>. A fundamental difference between these approaches is that some require a selective synchronization between receiving neurons and those subsets of afferent neurons representing the relevant information. To investigate whether this selective synchronization plays a causal role in selective routing and processing, we performed an experiment in which we interfered with information processing by applying short electric pulses. These pulses were delivered to neurons located in area V2 of macaque monkeys while recording the neuronal activity of downstream V4 neurons. We found that the electrically evoked activity in V2 affected downstream V4 neurons and behavior strongly when arriving at a specific phase of the V4 gamma-band ( $\gamma$ -band) activity. Spikes arriving at this specific phase caused a significant increase in reaction times (RTs), whereas there was no influence of stimulation on behavior when spikes arrived at other phases. The same holds for spiking activity in V4. We found a significant increase in spiking-activity of V4 neurons in response to the electrically evoked spikes 10 to 17 ms after stimulation in V2, but only if the electrically evoked spikes arrived within the trough of the V4  $\gamma$ -oscillation. These findings support the concept of temporal synchronization being causal for selective information transfer and processing.**

Electric pulses were applied while the monkeys performed an attention-demanding shape-tracking task<sup>103,183</sup>. The task comprises two stimuli located within the same V4 RF, but only one of them in the V2 RF, which received electrical stimulation (Fig. 6 A/B). After the static presentation, all shapes started morphing continuously into other shapes (Fig. 6C). Each morph

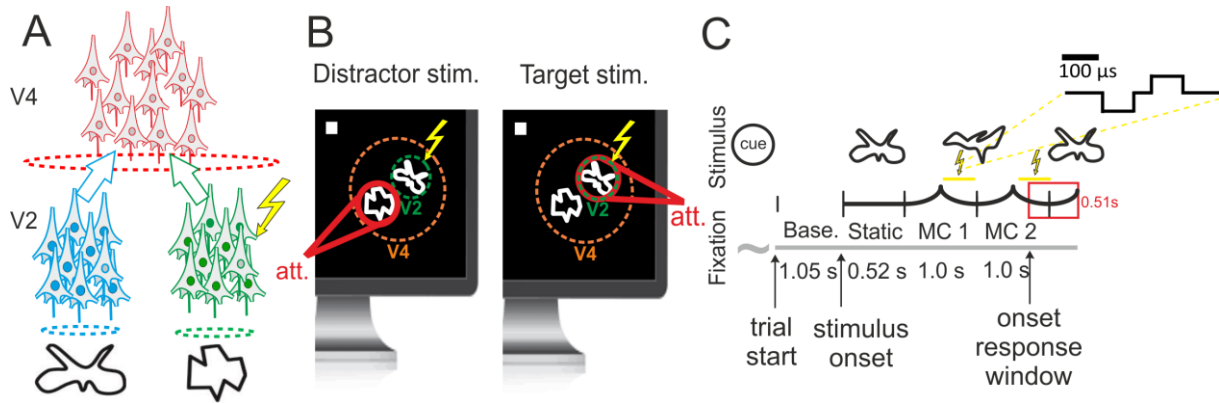


**Figure 6:** Illustration of experimental- and task design **A** Connection scheme of converging V2 input to V4. The two stimuli activate separate V2 populations, which deliver input to the same V4 population. One of the V2 sites was electrically stimulated (indicated by lightning symbol). **B** The two relevant conditions of the shape-tracking task. Spatial attention (att.) was cued to both stimuli located in V4 in the course of a recording session, and conditions are labeled accordingly either as “target stimulated” or “distractor stimulated”. V4 and V2 RFs are depicted as dashed circles that do not appear on screen. The V2 site, which received electric stimulation is indicated by lightning symbol **C** Morphing sequence of a target stimulus during a short trial (2 morph cycles, MC). After trial start and baseline period (Base.), the initial shape was presented statically (Static), whereupon it started morphing continuously into other shapes. Trials ended when the initial shape reappeared at the cued location. A single electric pulse was applied within the last half of each morph cycle (indicated by yellow vertical bars). Each pulse was biphasic, and either  $\pm 15 \mu\text{A}$  or  $\pm 25 \mu\text{A}$  were applied (inset). For correct task execution, the animal had to release the lever within the response window (red rectangle).

cycle (MC) lasted 1000 ms and trials contained between two and four of them. At random times within the second half (550 – 950 ms) of each MC, a single electric pulse (Fig. 6C) was applied to V2 neurons located in the supragranular layers. Since the target stimulus could appear at all stimulus locations, pulses were delivered to a V2 population representing either a relevant (target) stimulus or a non-relevant (distractor) stimulus (Fig.6 B). The animals were required to detect the reappearance of the initial shape at the cued location while ignoring stimuli at non-cued locations (Fig. 6 B/C, for a detailed description: chapter 2.2, Materials and Methods).

In order to investigate if potential effects of these stimulations on behavior were dependent on the current  $\gamma$ -oscillation in V4, we first sorted trials according to their  $\gamma$ -phase 3 ms after the electric stimulation preceding the behavioral response. Figure 7 shows how the median RTs depend on the V4  $\gamma$ -phases (black dots). Medians are taken within windows of  $60^\circ$  width (separated by  $1^\circ$ , 360 in total). We quantified the  $\gamma$ -phase dependence of median RTs by performing a sinusoidal fit and estimating its peak-to-peak-amplitude (PPA; Fig. 7, solid black lines). For each task condition and animal, median RTs showed a significant modulation in dependence of the  $\gamma$ -phase at which the electrically evoked spikes arrived in V4 (Fig. 7 A-D, significance threshold at  $p < 0.05$  highlighted in gray). We found significant differences between median RTs of trials where the electrically evoked spikes arrived at the peak of the sinusoidal fit

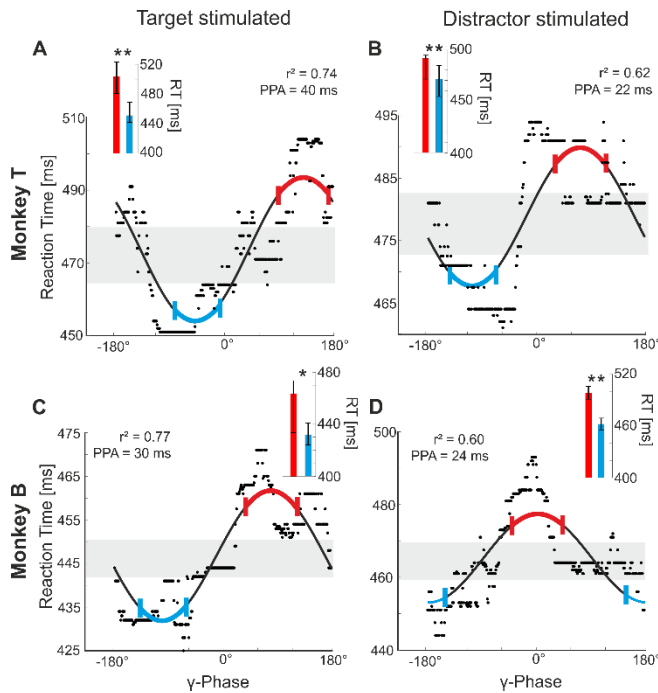


**Figure 7:**  $\gamma$ -phase dependent effect of stimulation on RTs. **A** Median RTs and sinusoidal-fit of target stimulated conditions of monkey T across  $\gamma$ -phase. Each dot represents the median RT of a window  $\pm 30^\circ$  centered around the value indicated on the abscissa. Red and blue highlighted are phase periods of  $60^\circ$  centered around the peak and trough of the fit, respectively. The gray highlighted area indicates the significance threshold at  $p = 0.05$ . The bar-plot inset shows median RTs for all cases falling into the peak and trough phase periods. Error bars indicate 95 % confidence intervals of medians. The asterisks indicate high significance ( $p < 0.001$ ). **B** same as in **A** but for distractor stimulated conditions. **C** same as in **A** but for monkey B. The asterisk indicates significance at  $p < 0.05$ . **D** same as in **A** but for monkey B and distractor stimulated conditions

(Fig. 7 A-D, red-colored,  $\pm 30^\circ$  around peak) as compared to trials where these spikes arrived at the trough (Fig. A-D, blue-colored,  $\pm 30^\circ$  around trough). The differences in median RTs for target stimulated conditions (Fig. 7A/C) was 53 ms for monkey T and 32 ms for monkey B (monkey T: median trough = 504 ms,  $n = 90$ ; median peak = 451 ms,  $n = 102$ ;  $p = 0.000086$ ,  $z = 3.9258$ ; monkey B: median trough = 464 ms,  $n = 137$ ; median peak = 432 ms,  $n = 159$ ,  $p = 0.0166$ ,  $z = 2.3948$ , both Wilcoxon rank-sum test). The differences for distractor stimulated conditions (Fig. 7 B/D) were comparable with a median difference of 20 ms for monkey T and 42 ms for monkey B (monkey T: median trough = 491 ms,  $n = 235$ ; median peak = 471 ms,  $n = 235$ ,  $p = 0.0097$ ,  $z = 2.5857$ ; monkey B: median trough = 493 ms,  $n = 121$ ; median peak = 451 ms,  $n = 143$ ,  $p = 0.00037$ ,  $z = 3.5607$ , both Wilcoxon rank-sum test).

After having shown that the electrical stimulation in V2 slows down RTs in dependence of the V4  $\gamma$ -phase, we investigated whether stimulation affects neuronal activity in V4 similarly. For this, we calculated multi-unit activity as measured by ESA<sup>185,187</sup> (see also chapter 2.2, Materials and Methods) over time, in bins of 3 ms (3 to 33 ms after stimulation, shifted by 0.2 ms, Fig. 8A). These 30 ms periods of ESA following stimulation were sorted according to the LFP  $\gamma$ -phase 3 ms after electrical stimulation. For each time bin, the PPA of mean ESA across  $\gamma$ -phases was quantified based on a sinusoidal fit (Fig. 8B). The insets shown in Figure 8 C-F depict the PPAs across time for each task condition and animal as well as the respective significance threshold. For monkey T, ESA-modulation surpassed the threshold between 15 and 19.8 ms post-stimulation for target-stimulated conditions (Fig. 8C, inset) and between 13.2 and 20.2 ms for distractor-stimulated

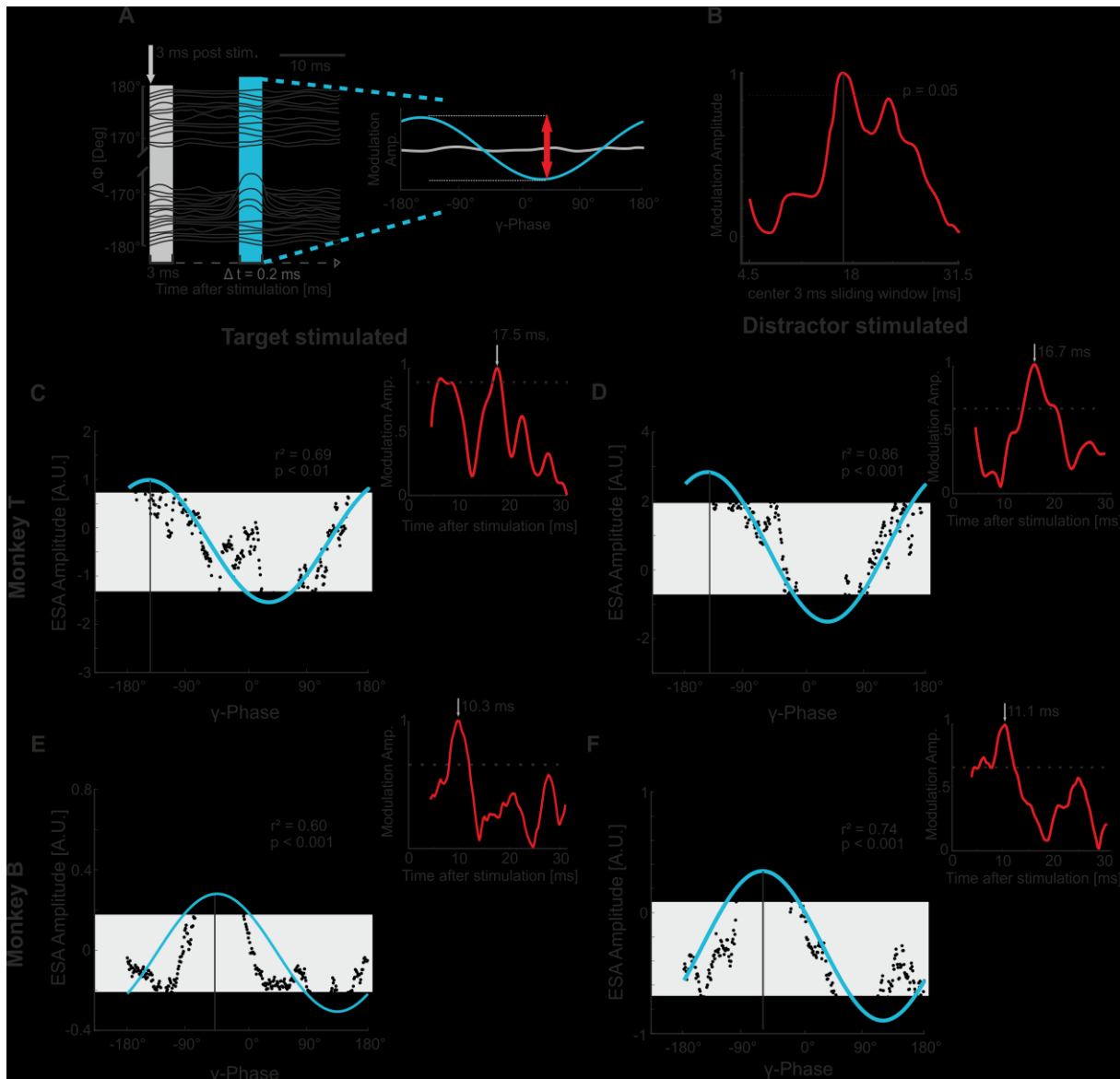


**Figure 8:**  $\gamma$ -phase-dependent modulation of multi-unit activity. **A-B** Schematic illustration of analysis procedure for calculating  $\gamma$ -phase dependence of stimulation on ESA. **A** Each gray trace represents the post-stimulation time course (3 -33 ms) of V4 ESA averaged over all trials with a  $\gamma$ -phase within  $\pm 30^\circ$  of the value indicated on the ordinate at  $t = 3$  ms. Within the early, gray time-bin ESA is similar in all traces and thus independent of the  $\gamma$ -phase, whereas in the later, blue bin an ESA-response to electrical stimulation is illustrated, that differs across phases. The  $\gamma$ -phase-dependent modulation of ESA was estimated within each time bin (3 ms,  $\Delta t = 0.2$  ms) as PPA of a sinusoidal fit across  $\gamma$ -phases. The fitted sinus functions for the gray and blue time-bin are depicted in the right panel. The red arrow indicates the modulation depth as estimated based on the PPA. **B** Illustration of the time-course of  $\gamma$ -phase dependent ESA-modulation based on PPAs. The dashed line indicates level of significance ( $p = 0.05$ ). **C-D**  $\gamma$ -phase-dependent modulation of ESA for both monkeys and task conditions. **C**  $\gamma$ -phase-dependence of ESA for the time of highest stimulus dependent modulation (indicated by arrow in inset) for target-stim. conditions of monkey T. Black dots represent mean ESA-values across trials, the red trace is the fitted sinus function, and the black vertical line indicates the  $\gamma$ -phase at its peak. The  $r^2$  value describes the goodness of fit and  $p$ -value the likelihood of the shown fit amplitude to occur in a data-set with random  $\gamma$ -phase-ESA relation (shift-predictor). **D** same as in C, but for distractor stimulated conditions. **E** same as in C but for monkey B. **F** same conventions as in C, but monkey B and distractor stimulated conditions.

conditions (Fig. 8D, inset). The times of highest ESA-modulation (peak) were very similar at

17.5 and 16.7 ms respectively. Figures 8 C and D show the dependence of ESA on the  $\gamma$ -phases for the times of highest ESA-modulation respectively (indicated by arrow in inset). We found for both conditions very similar phase positions of highest ESA in response to electrical stimulation ( $-148^\circ$  and  $-150.2^\circ$ ; Fig. 8 C/D, vertical black bars). We observed the same pattern of results for monkey B (Fig. 8 E/F) although the times of significant ESA-modulation differed between animals. The ESA-modulation of monkey B surpass the significance threshold between 7.4 ms and 13.4 ms for target stimulated conditions and 7.2, and 14.4 ms for distractor stimulated conditions (Fig. 8 E/F insets). As for monkey T, the times of strongest ESA-modulation were very similar in both conditions with 10.3 ms and 11.1 ms post-stimulation. The dependence of ESA across  $\gamma$ -phases for these periods is shown in Figure 8 E and F respectively. The highest ESA-responses to electrical stimulation were aligned again at very similar phase positions with  $-56.1^\circ$  and  $-62.2^\circ$ , respectively (Fig. 8E/F vertical black bars). In summary, these results show that the electrically evoked spikes originating in V2 initiated additional spikes in V4 in dependence of the LFP  $\gamma$ -phase. The time window in which electrical stimulation caused  $\gamma$ -phase dependent enhancement of spiking activity lasted on average 6.25 ms.

The times when stimulation affected multi-unit activity was up to one  $\gamma$ -cycle later than the time we determined the  $\gamma$ -phase (at 3 ms post stim.). This implies that the phase position of highest ESA-responses described above is not reflecting the actual phase in which incoming spikes are most effective. In order to determine the  $\gamma$ -phase at the time of significant impact of stimulation on multi-unit activity, we forecasted the progression of the  $\gamma$ -band LFP, based on the  $\gamma$ -power peak frequencies. Peak frequencies did not differ between conditions and were 71 Hz for monkey T (Fig. 9A), and 78.4 Hz for monkey B (Fig 9B). Figure 9 C-F schematically shows the progression of those  $\gamma$ -LFPs aligned to the highest ESA-values when taking the  $\gamma$ -phase 3 ms after stimulation (vertical black bar in Fig. 8 C-F). The first red arrow indicates the alignment of the highest ESA-values in response to stimulation at  $-148^\circ$  of the  $\gamma$ -cycle, 3 ms after stimulation. The second arrow indicates the phase position of highest ESA-values at 17.5 ms ( $-138^\circ$ ) for target-stimulated trials. For distractor-stimulated conditions, the highest ESA-values in response to electrical stimulation (at 16.7 ms) are also aligned to the trough at  $-159^\circ$  of the  $\gamma$ -cycle (Fig. 9D). Monkey B shows a similar pattern of ESA -  $\gamma$ -phase coupling at times of significant responses to electrical stimulation. During target stimulated trials, peak ESA-values are aligned to  $151^\circ$  (Fig. 9E), and to  $166^\circ$  for distractor stimulated conditions (Fig. 9F). All four forecasted ESA-peak/  $\gamma$ -phase relations scatter around the trough of the  $\gamma$ -oscillation by less than  $45^\circ$ . The difference in timing of significant responses of around 6 ms to the electrical

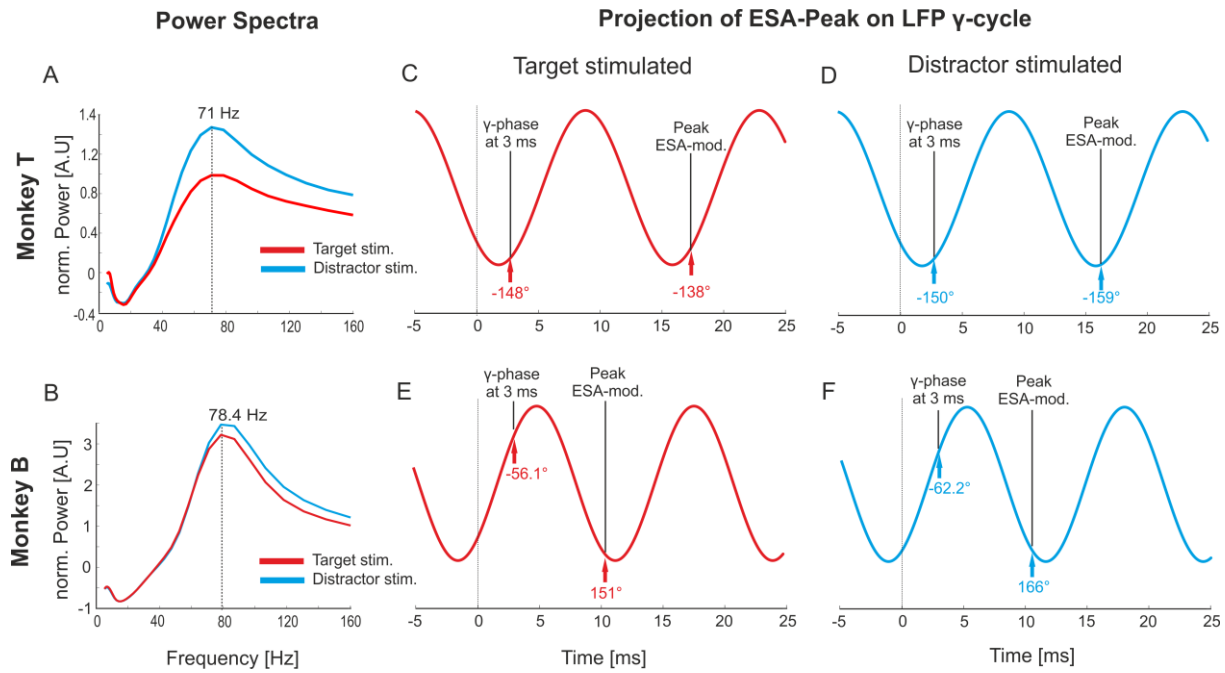


**Figure 9:** *ESA-peak to  $\gamma$ -cycle relations.* **A** Mean power spectra for monkey T of target (red) and distractor (blue) stimulated conditions. The peak frequency is indicated by the vertical dashed line at 71 Hz. **B** same as in A but for monkey B, the  $\gamma$ -peak frequency is at 78.4 Hz. **C** Projection of ESA-peak on forecasted  $\gamma$ -oscillation (schematic) for target stimulated conditions of monkey T. The left arrow indicates the  $\gamma$ -phase of the ESA-peak at 3 ms after stimulation. The right arrow indicated the  $\gamma$ -phase of the ESA-peak at the time of strongest ESA-modulation (17.5 ms) in response to electrical stimulation. **D** same as in C but for distractor stimulated conditions and 16.7 ms as time of strongest modulation. **E** same as in C but for monkey B with 10.3 ms as time of strongest modulation. **F** same as in C but for monkey B and distractor stimulated conditions. 11.1 ms is the time of strongest ESA-modulation.

stimulation between animals, is likely attributed to the different recording depths. Based on the symmetry of stimulus onset VEPs, we found monkey T's recording sites to be located in layers 2/3 and recording sites of monkey B to be located in layer 4 (chapter 2.3, Supplements). The difference of 6 ms between responses to electrical stimulation of neurons located in layers 2/3 and layer 4 is similar to the response latency between neurons in V1 to a visual stimulus, which was reported to be between 6 and 10 ms<sup>188</sup>.

In summary, our results demonstrate that the effects of electrical stimulation in V2 strongly depended on the  $\gamma$ -phase of the downstream V4 neurons. RTs were significantly slower when the electrically evoked V2 spikes arrived at a specific phase of the  $\gamma$ -cycle as compared to its anti-phase. Also, we could show that the electrically evoked spikes originating in V2 caused V4 neurons to generate additional spikes in a short time window following their arrival and also strongly depending on the current V4  $\gamma$ -phase. More specifically, we estimated the effective phase of the  $\gamma$ -cycle to be located at the trough of the  $\gamma$ -oscillation. The arrival of electrically evoked spikes is likely one to two milliseconds earlier<sup>189</sup> due to the latency of synaptic transmission and EPSP-summation. The effective phase is, therefore rather the beginning of the

LFP's trough than its center. The negative LFP trough is thought to reflect mainly the synchronous influx of positive ions from extracellular to intracellular space at the postsynaptic membrane, i.e. neurons depolarize and approach spiking threshold<sup>190,191</sup>, which makes them sensitive to incoming spikes<sup>177</sup>. Thus, the trough being the effective phase for signal transmission is very convincing. Previous work showed that V4 and V1 neurons synchronize their activity in the  $\gamma$ -band when they represent the attended, relevant stimulus without mentioning actual phase relations between neurons<sup>183,184</sup>. Also, RTs have been shown to be faster in trials with comparably strong synchronization between V1 and V4<sup>192</sup>. Other V1 populations delivering convergent input but representing irrelevant objects showed at the same time almost no  $\gamma$ -synchronization<sup>183,184</sup>. A selective  $\gamma$ -synchronization between areas encoding an attended stimulus has also been shown between macaque visual areas V4 and FEF<sup>107,193</sup>, as well as between widespread visual areas of the human cortex<sup>194</sup>. Other studies described  $\gamma$ -synchronization between separate auditory areas representing an attended tone<sup>195</sup>. These findings give further support for the functional relevance of  $\gamma$ -phase synchronization for selective information processing within the cortex.

Another interesting aspect of our data is that the effective phases for electric stimulations are almost identical between attentional conditions for the individual animals. Indicating that the  $\gamma$ -phase-dependent impact of stimulation on RTs and spiking-activity is not dependent on the  $\gamma$ -oscillation in area V2 since it is well known that input populations representing a non-relevant stimulus show almost no synchronization with upstream areas<sup>183,184</sup>. Thus, the  $\gamma$ -phase measured in V4 is almost randomly related to the ongoing  $\gamma$ -oscillation in V2 when representing a distractor stimulus. A potential V2, instead of V4,  $\gamma$ -phase dependence of the effects of stimulation would not deliver V4  $\gamma$ -phase-dependent effects as we found.

These results strongly support the idea of  $\gamma$ -phase synchronization playing a causal role in selective information processing and routing.

## 2.2 Materials and Methods

### Surgical preparation

Two male macaque monkeys (*Macaca mulatta*) were implanted under aseptic conditions with a titanium bolt to fixate the head and a recording chamber above visual areas V4 and V2. The target areas were identified based on anatomical MRI-scans. All procedures were approved by the local authorities (Senator für Gesundheit, Bremen, Germany) and following the German

Animal Welfare Act (TierSchG) and the guidelines of the European Union (2010/63/EU) for care and use of laboratory animals.

### **Task paradigm**

The animals performed a highly demanding shape tracking task, which is known to induce strong  $\gamma$ -band power<sup>103,183,185</sup> (Fig. 6B/C). Each trial started with the presentation of a cue consisting of an annulus ( $1^\circ$  in diameter,  $0.04^\circ$  line widths) indicating the relevant stimulus location of the upcoming trial. After 2 s a central rectangular fixation point (FP,  $0.15^\circ \times 0.15^\circ$ ,  $2.45 \text{ Cd/m}^2$ ) was presented on screen signaling monkeys to initiate the trial by depressing a lever within a period of 4.5 s and holding fixation in a  $1^\circ$  fixation window (diameter) centered on the FP. Following lever press, the spatial cue disappeared, and nothing but the FP was present on screen for 1.05 s (baseline period). After this baseline period, three to four stimuli consisting of complex-shaped contours ( $1.5^\circ$  diameter, line width  $0.25^\circ$ ,  $3.8 \text{ cd/m}^2$ ) appeared on the screen. One or two were placed contra-laterally to the recording sites in V2 and V4 in the lower visual quadrant of the visual field. The other two stimuli were placed at point-mirrored positions in the upper quadrant. For each recording session, stimulus locations were chosen such that two stimuli were located within the same V4 RF, but each of them in separate V2 RFs. After 0.52 s of static presentation, all shapes started morphing continuously into other complex-shaped contours. The contours were chosen randomly out of a set of 11 shapes (6 shapes for monkey B). Note that for monkey T all shapes of the set could become the initial target shape, whereas, for monkey B, only two shapes could become the target shape. A complete morph cycle (MC), i.e., complete morphing from one shape into another, lasted 1 s. Trials could contain up to four of these MCs, but at least two. The monkeys had to detect the reappearance of the initial shape at the cued location within a response window of 0.51 s starting 0.3 s before the full reappearance to 0.21 s after. Since each stimulus location on screen could become a target stimulus, the electrically stimulated V2 population could either represent a target or distractor shape and stimulus conditions were labeled accordingly as “target stimulated” or “distractor stimulated” (Fig. 6B). Besides, we included task conditions with only one stimulus present within the V4 RF, for both stimulus locations in the V4 RF, respectively. Trials were terminated without reward if animals released the lever before or after the response window or moved their center of gaze by more than  $0.5^\circ$  from the FP.

### **Experimental setup and recording procedure**

The animals sat in a custom-made primate chair 95 cm (93 cm for monkey B) in front of a 20-inch CRT-monitor with a resolution of 1024 x 768 pixels and a refresh rate of 100 Hz. The background luminance of the screen was constant at 0.03 cd/m<sup>2</sup>. Eye-positions were monitored by video-oculography (IScan Inc., Woburn, MA, USA). Intra-cortical recordings were performed using up to four epoxy-insulated tungsten micro-electrodes (125 µm diameter, 1 – 3 MΩ, FHC Inc., Bowdoin, ME, USA) for acute recordings in V4 and glass-insulated tungsten micro-electrodes (125 µm diameter, 1 MΩ, FHC Inc., Bowdoin, ME, USA) for semi-chronic recordings in V2. The recorded signals were amplified 20000 fold for monkey T and 8000 fold for monkey B (4x by a wideband preamplifier MPA32I, 5000x by a PGA 64 (2000x monkey B), 1-5000 Hz, both Multi Channel Systems GmbH, Reutlingen, Germany) and digitized with 25 kHz sampling rate at 12 bit ADC resolution. Signals were referenced against the recording chamber, which is a titanium cylinder (25 cm diameter) enclosing the areas of interest of the visual cortex with good contact to skull bone and dura mater. The electric pulses were generated by an electric stimulus generator (STG 4008-1.6 mA, Multi-Channel Systems GmbH, Reutlingen, Germany) connected to a glass-insulated microelectrode located in V2. Each pulse was biphasic, starting with 100 µs of negative current, followed by 60 µs with no current application and 100 µs of positive current. The strength of each pulse was either ± 15 µA or ± 25 µA. The effects evoked by the different strengths of the current pulses were not significantly different and were therefore pooled for analysis. The time of electric stimulation was random within the last half of each MC (550 – 950 ms), resulting in 2 to 4 stimulations within a single trial. To avoid saturation and long-lasting discharge times of the PGA, it (and all following components) was disconnected from the animals for 300 µs around each pulse application (starting simultaneously with pulse application).

### **Data analysis**

Customized Matlab scripts (version R2016b, MathWorks, Natick, MA, USA) were used for all offline analyses and procedures stated below. Since the electrical stimulation caused large, exponentially decaying artifacts, we developed an offline procedure to extract the artifacts from the actual data before further analyses, which reliably restores the original underlying broadband signal. This procedure and its characteristics are described in Chapter 5, in detail.

### **Verification of electrode positions**

The correct positioning of semi-chronic microelectrodes in V2 was verified during the placement of these electrodes before the actual task recordings began. We based the verification on the changes of the RF-sizes along the electrode tracks through area V1 to V2 (an increase of  $1^\circ$  when reaching V2), as well as by the polarity of the onset transient as described by Schroeder et al., 1998<sup>39</sup>. Furthermore, we required an immediate jump in the eccentricity of RFs caused by the electrode crossing of the vertical meridian between V1 and V2. RF-sizes were estimated based on a bar-mapping paradigm explained in Drebitz et al., 2019<sup>187</sup>. For evoking large onset-transients as required for assessing in which cortical layer the electrode tip was located, we used a checkerboard pattern ( $8^\circ \times 8^\circ$ , 100 % Michelson contrast). This pattern consisted of 64 square-shaped fields ( $1^\circ \times 1^\circ$ ) and was flashed for 250 ms on screen while animals fixated the central FP and had to detect a decrease in luminance of the FP. After presenting a pattern for 250 ms, a reversed pattern of white and black fields was flashed on the screen for 250 ms. This change of checkerboard patterns was repeated between 8 to 16 times depending on trial duration (between 2 to 4 s). Onset-transients of an electrode within a specific depth were then averaged across checkerboard pattern changes, and the symmetry assessed. Based on previous work investigating the polarity and shape of visually evoked potentials across cortical layers<sup>196</sup> the respective electrode tips layer location was determined.

Each V4 recording site was similarly classified into being located either in superficial or input-layers based on the polarity and shape of the onset-transient evoked by visual stimulus onset<sup>39,197</sup>. The classification was based on a principle component analysis (PC1, PC2) of mean LFP-values (of a recording site for both attentional conditions) starting 50 ms after visual stimulus onset to 300 ms after (see chapter 2.3, supplements).

For each session, V4 and V2 RF positions and outlines were mapped manually based on multi-unit- and LFP-responses to bar stimuli. Based on these estimates, stimulus locations were chosen such that two stimuli were located within the same V4 RF equidistant to the FP, but each in a separate V2 RF. The stimulus locations in the upper visual quadrant were point mirrored across the FP.

### **Data selection**

As mentioned before, we ensured the correct stimulus positioning within the V4 and V2 RFs before each recording session based on manually mapping the RF outlines. Furthermore, each V4 recording site used for further analyses had to deliver on average over MCs 2/3 at least 50 %

higher  $\gamma$ -band power than during baseline-period (spontaneous activity), for the two stimulus conditions containing one stimulus within the V4 RF. These conditions did not contain electrical stimulations. The  $\gamma$ -band power was calculated by first band passing the raw-signal between 5 – 170 Hz using an equiripple FIR-filter in forward and backward direction. This band-limited signal was then down sampled to 1000 Hz and its power calculated by performing a Morley's wavelet-transform (see Drebitz et al., 2018 for details). The frequency-resolved power-values obtained during task-performance were normalized to the mean power-spectra values obtained during baseline-periods by first subtraction followed by division. We defined the  $\gamma$ -band for each animal individually based on the full-width at half maximum of the mean normalized power spectra (between 30 – 100 Hz) of all task conditions requiring the monkeys to focus attention on the V4 RF. Another selection criterion for recording-sites was that animals' performance was better or equal to 80 % correctly performed trials (33 % chance level, disregarding errors related to eye-movements  $> 0.5^\circ$  away from the FP). For analyses regarding multi-unit activity all stimulations (up to 4 within a trial) were considered if, there were more than 150 ms between pulse application and behavioral response. For analysis of RT modulations, only the last stimulation preceding the behavioral response was considered, if there were more than 150 ms between pulse application and behavioral response.

### **Phase estimation**

For estimating the V4  $\gamma$ -phases, the recorded raw signals (1-5000 Hz, 25 kHz sampling rate, electrical artifacts removed) were band-passed in a broad  $\gamma$ -frequency range (35-120 Hz) using an equiripple FIR-filter in forward, and backward direction and subsequently down-sampled to 1000 Hz. The phases of this  $\gamma$ -band limited signal were then estimated, performing a Hilbert transform, which delivers estimates of the instantaneous phase  $\phi(t)$  and amplitude  $A(t)$  of the signal at time  $t$ <sup>198,199</sup>.

### **Spiking-Activity**

For analyzing spiking activity in V4, we used a more sensitive measure for detecting spiking activity in signals with rather low SNR as standard methods based on amplitude thresholding are<sup>187</sup>. Since this measure does not reject subthreshold spikes, it takes into account the entire spiking activity (ESA). For calculating the ESA-signal, the raw-signal (stimulation artifacts removed) was first high-pass filtered in forward and backward direction (equiripple FIR-Filter,  $>300$  Hz). The high-passed signal was subsequently full-wave rectified and low-pass filtered using a Gaussian kernel with  $\sigma = 1$  ms and a window size of 2 ms, again in forward and backward direction (see Drebitz et al., 2019 for details). To extract the intrinsic  $\gamma$ -phase relation

of ESA, we generated a surrogate data set based on trials without electrical stimulation, but equal visual stimulation (as in target and distractor-stimulated trials) and cut out data-sections centered around the actual stimulation times of trials with stimulation. The assignment of stimulation times to non-stimulated trials was random. We performed this procedure 50000 times, resulting in a surrogate data set representing the same trial periods as the stimulated data and originating from the same recording sites. We then estimated the  $\gamma$ -phases and calculated the ESA for the surrogate data equal to the procedures described above for the stimulated data. The surrogate data were then sorted into  $\gamma$ -phase groups of  $60^\circ$  width as the actual data ( $1^\circ$  step size) and the mean ESA for the surrogate data of each window was calculated. This mean ESA of surrogate data was subsequently subtracted from the mean ESA-values of phase sorted stimulation data. This subtraction removed the intrinsic  $\gamma$ -phase dependence of ESA, for identifying  $\gamma$ - phase-dependent effects of electrical stimulation on ESA.

### **Sinusoidal Fit**

The modulation of RTs and ESA across phases was estimated based on a sinusoidal fit. The described curve fitting was performed using the Matlab curve-fitting toolbox (MathWorks, Natick, MA, USA). The median RT- and mean ESA-values (for a 3 ms time window) across phases (binned in  $60^\circ$  windows and step size of  $1^\circ$ ) were fit to the function:

$$y(\phi) = A * \sin(1 * x + b) + o,$$

with  $A$  as amplitude-,  $b$  the phase- and  $o$  the offset-parameter being free adjustable parameters without further restrictions. The frequency of the function was fixed to 1.

### **Statistical evaluation**

For evaluating whether the modulation depth as estimated by fitting a sinusoidal function to the data was significant, we performed a shift-predictor procedure for RTs and ESA-values. For this,  $\gamma$ -phase values were randomly assigned to RT- or ESA values, and the modulation depth of this unrelated data was calculated based on a sinusoidal fit. This procedure was repeated 1000 times, each time with new randomly assigned  $\gamma$ -phase/RT or  $\gamma$ -phase/ESA-value relations. For calculating the shift-predictor of ESA modulations, we used data of non-stimulated trials but kept the  $n$  equal to the actually stimulated data set.

By performing this shift-predictor procedure 1000 times, we estimated the significance threshold ( $p < 0.05$ ) Interval of modulation depth for RTs with random  $\gamma$ -phase relations. For ESA-modulation, we used only the maximum modulation depth of a given permutation across

time (30 ms). This procedure accounts for the multiple-comparison correction across time<sup>200</sup>.

## 2.3 Supplements

For the analysis of  $\gamma$ -phase-dependent modulation of multi-unit activity, we sorted recording sites according to their depth within the V4 column. This was necessary due to the potentially different response times of neurons located in different layers to our electrical stimulation<sup>196</sup>. We based the sorting on a principal component analysis (PCA) of the onset VEPs to visual stimulation for each recording site. PC1 and PC2 values of each site were used to define clusters in PC1 x PC2 space (Fig. 10 A/C), these clusters were defined based on an iterative procedure to minimize the point-to-centroid distance across a predefined number of clusters as implemented in Matlab (function name: kmeans; The MathWorks Inc., Natick, MA, USA)<sup>201,202</sup>.

Figure 10 A shows the PCA values of monkey B in PC1 x PC2 space. The PCA revealed that recording sites form one cluster (cluster 1) and a second “cluster” of outliers (cluster 2). The mean VEP across recording sites sorted into cluster 1, as well as the individual mean VEPs for each recording site, shows the high similarity of VEP shapes between these sites (Fig. 10B). They share two specific features, which are a positive peak at 70 ms and a negative peak at 100 ms after stimulus onset. These features are characteristic for VEPs of neurons located in layer 4<sup>197</sup>.

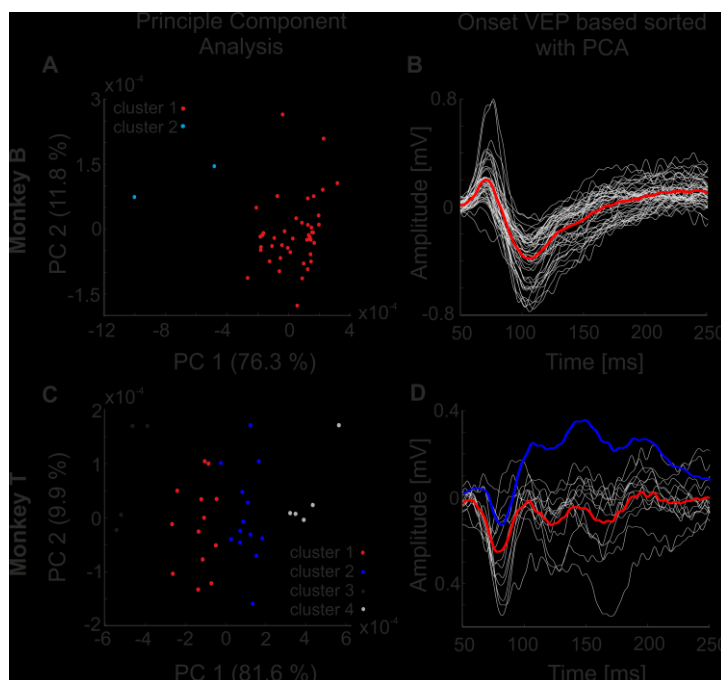


**Figure 10:** *A* Principle component analysis (PC1 and PC2) of mean visually evoked potentials (VEPs) to stimulus onset of target and distractor stimulated conditions for monkey B. *B* Individual mean VEPs of recording sites (light gray) defined as cluster 1 (in A) and the average mean VEP from 50 to 250 ms after stimulus onset (red). *C* same as in A but for monkey T. Four clusters were formed based on the PCA. *D* Average mean VEPs for clusters 1 (red) and 2 (blue) from 50 to 250 ms after stimulus. The light gray traces represent individual mean VEPs of recording sites constituting cluster 1. These sites were used for further analysis.

## Chapter 2

We performed the same procedure for monkey T but required the separation of recording sites into four groups (Fig. 10C). For monkey T, the separation between sites with negative and positive PC1 values (clusters 1 and 2) was necessary due to their different VEP shape 100 ms after stimulus onset (Fig. 10 D). Due to this difference in shape, as well as the poor multi-unit activity for sites sorted into cluster 2, we used only sites sorted into cluster 1 for further analysis. The shape features of both clusters are characteristic for recording sites in superficial layers and are clearly distinct from monkey B recording sites located in layer 4<sup>197</sup>. Clusters 3 and 4 comprised only small fractions of data and were therefore not taken into further account.

## Chapter 3

### 3.1 Attention Configures Synchronization within Local Neuronal Networks for Processing of the Behaviorally Relevant Stimulus

Declaration on the contribution of the candidate to a multi-author article, which is included as a chapter in the submitted doctoral thesis.

Experimental concept and design:	50 %
Data acquisition:	50 %
Data analysis:	100 %
Data interpretation:	60 %
Preparation of Figures and Tables:	100 %
Drafting of the manuscript:	60%

Date:

Signature:

This chapter was published as: *Drebitz, E., Haag, M., Grothe, I., Mandon, S. & Kreiter, A. K. Attention configures synchronization within local neuronal networks for processing of the behaviorally relevant stimulus. Front. Neural Circuits 12, 71 (2018).*

## **Attention Configures Synchronization within Local Neuronal Networks for Processing of the Behaviorally Relevant Stimulus**

Eric Drebitz<sup>1</sup>, Marcus Haag<sup>1</sup>, Iris Grothe<sup>1</sup>, Sunita Mandon<sup>1</sup>, Andreas K. Kreiter<sup>1</sup>

<sup>1</sup> Brain Research Institute, Center for Cognitive Sciences, University of Bremen

### **3.1.1 Abstract**

The need for fast and dynamic processing of relevant information imposes high demands onto the flexibility and efficiency of the nervous system. A good example for such flexibility is the attention-dependent selection of relevant sensory information. Studies investigating attentional modulations of neuronal responses to simultaneously arriving input showed that neurons respond, as if only the attended stimulus would be present within their receptive fields (RF). However, attention also improves neuronal representation and behavioral performance, when only one stimulus is present. Thus, attention serves for selecting relevant input and changes the neuronal processing of signals representing selected stimuli, ultimately leading to a more efficient behavioral performance. Here, we tested the hypothesis that attention configures the strength of functional coupling between a local neuronal network's neurons specifically for effective processing of signals representing attended stimuli. This coupling is measured as the strength of  $\gamma$ -synchronization between these neurons. The hypothesis predicts that the pattern of synchronization in local networks should depend on which stimulus is attended. Furthermore, we expect this pattern to be similar for the attended stimulus presented alone or together with irrelevant stimuli in the RF. To test these predictions, we recorded spiking-activity and local field potentials (LFP) with closely spaced electrodes in area V4 of monkeys performing a demanding attention task. Our results show that the  $\gamma$ -band phase coherence ( $\gamma$ -PhC) between spiking-activity and the LFP, as well as the spiking-activity of two groups of neurons, strongly depended on which of the two stimuli in the RF was attended. The  $\gamma$ -PhC was almost identical for the attended stimulus presented either alone or together with a distractor. The functional relevance of dynamic  $\gamma$ -band synchronization is further supported by the observation of strongly degraded  $\gamma$ -PhC before behavioral errors, while firing rates were barely affected. These qualitatively different results point toward a failure of attention-dependent top-down mechanisms to correctly synchronize the local neuronal network in V4, even though this network receives the correctly selected input. These findings support the idea of a flexible, demand-dependent dynamic configuration of local neuronal networks, for performing different functions, even on the same sensory input.

### 3.1.2 Introduction

Successful and goal directed behavior within our complex world requires a dynamic and adaptive processing of relevant information. Thus, local neuronal networks are required to perform different functions depending on the current requirements of information processing. A well-known example for such adaptation of network functions is the attention-dependent selection of different subsets of afferent input for effective processing of relevant visual information. Several studies investigating responses of neurons to simultaneous and convergent input showed that neurons responded almost as if only the attended stimulus would be present within their receptive field (RF)<sup>54,90,91,113,115,183</sup>. Such changes of network function quickly follow changing behavioral demands although anatomical connections cannot change on such short timescales<sup>203-205</sup>. However, recent theoretical work indicates that modulating  $\gamma$ -band synchronization can change the strength of the functional coupling between neuronal populations. Selective synchronization of a local network with only those upstream inputs representing the attended stimulus could therefore constitute a mechanism underlying this attention-dependent bias of neuronal responses<sup>179,206-210</sup>. We and others showed indeed that the strength of  $\gamma$ -band phase coherence ( $\gamma$ -PhC) between V1 and V4 populations with overlapping receptive fields (RF) was much stronger when the V1 population represented the attended instead of the non-attended stimulus<sup>183,184</sup>. These theoretical and experimental results indicate that attention-dependent selective processing of relevant afferent input depends on the strength of functional coupling between neurons along the visual pathway.

Yet, attention also modulates perception and neuronal responses when there is no competition between inputs. With only one stimulus inside the RF, attention has been shown to increase firing rates<sup>91,211-213</sup>, to reduce the response variability of individual neurons<sup>86,95,97</sup> and to reduce the shared response variability of neuronal populations<sup>86,96,98</sup>. Thus, besides the selective routing of relevant information, attention also modifies network functions for improving the processing of a single attended stimulus. Such modifications could be obtained by reorganizing the network's internal pattern of functional connections by changing the pattern of  $\gamma$ -band synchronization<sup>112,149,178,182,206,214-218</sup>.

Based on these considerations, we hypothesized that effective processing of an attended stimulus requires a specific configuration of local neuronal networks in visual cortex. This attention-dependent and stimulus-specific configuration of a local network is established by a specific pattern of  $\gamma$ -band synchronization between neurons processing the attended stimulus.

From this hypothesis, we derive three simple predictions: (1) In the presence of multiple stimuli in the population receptive field (pRF) of a local network, the pattern of  $\gamma$ -band synchronization and hence, the corresponding configuration of functional connections should depend on the attended stimulus. (2) If this pattern would indeed be stimulus specific, it should be very similar to the pattern observed, if only the attended stimulus is present. (3) Deviating patterns of  $\gamma$ -band synchronization should reflect erroneous network configurations and go along with deteriorated behavioral performance.

To test the hypothesis, we recorded neuronal activity in area V4, using two closely spaced microelectrodes, while monkeys attended one of two stimuli within the RF. The stimuli were placed within the V4 pRF such that they induced local synchronization and responses of different strength. We found that switching attention between these two stimuli resulted in local  $\gamma$ -band synchronization strength almost as if the attended stimulus would be present without nearby distractor. Behavioral errors were preceded by local synchronization deviating strongly from that observed for successfully executed trials, while spiking activity showed only small differences between successful and wrong task execution.

### 3.1.3 Materials and Methods

#### Surgical Preparation

Two male macaque monkeys (*Macaca mulatta*) were implanted under aseptic conditions with a titanium head holder and a recording chamber above area V4. The target area was identified by evaluation of MRI-scans performed before surgery. All procedures were approved by the local authorities (Der Senator für Gesundheit, Bremen, Germany) and were in accordance with the regulation for the welfare of experimental animals issued by the Federal Government of Germany and with the guidelines of the European Union (2010/63/EU) for care and use of laboratory animals.

#### Behavioral Task

The animals performed a highly attention-demanding shape-tracking task. In the following, for task parameters differing between individuals, the parameters for monkey T are mentioned in the text and those for monkey B follow in brackets. Visual stimuli were presented on a 20-inch CRT-monitor with a resolution of  $1024 \times 768$  pixels ( $1152 \times 864$  pixels) and a refresh rate of

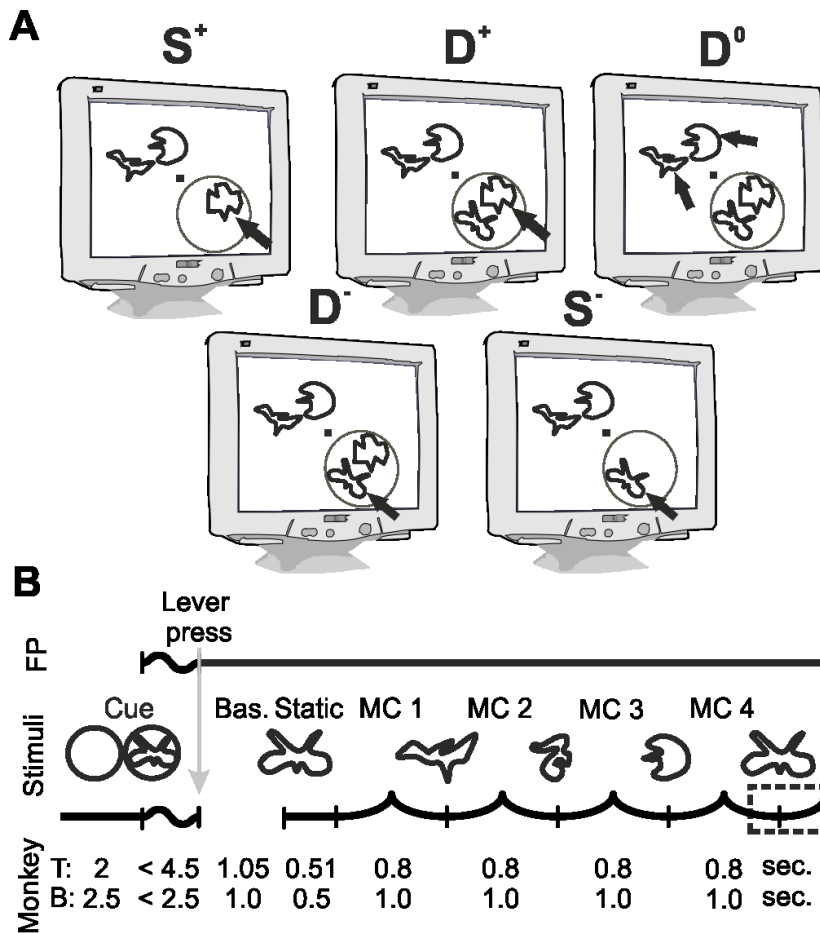


**Figure 11:** Stimulus configuration and temporal structure of the shape-tracking task. **A**, Schematic illustration of task conditions. Black arrows indicate the cued target stimulus; other stimuli serve as distractors. The RF of the recording site in V4 is depicted as a grey circle, which does not appear on the display. Trials could contain either one or two stimuli in the V4 RF. The abbreviations indicate the number of stimuli within the RF (“S” for single and “D” for double presentation in the V4 RF) and the direction of attention to either the stimulus inducing higher “+” or lower values “-” of spiking activity or  $\gamma$ -synchronization. The condition with two stimuli in the RF but attention directed to stimuli in the opposite hemi-field is referred to as D<sup>0</sup> (Double Attend Out). **B**, Temporal structure of the shape-tracking task. During the cueing period, a spatial cue was present on screen. The cue was a simple ring for monkey T and a ring enclosing the upcoming target shape for monkey B. After appearance of the fixation point (FP), monkeys started fixation and initiated the trial by pressing a lever. Simultaneously, the spatial cue disappeared (faded within 200 ms for monkey B). After a baseline period (Bas.), followed by static presentation (Stc.) of the initial shapes at each location, they morphed through a sequence of different shapes until the initial shape at the cued location reappeared. Monkeys had to signal this reappearance within a response period indicated by the dashed rectangle. Bas, baseline period; Cue, Cueing period; FP, fixation point; MC, morph cycle; Stc, static presentation period.

100 Hz. The screen was placed 90.5 cm (92 cm) in front of the monkey that was sitting in a custom-made primate chair. Visual stimulation comprised a fixation point and up to four simultaneously presented complex shapes (Figure 11A). Figure 11B shows the sequence of stimuli and events of a single trial: It starts with the appearance of a spatial cue, which indicates the position of the behaviorally relevant stimulus in the upcoming trial. During this period of the trial animals were allowed to move their eyes freely. The spatial cue consisted of a 1° (1.5°) diameter ring with a linewidth of 0.04° (0.075°) centered over the position of the upcoming target stimulus. For monkey B, the cue contained in addition the initial shape of the upcoming trial, because it helped to increase performance during training of the task. After 2.0 s (2.5 s) a central 0.15°

× 0.15° fixation point (FP) appeared, which required the animals to start fixation and subsequently to initiate the trial by pressing a lever inside the primate chair within 4.5 s (2.5 s). Following trial start, the spatial cue disappeared (faded within 200 ms) and a baseline period of 1050 ms (1000 ms) began. Subsequently the static presentation period started with the appearance of three or four differently shaped stimuli, all at the same eccentricity between 2.5° and 3.5° (2.1°-2.5°) of visual angle (Figure 11A). Either one or two adjacent stimuli were located in the lower visual field quadrant contralateral to the recording sites in area V4. The other two stimuli appeared at positions mirrored across the FP in the upper, ipsilateral visual field quadrant. The stimuli presented at each of the four positions differed in color (red, green, yellow, blue; luminance: 3.7–5 cd/m<sup>2</sup>, background luminance: 0.03 cd/m<sup>2</sup>). The assignment of these colors to the four stimulus positions was constant throughout a recording session. Stimuli at all locations could serve as target. The initial complex shapes at each stimulus location were presented statically for 510 ms (500 ms) and subsequently started to morph continuously into other complex shapes (see also: Taylor et al., 2005<sup>103</sup>; Grothe et al., 2012<sup>183</sup>). A single morphing cycle (MC), i.e., morphing completely from one shape into another shape, lasted 800 ms (1000 ms). Trials consisted of two to four MCs. All shapes were taken randomly with equal probability out of a set of 8 shapes (6 shapes). The reappearance of the initial shape at the cued stimulus location required the monkeys to release the lever within a time window ranging from 310 ms before the shapes' complete reappearance to 400 ms afterwards (–350 ms to 150 ms; Figure 11B, dashed rectangle). The appearance of the targets' initial shape within the sequence of MCs at the distractor locations or the distractors own initial shape had to be ignored. For monkey T, all 8 shapes could become initial shape, whereas for monkey B, the initial shape of the target stimulus was always the same, within and across sessions. Throughout the whole trial, the eye position was monitored by video-oculography (monkey T: I Scan Inc., Woburn, MA, USA; monkey B: custom-made eye tracking system) and the direction of gaze was not allowed to deviate from the FP by more than 0.5°. If monkeys released the lever within the response window, they were rewarded with a small amount of diluted fruit juice. If they broke fixation or responded outside the response window, trials were aborted without reward.

### **Recording Procedure**

Simultaneous intracortical recordings in the upper layers of visual area V4 were performed using two epoxy-insulated tungsten microelectrodes (1–3 M $\Omega$ , shank diameter 125  $\mu$ m FHC Inc., Bowdoin, ME, USA; 330  $\mu$ m distance between shanks). The electrode signals were

amplified 4000x (1000x) (monkey T: 4x by a wideband preamplifier MPA32I and 1000x by a PGA 64, 1-5000Hz, both Multi Channel Systems GmbH, Germany; monkey B: same setup but gain factor 10 for preamplifier and 100 for PGA) and digitized with 25 kHz sampling rate and 12 bit (16 bit) ADC resolution. The reference electrode for monkey T was the recording chamber, a titanium cylinder of 25 mm diameter implanted into the bone and touching the dura. The electrode signals of monkey B were referenced to a low impedance electrode ( $<0.1 \text{ M}\Omega$ ), positioned on top of an epidural array (contacting the bone), placed above area V1. Before recordings, the pRF for each recording site was mapped manually as the minimal response field based on multi-unit and LFP-responses, while the animals performed a fixation task. Both microelectrodes were placed such that the recorded neurons shared major parts of their pRFs. Locations and colors for the two stimuli within the overlapping pRFs were chosen such that they caused responses of different strength.

### **Data Analysis**

Customized scripts for Matlab (version R2013a, MathWorks, Natick, MA, USA) were used for all offline data analysis procedures described below. Data were analyzed for the spiking activity of a small group of neurons by calculating the entire spiking activity (ESA). As a measure for the strength of functional coupling, we calculated the PhC between two signals, either representing the overall local population activity (LFP) and the activity of a small group of neurons (ESA-LFP PhC) or the activity of two separate groups of neurons of the same local network (ESA-ESA-PhC). For analysis of spiking activity, we used the ESA-signal because it is more sensitive in detecting neuronal responses in data with low signal to noise ratio, since it does not reject sub-threshold events. Furthermore, the independence from thresholding provides the advantage of integrating over all spikes (even small ones) of a population, resulting in a more complete estimate of the actual population response. The ESA of neurons near the recording electrode's tip (50  $\mu\text{m}$  radius according to Brosch et al., 1997<sup>219</sup>) was obtained by band-passing the raw signal using a FIR-filter between 0.3 and 12.2 kHz in forward and backward direction (to avoid phase shifts). Subsequently, the band-limited signal containing the spiking activity was fullwave rectified and low-pass filtered (forward and backward) at 160 Hz and down-sampled to 1 kHz<sup>220,221</sup>. As opposed to standard multi-unit activity, this procedure delivers a continuous instead of a binary signal, which is known to represent the spiking activity of multiple neurons surrounding the electrode tip<sup>222</sup>. ESA-responses were obtained by subtracting for each recording site the mean spontaneous activity from the ESA values recorded

during the analysis period. Spontaneous activity was estimated as the average ESA taken from 150 ms (250 ms) after the baseline period started to its end over all correctly performed trials of a recording session. Note, that during baseline period (Fig. 11B) no visual stimulus but the FP was present on screen. The LFP was obtained from the recorded signal by low-pass filtering with a FIR-filter (-3 dB point at 170 Hz) in forward and backward direction and subsequent down sampling to 1 kHz.

The time-frequency decomposition of ESA and LFP signals was performed by convolving the signals with complex Morlet's wavelets  $\omega(t, f_0) = A \exp(-t^2/2\sigma_t^2) \exp(2i\pi f_0 t)$ , with  $\sigma_f = 1/2\pi\sigma_t$ . Morlet's wavelets have a Gaussian shape both in time (SD:  $\sigma_t$ ) and frequency dimension (SD:  $\sigma_f$ ) and were normalized such that their total energy was 1. The normalization factor  $A$  was defined as:

$$A = (\sigma_t \sqrt{\pi})^{-0.5}. \quad (1)$$

Central frequencies  $f_0$  of the Morlet's wavelets ranged from 5 to 160 Hz according to the scheme described by Torrence and Compo (1998)<sup>223</sup> with a ratio of  $\frac{f_0}{\sigma_f} = 6$ <sup>103,224</sup>. The wavelet transform provides complex coefficients  $\tilde{x}_j^r$  for electrode  $j$  and trial  $r$  at time  $t$  and frequency  $f$ , which can be expressed as their amplitude  $A$  and phase  $\Phi$ :

$$\tilde{x}_j^r(t, f) = A_j^r(t, f) e^{i\Phi_j^r(t, f)} \quad (2)$$

The frequency-dependent power of LFP and ESA-signals was computed by taking the square of the absolute value of the convolution's result and dividing it by the Nyquist frequency (500 Hz). The phase component for each time and frequency bin was used for estimation of PhC over  $N$  trials, between electrodes  $j$  and  $k$ , as follows (see also: Lachaux et al., 1999<sup>225</sup>; Grothe et al., 2012<sup>183</sup>):

$$PhC(t, f) = \left| \frac{1}{N} \sum_r e^{i\Phi_j^r(t, f) - i\Phi_k^r(t, f)} \right| \quad (3)$$

The PhC was calculated for each electrode pair, thus delivering one ESA-ESA measure and two ESA-LFP pairs (as both sites of the pair can deliver either the ESA or the LFP) for PhC analyses. ESA and LFP signals were never taken from the same electrode to avoid the possibility that the same spike contributed to ESA and LFP. PhC values were bias-corrected by subtracting the expected value (EV) for the PhC, as estimated from the same number trials ( $N$ ) with random phase relations<sup>183</sup>

$$EV(N) = \frac{\sqrt{\pi}}{2\sqrt{N}} \quad (4)$$

For the analysis of PhC and power in the  $\gamma$ -band ( $\gamma$ -PhC,  $\gamma$ -power), we defined the  $\gamma$ -bands for

each animal and measure separately. For this purpose, we computed power and PhC-spectra in the period of MCs 2 and 3. The power spectra of each recording site were normalized by the mean power spectrum obtained during the baseline period of all trials in all conditions of that respective recording site, by first subtraction and then division by the baseline period's spectrum. Subsequently we averaged the normalized power spectra and PhC-spectra of all recording sessions and experimental conditions. The extent of the  $\gamma$ -band was determined based on the full width at half maximum of the mean PhC- and power-spectra respectively (Fig. 12D, highlighted in gray).

The analysis of behavioral errors required pooling of trials across sessions. This excluded PhC as measure for synchronization since PhC requires a constant preferred phase difference across trials. This requirement might not be fulfilled for trials coming from different recording sessions. Therefore we used the magnitude squared coherence (MSC, see also: Carter et al., 1973) which can be computed within single trials and subsequently averaged over trials. To obtain the MSC we first calculated the complex coherence values  $\gamma_{jk}(t, f)$  between the signals of electrodes  $j$  and  $k$  at each time ( $t$ ) and frequency ( $f$ ) bin. This is achieved by multiplying for each trial the complex wavelet coefficient  $\tilde{x}_j^r(t, f)$  with the complex conjugate of  $\tilde{x}_k(t, f)$  to obtain the cross spectral density and normalizing it to the square root of the product of their auto spectral densities (again calculated by multiplying the complex wavelet coefficients with complex conjugates, but here of the same signal; complex conjugates are indicated by an overbar):

$$\gamma_{jk}(t, f, r) = \frac{\tilde{x}_j^r(t, f) * \overline{\tilde{x}_k^r(t, f)}}{\sqrt{(\tilde{x}_j^r(t, f) * \overline{\tilde{x}_j^r(t, f)}) (\overline{\tilde{x}_k^r(t, f)} * \tilde{x}_k^r(t, f))}} \quad (5)$$

Subsequently, the absolute value of the complex coherence  $\gamma_{jk}(t, f)$  is squared<sup>226</sup>:

$$MSC(t, f, n) = |\gamma_{jk}(t, f, n)|^2 \quad (6)$$

MSC-values were then averaged over trials. The time and frequency resolved MSC was bias-corrected by subtracting corresponding values derived from a shuffle predictor<sup>134,227</sup>. This shuffle predictor was obtained by computing 1000 times the MSC between ESA and LFP from randomly shuffled trials and averaging the results for each frequency bin. For computation of the MSC in the  $\gamma$ -band ( $\gamma$ -MSC) we defined a  $\gamma$ -band based on MSC spectra by the same procedure as described above for the  $\gamma$ -PhC.

## Experimental design and statistical analysis

This study includes physiological and behavioral data of two adult male macaque monkeys. The concept of the study demands two stimuli within the same pRF, each of them evoking a specific configuration of the local neuronal network in V4. As quickly accessible indicators for such a difference during the experimental sessions, we used response strength in firing rate and LFPs. We arranged position and color of the individual stimuli within the V4 pRF such, that the response strengths were clearly different. To characterize the local processing of different, behaviorally relevant stimuli with and without distractor within the V4 pRF, the task paradigm comprises five different conditions.

The two conditions with only one of the two possible stimuli presented inside the pRF are indicated by an “S” for single stimulus presentation whereas the other conditions with both stimuli present are indicated by a “D” for double stimulus presentation. In the double conditions, each of the two stimuli could serve as the target of attention. In order to investigate whether processing of a relevant stimulus implies the same network configuration in absence as well as presence of a competing distractor we required also in the single conditions attention to the stimulus within the pRF. This ensures a demand to configure a network for processing the same stimulus in corresponding S and D conditions.

Single and double conditions were labeled by a “+” or a “-“ sign, depending on the stimulus in the pRF that was attended. Separately for each of the three measures (ESA-responses, ESA-LFP  $\gamma$ -PhC and ESA-ESA  $\gamma$ -PhC) the labels “+” and “-“ were assigned to the stimuli evoking the higher respectively lower values when presented alone. Thus, a stimulus inducing the stronger ESA-responses did not always also induce the higher  $\gamma$ -PhC (i.e. the same stimulus could be labeled “+” for ESA-responses and “-“ for  $\gamma$ -PhC). For comparison of our ESA results to earlier work we also included a double condition with attention directed away from the pRF ( $D^0$ ). Together this results in five attentional conditions:  $S^+$ ,  $S^-$ ,  $D^+$ ,  $D^-$  and  $D^0$ .

The rationale of the study required that the individual recording sites or site pairs had to fulfill the following criteria to be included in the analysis: 1) Recording sites had to be located in the upper cortical layers. 2) Neurons needed to respond significantly to each of the stimuli presented alone within the pRF, as measured by ESA response for measures including ESA and by  $\gamma$ -LFP power for measures including LFP. 3.) The values of ESA-responses or  $\gamma$ -PhC (depending on the analysis) for the two single stimulus conditions had to be sufficiently different to make sure the stimuli were driving the local population differently.

Criterion 1) was applied to avoid comparing of phase relations between neurons and overall

population activity of different layers. Due to the typical recording procedure (lowering the electrode only until the first responses were found), this meant that recordings happened most likely in the upper layers. The location in the upper cortical layers was verified by the polarity of the evoked potential caused by stimulus onset<sup>228</sup>. The significant activation (criterion 2) of neurons during the analysis window (MC 2/3, for explanation see below) was tested for ESA-values or LFP  $\gamma$ -power (depending on which measure was used for PhC estimation) against the respective values during the baseline period (starting after 150 ms (250 ms for monkey B) to its end; Wilcoxon signed-rank test, critical  $\alpha$ -level: 0.05).

A sufficient difference of values during single conditions (criterion 3) was required for evaluating whether the ESA-response or  $\gamma$ -PhC observed in a double condition is more similar to the corresponding value observed in the  $S^+$  or in the  $S^-$  condition. Therefore, only sites or site pairs were considered, in which the analyzed measure differed by at least a factor of 1.33 between the two single conditions.

All analyses (with the exception of the error trial analysis) were performed within a time window comprising MCs 2 and 3 (Fig. 12A, gray background). This analysis window was chosen because the target shape never appeared in MC 1, and at latest in MC 4. Therefore, attentional demands might be reduced during these periods. If the initial shape reappeared at the cued location at the end of MC 2 or 3, the time window ended 200 ms prior to the behavioral response. To exclude the potential survival of response related effects (as described by Mirabella et al., 2007)<sup>229</sup>, we performed a control analysis with a cutoff period of 350 ms before the behavioral response. Neither for ESA-rates nor ESA-LFP  $\gamma$ -PhC we found differences of the sizes of effects or the level of significances. Individual values differed only marginally (on average by around 1 %) as compared to our original values.

For quantitative analysis of the effect of attention on ESA-responses and  $\gamma$ -PhC across sessions and animals, the mean values for each of the five different attention conditions observed for a recording site or recording site pair were normalized by dividing them by the average of these five values. The statistical analysis was performed using non-parametric Wilcoxon signed-rank tests and Wilcoxon rank-sum tests at a critical  $\alpha$ -level of 0.05. In case of multiple comparisons, all p-values were Bonferroni corrected, except for p-values that were already higher than the critical  $\alpha$ -level of 0.05 before Bonferroni correction.

To investigate potential relations between neuronal activity patterns and behavioral performance, we compared ESA-responses and the synchronization of ESA with the LFP between correctly performed trials and trials terminated by a false alarm during MC 2/3. The selection criteria for contributing recording sites and site pairs were the same as described

above. Because of their small number, the false alarm trials were pooled across sessions for each animal separately and MSC instead of PhC was used as a measure of synchronization (see above). For the analysis, a time window of 400 ms (monkey B: 500 ms) aligned to and ending 200 ms before the behavioral response was used. Thus, the duration of the time window was equivalent to half of a MCs' duration. For quantifying the differences between false alarms and correctly executed trials, 1000 randomly compiled sets of correctly performed trials were generated. For each set, we randomly selected the same number of correctly performed trials from each session as the session contributed false alarms. From these 1000 sets of correctly performed trials, the distributions of  $\gamma$ -MSC values were computed within the same time windows as for the corresponding false alarm trials in the corresponding sessions. The pooling procedure and random selection of trials was identical for investigating ESA-responses. Based on these distributions, we estimated the z-score values for  $\gamma$ -MSC and ESA-responses observed in the false alarm trials in comparison to correctly performed trials and derived corresponding confidence levels (probability derived from z-score chart).

### 3.1.4 Results

We investigated attention-dependent changes of local network configuration in visual area V4 of two macaque monkeys, while the animals performed an attention-demanding shape tracking task<sup>103,183</sup>. Briefly, animals had to covertly attend one of three or four stimuli with different shapes, colors and luminance, of which one was previously cued (Fig. 11A). After static presentation, the shapes of all stimuli started morphing into other, randomly selected shapes, color and luminance did not change (Fig. 11B). Trials could contain up to four such MCs. Animals were required to detect the reappearance of the initial shape at the cued location. Animals broke fixation in 5.5 % (monkey T) and 24.9 % (monkey B) of trials respectively, the average performance disregarding fixation errors was 87.1 % and 93.3 % correct trials for monkey T (28 recording sessions) and B (34 recording sessions), respectively. In 6.6 % (monkey T) and 3.8 % (monkey B) of all trials (across all stimulus conditions), the response occurred before reappearance of the initial shape (false alarms), and in 6.3 % (monkey T) and 2.9 % (monkey B) the response occurred too late (misses). For trials with attention directed to a stimulus inside the pRF, the proportion of false alarms differed significantly for one animal between trials with one and two stimuli in the pRF (monkey T: with distractor in pRF 6.8 %, without distractor 5.1 %,  $z = 2.5504$ ,  $p = 0.0108$ ; monkey B: with distractor in pRF 2.0%,

without distractor 2.2%,  $z = -0.561$ ,  $p = 0.5748$ ; Wilcoxon signed-rank test).

To investigate attention-dependent modulations of  $\gamma$ -PhC and ESA-responses within local V4 networks, we recorded simultaneously with two closely spaced microelectrodes (330  $\mu\text{m}$  distance between shanks) from 118 recording sites in supragranular layers 2/3 (monkey T: 54, monkey B: 64). Data were gathered in 62 recording sessions (monkey T: 28, monkey B: 34). Based on manual mapping, we found 57 pairs with overlapping pRFs (monkey T: 26, monkey B: 31).

### **Attention-dependent modulation of spiking activity**

We first verified whether ESA-responses in our paradigm revealed a similar pattern of attentional modulation as described in previous studies based on single-unit firing rates<sup>54,90,91,113,115,186,230,231</sup>. These studies showed consistently that when two stimuli are present in a RF, firing rates were modulated by attention to similar levels as for the attended stimulus presented alone. Without attention, firing rates were intermediate. Figure 12 A shows an example for ESA-responses under different attentional conditions with either one ( $S^+/S^-$ ) or two ( $D^+/D^-$ ) stimuli inside the same pRF (cf. 3.1.3, Methods for details of labeling task conditions). Due to our study design, ESA-responses were stronger during  $S^+$  conditions than during  $S^-$  conditions. When both stimuli were present in the pRF, the ESA-responses were in-between those for the single stimulus conditions and depended on the allocation of spatial attention. ESA-responses were stronger when the well activating stimulus was attended ( $D^+$ ) than when the less activating stimulus was attended ( $D^-$ ). Quantitative analysis of 80 recording sites (monkey T: 37, monkey B: 43) revealed significant differences between the two conditions with both stimuli present in the pRF (Fig. 12B). ESA-responses were significantly larger during  $D^+$  (median 1.3) than during  $D^-$  conditions (median: 0.8;  $z = 7.293$ , Bonferroni-corrected  $p < 10^{-11}$ , Wilcoxon signed-rank test). Thus, ESA-responses during double conditions were shifted towards the response levels induced when the attended stimulus was presented in isolation ( $S^+$ : median: 1.3;  $S^-$ : median: 0.6). Conditions which required the animals to direct attention away from the two stimuli inside the pRF to one of the stimuli located in the opposite hemi-field resulted in intermediate responses ( $D^0$ : median 0.9). These responses were significantly different from the responses for the two other conditions with two stimuli in the pRF ( $D^+/D^0$ :  $z = 7.77$ ,  $p < 10^{-10}$ ;  $D^-/D^0$ :  $z = -3.0504$ ,  $p = 0.0069$ ;  $p$  - values are Bonferroni corrected, Wilcoxon signed-rank test).

To quantify the extent of attentional modulation of responses in the double conditions and relate

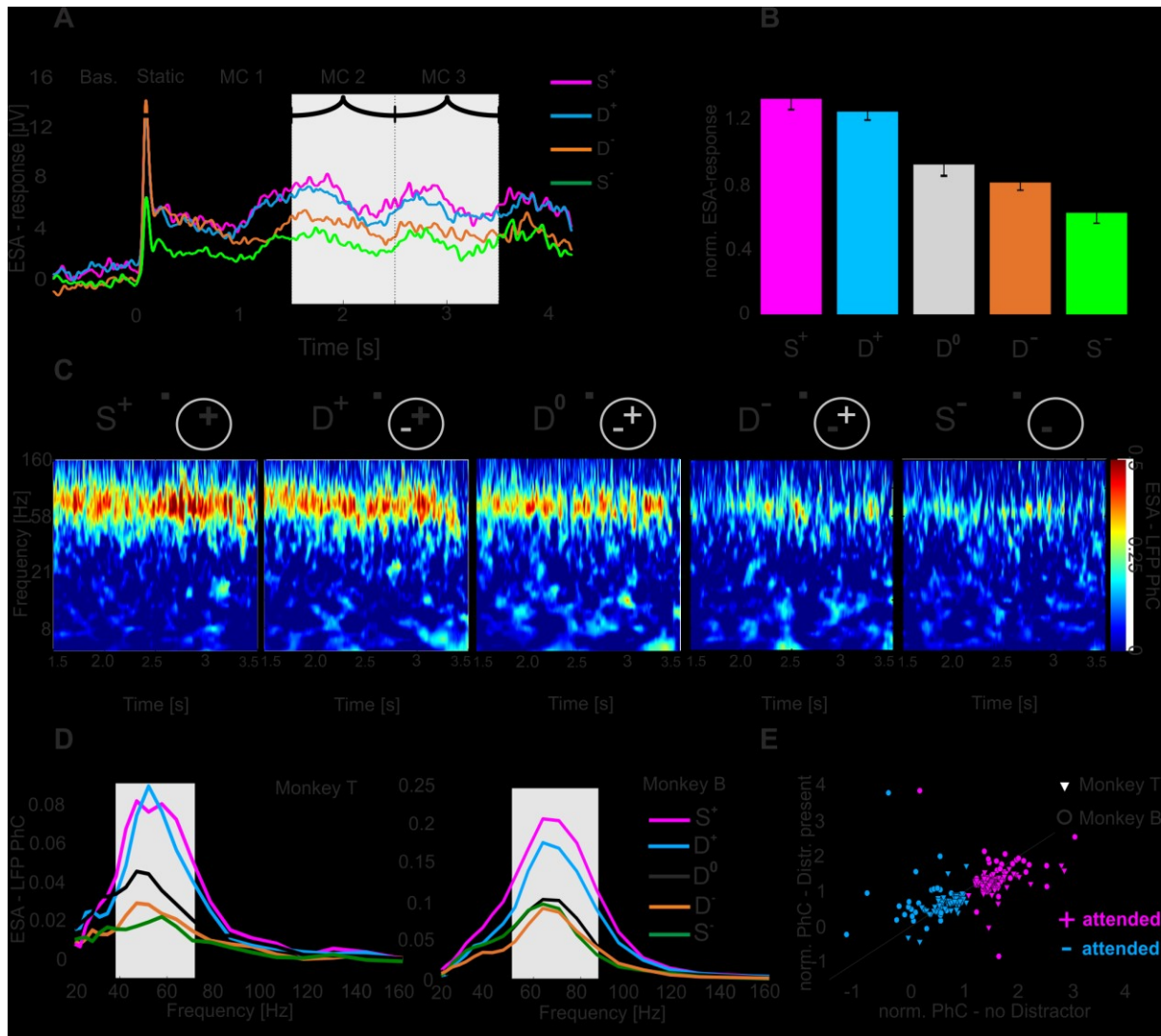


**Figure 12:** Attention-dependent modulation of neuronal responses and their coupling to the local population activity. **A**, Time course of mean ESA-responses during the shape-tracking task of an example case (visual stimulation sequence indicated above as in Fig. 9). For clarity, the  $D^0$ -condition is omitted. **B**, Histogram of normalized median ESA-responses during MC 2 and 3 (highlighted gray in A) and pooled over both animals. Error-bars indicate 95 % confidence intervals. **C**, Time-frequency plots of the PhC between ESA and LFP for all task conditions during MC 2 and 3 of an example case. Pictograms indicate stimulus configuration within the V4 pRF. Plus and minus signs depict the stimuli inducing stronger and weaker  $\gamma$ -PhC, respectively. Bold highlighted signs correspond to the attended stimulus. **D**, Median spectra for ESA-LFP PhC of both animals. The individual  $\gamma$ -bands are highlighted in gray. **E**, Scatter-plot of normalized ESA-LFP PhC (median over MC 2/3 and the individual  $\gamma$ -band) for conditions without vs. with distractor in pRF.

it to the difference between the responses caused by each of the two different stimuli alone we used an attentional modulation index (AMI). It is computed as the ratio of the attention-dependent difference between responses obtained in the  $D^+$  and  $D^-$  condition to the difference between responses in the  $S^+$  and  $S^-$  condition ( $AMI = ((D^+ - D^-) / (S^+ - S^-)) * 100$ ). The AMI reaches 100 %, if attention modulated ESA-values such that the differences between double conditions on the one side and single conditions on the other side are equal. An AMI of zero

indicates that there is no effect of attention when both stimuli are present. AMI values larger than 100 % indicate that the difference of responses between  $D^+$  and  $D^-$  is even larger than between the single conditions. Negative values correspond to an opposite modulation in the double conditions as compared to the single conditions ( $D^+$  smaller than  $D^-$ ). For ESA-responses the median AMI value of 68.4 % shows that the difference between  $D^+$  and  $D^-$  conditions is similar to that observed during the respective single conditions, but does not reach the same size. In summary, the attention-dependent modulation of ESA-responses under the stimulus and task conditions of the present experiments is well in line with previous findings on single-unit firing rates in areas V4 and MT.

### **Attention-dependent changes of $\gamma$ -PhC between neurons and overall population activity**

After having confirmed the expected effect of selective attention on response strength, we tested our hypothesis that effective processing of an attended stimulus is associated with a specific configuration of functional connectivity within the local neuronal network. To this end, we compared the strength of  $\gamma$ -band synchronization between a small group of neurons (ESA) and the overall population activity (as measured by the LFP) either for a particular stimulus presented alone or together with a distractor in the pRF.

We calculated the PhC between ESA and LFP taken from two separate, closely spaced electrodes. In the following ESA-LFP PhC analysis, the designation of stimuli as “+” or “-“ depended on the strength of  $\gamma$ -PhC induced by the two stimuli when presented alone. Figure 12 C provides an example case of monkey B, showing the phase coupling between ESA and LFP in the  $\gamma$ -band (57.7 Hz to 86.8 Hz), persisting throughout MCs 2 and 3. The time averaged strength of the  $\gamma$ -PhC for the two conditions with only one stimulus in the pRF was 0.34 for the  $S^+$  and 0.13 for the  $S^-$  condition, indicating two configuration states that are separable with our network interaction proxy. When both stimuli were simultaneously present in the pRF and one of them was attended, the degree of synchronization closely matched the values of the corresponding single stimulus condition ( $D^+$ : mean 0.3;  $D^-$ : mean 0.15). With attention directed outside the pRF, the  $\gamma$ -PhC was intermediate ( $D^0$ : mean 0.26).

Mean PhC-spectra for all recording site pairs confirmed the similarity of  $\gamma$ -PhC between conditions requiring to attend the same stimulus either in the presence or in absence of a distractor inside the pRF, for both animals (Fig. 12D). A stimulus inducing low  $\gamma$ -PhC values when presented alone ( $S^-$ ) induced similarly low  $\gamma$ -PhC values even in the presence of a

distractor inducing high  $\gamma$ -PhC when presented alone ( $D^-$ ). Conversely, when the stimulus inducing strong  $\gamma$ -PhC was attended, the level of  $\gamma$ -PhC stayed similarly high when a distractor inducing weak  $\gamma$ -PhC was present in the pRF (compare  $S^+$  and  $D^+$ ). The attention-dependent modulation of  $\gamma$ -PhC for all ESA-LFP pairs is shown in Figure 12 E. The scattering of entries around the diagonal line indicates the similarity between the normalized  $\gamma$ -PhC values for attending a stimulus without versus with distractor in the pRF for both animals ( $n = 90$ ). Note, that each recording site pair may deliver two ESA-LFP pairs since each electrode contributed an ESA and a LFP signal. The differences between normalized  $\gamma$ -PhC-values for the two conditions requiring to attend the stimulus inducing strong  $\gamma$ -PhC were small but significant ( $S^+$ : median 1.42,  $D^+$ : median 1.27,  $z = 4.6296$ , Bonferroni corrected  $p < 10^{-4}$ , Wilcoxon signed-rank test). For conditions requiring to attend the stimulus inducing weak  $\gamma$ -PhC, the difference was not significant ( $S^-$ : median 0.68,  $D^-$ : median 0.63;  $z = 1.3017$ ,  $p = 0.1930$ ). In contrast, the difference between double conditions was large and highly significant ( $D^+$ : median 1.27,  $D^-$ : median: 0.63,  $z = 7.1481$ , Bonferroni corrected  $p < 10^{-11}$ , Wilcoxon signed-rank test). The AMI, as a measure for the degree of attentional modulation in the double conditions as compared to the single conditions reached a median value of 81.8 % and was significantly larger than the AMI for ESA-responses (ESA-responses: 68.4 %,  $p = 0.0142$ ,  $z = -2.4523$ , Wilcoxon rank-sum test). This close match of  $\gamma$ -PhC between ESA and LFP signals for conditions requiring to attend the same stimulus ( $S^+/D^+$  and  $S^-/D^-$ ) also holds true for the individual animals (see Table 1). We found these significant modulations of PhC only in the  $\gamma$ -frequency range, but not for other frequency bands.

**Table 1:** Comparison of ESA-LFP  $\gamma$ -PhC values observed during different stimulus conditions for both animals.

Compared Conditions	Monkey T (n = 34)		Monkey B (n = 56)	
	$S^+/D^+$	1.48/1.54	$p = 0.4675$ , $z = 0.7266$	1.41/1.18
$D^+/D^-$	1.54/0.55	$p < 10^{-3}$ *, $z = 4.0433$	1.18/0.63	$p < 10^{-8}$ *, $z = 5.9791$
$D^-/S^-$	0.55/0.51	$P = 0.1909$ , $z = 1.3079$	0.63/0.78	$p = 0.0027$ *, $z = 3.3199$

*The leftmost column describes the two task conditions that are compared. For each animal, the left column shows the normalized median  $\gamma$ -PhC values for these two conditions, whereas the right column provides the results of the corresponding Wilcoxon signed-rank tests. The asterisk indicates Bonferroni-corrected p-values. ESA-LFP  $\gamma$ -PhC values during ST-task for individual animals.*

To ensure that the stimulus specific differences of  $\gamma$ -PhC do not reflect very weak or lacking

ESA and LFP oscillations, we examined the strength of underlying  $\gamma$ -oscillations. Figure 15A and B (3.2 Supplements) show that not only during  $S^+$  and  $D^+$  conditions, but also during  $S^-$  and  $D^-$  conditions,  $\gamma$ -band oscillations were sufficiently large to ensure meaningful phase estimations for the PhC-measure. To investigate whether the modulations of  $\gamma$ -PhC simply reflect the modulations in ESA and/or LFP  $\gamma$ -power, we analyzed how well the reduction of  $\gamma$ -PhC between  $D^+$  and  $D^-$  conditions can be explained by changes in ESA and LFP  $\gamma$ -power (Figure 15 C/D). There were no significant correlations between the  $\gamma$ -PhC reduction and modulations of LFP or ESA  $\gamma$ -power ( $\gamma$ -PhC/  $\gamma$ -LFP-power: Pearson's correlation,  $r = 0.1821$ ,  $p = 0.11$ ;  $\gamma$ -PhC/  $\gamma$ -ESA-power:  $r = 0.17$ ,  $p = 0.1252$ ).

### **Attention-dependent modulation of functional coupling between groups of neurons**

Processing of different stimuli in a local network is thought to depend on different patterns of functional coupling strengths between its neurons. Therefore, we investigated whether the strength of functional connections between two small groups of neurons as measured by the ESA-ESA  $\gamma$ -PhC in the presence of two stimuli matched that observed for the attended stimulus presented alone. Here the designation of stimulus conditions as  $S^+$  or  $S^-$  was based on the strength of the ESA-ESA  $\gamma$ -PhC induced by the two different stimuli shown in these conditions. Contrary to our expectation, we found that the difference between double conditions ( $D^+/D^-$ ) was much smaller than between single conditions ( $S^+/S^-$ ) as reflected by a median AMI of 57.9 % ( $n = 44$ ). This raises the question whether this rather low AMI is characteristic for the  $\gamma$ -PhC between two subpopulations of neurons of the same population. The distribution of AMI values (Fig. 13A) indicates that this is not the case since the AMI differed strongly over a wide range between pairs.

To investigate whether the wide range of AMI-values might be related to different response characteristics of the two constituting sites, we split the pairs according to their AMI value into three equally sized groups. (Fig. 13A, dashed lines separate low, medium and high AMI group). First, we analyzed the relation between the pairs' AMI values for  $\gamma$ -PhC and the ESA-responses of their corresponding sites during  $S^+$  conditions. Almost half (47 %) of the pairs of the low AMI-group (Fig. 13B, red dots) had at least one site, which responded very weakly (ESA response strength  $< 0.05$ , border indicated by gray dashed lines in Fig. 13B) to the stimulus inducing high  $\gamma$ -PhC. There were no such sites for the high AMI-group (blue dots) and only two pairs with such low responses for the medium group (green dots). Chi-square tests of

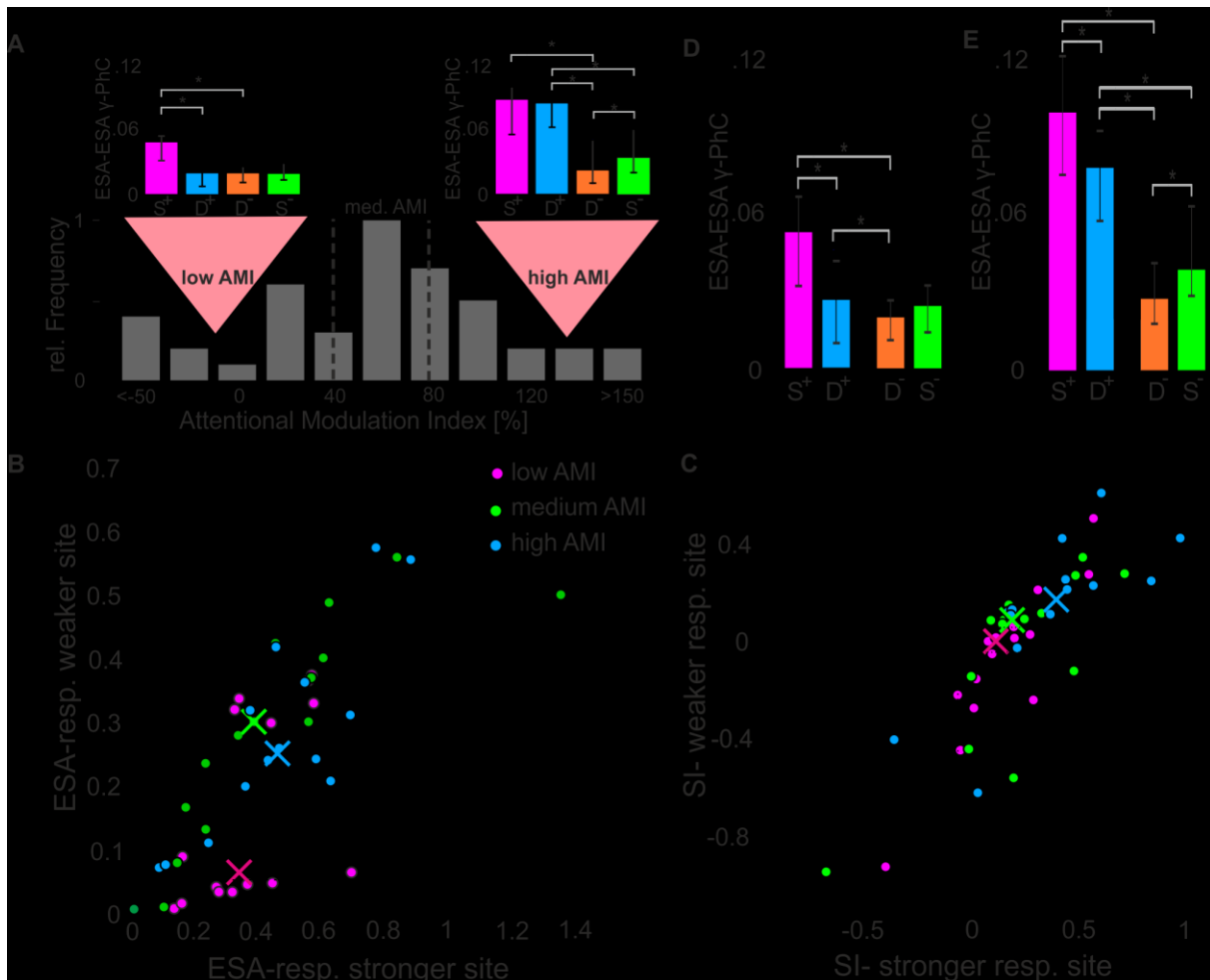


**Figure 13:** Dependence of ESA-ESA  $\gamma$ -PhC modulation on level of ESA-responses and stimulus specificity. **A**, Distribution of AMI-values based on ESA-ESA  $\gamma$ -PhC ( $n = 44$ ). The dashed vertical lines indicate borders between the third with lowest, the third with medium, and the third with highest AMI-values. The bar-plot insets above the distribution depict for the low and the high AMI group the median normalized  $\gamma$ -PhC between ESA-signals, which determine the AMI values. **B**, Scatter-plot of normalized ESA-responses for the stimulus inducing higher  $\gamma$ -PhC between ESA-signals ( $S^+$  condition). An entry represents the ESA-responses of both recording sites contributing to the  $\gamma$ -PhC, with the site showing higher ESA-responses plotted on the X-axis. The different colors represent the high, medium and low AMI-group, as illustrated in A. The median values for each group are depicted as correspondingly colored crosses. **C**, Same as in B, but for the stimulus specificity of the sites constituting a pair. Sites showing higher SI-values are plotted on the X-axis. **D**, Histogram of median normalized  $\gamma$ -PhC between ESA signals of the unspecific group (at least one site with ESA-responses below 0.05, see B or SI-values between -0.05 and 0.05 or with opposite stimulus preference, see C, cases between dashed lines and in lower right quadrant). The error-bars indicate 95% confidence intervals. Asterisks indicate significant differences ( $p < 0.05$ ) **E**, same as in D, but for the specific group (pairs which were not classified as unspecific, see D).

independence confirmed, that there are more such pairs in the low AMI group than in the high AMI-group ( $\chi^2$  (1,  $N = 29$ ) = 8.61, Bonferroni-corrected  $p < 0.01$ ). All other comparisons between groups revealed no significant differences after Bonferroni correction (low AMI/medium AMI; medium AMI/high AMI;  $\chi^2$  (1,  $N = 30$ ) < 3.8, Bonferroni-corrected  $p > 0.05$ ). Yet, the low-AMI group seems to consist of two groups of pairs, one with at least one

site showing rather low responses ( $< 0.05$ ) and another one where both sites showed normal response levels (values around 0.3 to 0.6). This may indicate that there are further combinations of response properties of a pair that go along with low AMI values.

Therefore, we analyzed whether the ratio between ESA-responses to the two stimuli might influence the AMI-values of  $\gamma$ -PhC as well. For each recording site a specificity index (SI) was calculated, which describes the degree of similarity (or dissimilarity) of the responses for the two different stimuli. The index reflects the difference between the ESA-responses during the  $S^+$  and the  $S^-$  conditions divided by their sum ( $(S^+ - S^-)/(S^+ + S^-)$ ). Positive values indicate a preference for the stimulus of the  $S^+$  condition, negative values for the stimulus of the  $S^-$  condition and zero the same response strength for both stimuli. The scatterplot in Figure 13 C depicts the SI-indices of the two contributing sites for each recording site pair of the three different AMI groups (high, medium and low values). A pair that has at least one site, which responds very similar to both stimuli, would be located between the dashed gray lines (Fig. 13C; SI-values between -0.05 and 0.05). The entry of a pair with opposite stimulus preferences would be located in the lower right quadrant of the scatterplot (because the site with the higher SI-value is plotted on the X-axis). When comparing the distributions of entries it becomes obvious, that more entries of the low AMI group (red dots) are located between the gray dashed lines than for both other groups. Furthermore, there are no entries of the high AMI-group with opposite stimulus preference. Chi-square tests confirmed that the low AMI-group contained in comparison to the medium and the high AMI-group more pairs where at least one site shows almost no difference in responses to both stimuli (SI-values between  $- 0.05$  and  $0.05$ ) or even opposite stimulus preferences (high/low group:  $\chi^2(1, N = 29) = 10.208$ , Bonferroni-corrected  $p < 0.005$ ; medium/low group:  $\chi^2(1, N = 30) = 6.53$ , Bonferroni-corrected  $p < 0.04$ ). The corresponding differences between high and medium AMI group were not significant ( $\chi^2(1, N = 29) = 0.68$ ,  $p = 0.41$ ).

In summary, we found that high AMI-values correlate with a sufficient level of responses of both sites to the attended stimulus (Fig. 13B). Furthermore, high AMI-values also correlate with higher levels of stimulus specificity for the same stimulus of the two constituting sites (Fig. 13C). Thus, the weak synchronization in the  $D^+$  condition (Fig. 11A, compare insets), which results in low AMI values, is observed in pairs with at least one site almost not responding to the attended stimulus (Fig. 13B) or responding equally strong to both stimuli (Fig. 13C). Such sites may therefore receive comparatively high proportions of signals related to the non-attended stimulus during the  $D^+$  condition. Strong synchronization between those neurons with a group of neurons processing mainly the attended stimulus could lead to a mixing of signals

from target and distracter stimuli, which would counteract the enhanced and selective processing of the attended stimulus. It might therefore be beneficial that attention does not include those neurons into the ensemble processing the attended stimulus by enhancing their functional coupling.

In order to test whether such relations of response characteristics determine the different effects of attention  $\gamma$ -PhC, we split the 44 ESA-ESA pairs into two groups: One in which the promotion of distractor-related signals is unlikely and a second where this is more likely. Pairs were assigned to the first group (specific group) if both sites showed a sufficient response of at least 0.05 in the  $S^+$  condition and a preference for the same stimulus (both SI-values above +0.05 or both below -0.05). The remaining pairs were assigned to the second group (unspecific group). The median  $\gamma$ -PhC values of the unspecific group ( $n = 24$ ) are shown in Figure 13 D, the corresponding  $\gamma$ -PhC values for the specific group ( $n = 20$ ) in Figure 13 E. The most evident difference between both groups is between the median  $\gamma$ -PhC values during  $D^+$ -conditions. The unspecific group (Fig. 13D) reached with a median value of 0.026 only 49.1 % of the  $\gamma$ -PhC evoked during  $S^+$ -conditions (median 0.053). For the specific group (Fig. 13E), the  $\gamma$ -PhC during  $D^+$ -conditions (median 0.08) reaches 80.4 % of the value evoked by the  $S^+$ -condition (median: 0.1). However, for both groups these differences were significant (unspecific group:  $p < 10^{-3}$ ,  $z = 3.9429$ ; specific group:  $p = 0.0015$ ,  $z = 3.6213$ , Wilcoxon signed-rank test, all p-values are Bonferroni corrected).

Another difference between specific (Fig. 13E) and unspecific (Fig. 13D) group can be observed when comparing  $D^+$  and  $D^-$  conditions. For the specific group, the difference was large and significant ( $D^+$ : median 0.08,  $D^-$ : median 0.027, Bonferroni corrected  $p < 10^{-3}$ ,  $z = 3.8826$ ), whereas it was small, albeit significant for the unspecific group ( $D^+$ : median 0.026,  $D^-$ : median 0.021, Bonferroni corrected  $p = 0.036$ ,  $z = 2.6857$ , both Wilcoxon signed-rank test). The  $\gamma$ -PhC of the unspecific group recorded during  $D^+$  conditions (median: 0.026) was not even significantly different from those recorded during  $S^-$  conditions (median 0.028;  $p = 0.3758$ ,  $z = 0.8857$ , Wilcoxon signed-rank test). Yet, the same conditions evoked highly significant differences for pairs of the specific group ( $D^+$ : median 0.08,  $S^-$ : median 0.03; Bonferroni corrected  $p < 10^{-3}$ ,  $z = 3.8453$ , Wilcoxon signed-rank test). These differences in  $\gamma$ -PhC during double conditions explain the large and significant differences in AMI-values between both groups, with a median AMI of 84.7 % for the specific group and only 29.9 % for the unspecific group ( $p < 10^{-5}$ ,  $z = 4.0423$ , Wilcoxon signed-rank test). The AMI for the unspecific group was significantly lower than AMI-values for ESA-responses and ESA-LFP  $\gamma$ -PhC (ESA-

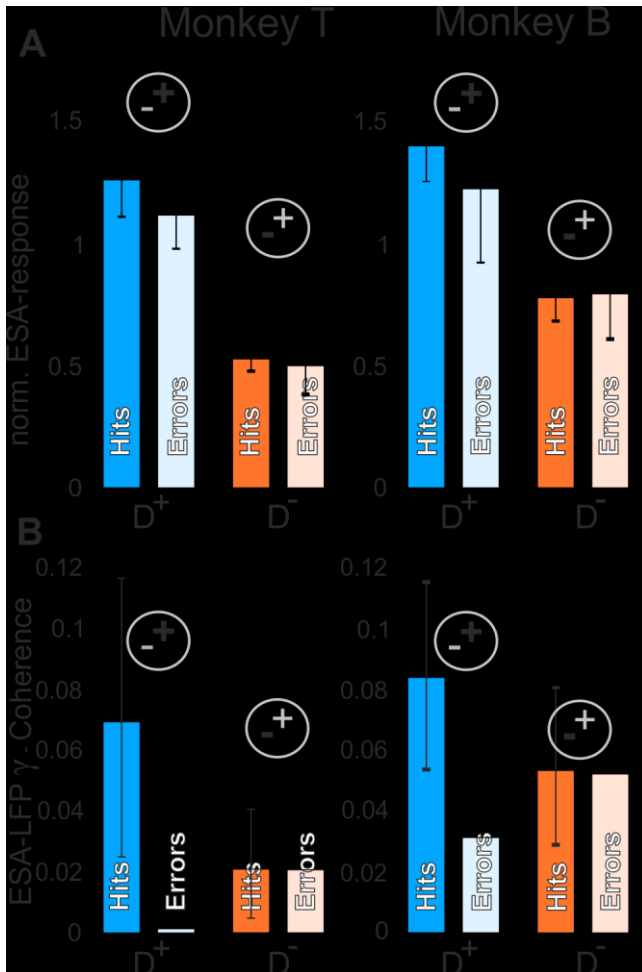


**Figure 14:** Neuronal correlates of different behavioral outcomes. **A**, Median normalized ESA responses just before correct (dark blue and orange) and erroneous (light blue and orange bars) responses in trials requiring attention for one of the two stimuli within the pRF. Error-bars indicate 95% confidence intervals. **B**,  $\gamma$ -coherence between ESA and LFP for the same conditions as in A. Note, that in contrast to A error-bars here indicate 95 % of coherence values generated from 1000 times compiling sets of correctly performed trials (c.f. Materials and Methods). The coherence value for error trials represents the coherence of all error trials pooled (due to small number). The value has to be interpreted with respect to the distribution of correctly performed trials and has no error-bars, since it is only one value.. For abbreviations and pictograms see Figures 11 and 12.

responses/unspecific group:  $p < 10^{-4}$ ,  $z = -4.1392$ ; unspecific group/ESA-LFP AMI:  $p < 10^{-10}$ ,  $z = -6.4883$ , p-values were Bonferroni-corrected). AMI-values for the specific group were significantly larger than those of ESA-responses and ESA-LFP  $\gamma$ -PhC (ESA-responses/specific group:  $p = 0.032$ ,  $z = 2.4085$ ; specific group/ESA-LFP AMI:  $p < 10^{-8}$ ,  $z = 5.9558$ , p-values were Bonferroni-corrected).

In summary, the attention-dependent modulation of  $\gamma$ -PhC between two neuronal sub-populations of the same local network depends on the response characteristics of their neurons for the two stimuli located in the pRF. The modulation is almost identical in conditions with and without distractor if both sub-populations respond sufficiently well to an attended stimulus and share the same stimulus preference. In contrast, if one of the two sub-populations shows only low responses to one of the stimuli, or the sites do not share the same stimulus preference, the strong attention-dependent difference between double conditions vanished.

### Network state and behavioral outcome

The results so far showed that attention modulates the pattern of  $\gamma$ -PhC in

dependence of the attended stimulus with very similar values of  $\gamma$ -PhC in conditions with and without nearby distractor present. Hence, successful stimulus processing seems to depend on this specific pattern of synchronization within the local V4 network. If this holds true, the

question arises, whether unsuccessful behavioral outcomes are associated with an incorrect pattern of  $\gamma$ -synchronization. Thus, we compared the  $\gamma$ -synchronization and spiking activity of periods directly preceding a behavioral error. A sufficient number of errors occurring during MC 2/3 for  $D^+$  and  $D^-$  conditions were available only for false alarms for both animals. Therefore we here show the false alarm trials pooled across all recording sessions for each animal individually. A comparison of misses and correctly executed trials for the monkey with a sufficient number of misses is shown in Figure 16 (chapter 3.2.1). The pooling across sessions made it necessary to investigate  $\gamma$ -band synchronization between ESA and LFP signals based on magnitude-squared coherence (cf. 3.1.3 Materials and Methods for details). We analyzed  $\gamma$ -synchronization and ESA-responses within a time period of 400 ms for monkey T and 500 ms for monkey B. (Materials and Methods) terminating 200 ms before the behavioral response.

The normalized ESA-responses were similar between periods preceding false alarms (Fig. 14A, light blue and orange bars) and correct responses (Fig. 14A, dark blue and orange bars) when attending the stimulus inducing stronger responses ( $D^+$ ) as well as for attending the stimulus inducing weaker responses ( $D^-$ ). There was no significant difference during  $D^+$  conditions for monkey T, and only small but significant differences for monkey B (monkey T: hits: 1.26, errors: 1.12,  $n=52$ ,  $z$ -score = -1.20;  $p = 0.12$ ; monkey B: hits: 1.40, errors: 1.23,  $n=39$ ,  $z$ -score = -2.22,  $p = 0.013$ ;  $z$ -transform, cf. 3.1.3 Materials and Methods). Similarly, the differences between ESA-responses in false alarm and correctly executed trials during  $D^-$  were not significant for both animals (monkey T: hits: 0.53, errors: 0.50,  $n=108$ ,  $z$ -score = -0.57; monkey B: hits: 0.78 errors: 0.80,  $n=58$ ,  $z$ -score = 0.26;  $p>0.05$  for both,  $z$ -transform).

In contrast to ESA-responses, the  $\gamma$ -synchronization between ESA and LFP (Fig. 14B) showed a strong reduction for false alarm trials. During  $D^+$  conditions, the  $\gamma$ -synchronization was more than 98 % weaker for monkey T and still 62 % weaker for monkey B in periods preceding a behavioral error as compared to correctly performed trials (monkey T: hits: 0.07, errors: 0.001,  $n=28$ ,  $z$ -value = -2.5083; monkey B: hits: 0.08, errors: 0.03,  $n = 38$ ,  $z$ -value = -2.7822;  $p < 0.005$  for both). During  $D^-$  conditions, the values between false alarm trials and correctly performed trials did not differ significantly (monkey T: hits: 0.02, errors: 0.02,  $n = 95$ ,  $z$ -value = -0.0978,  $p=0.46$ ; monkey B: hits: 0.053, errors: 0.052,  $n = 38$ ,  $z$ -value = -0.1123,  $p= 0.46$ ). In summary, false alarms seem to correlate with a reduced level of  $\gamma$ -synchronization within the local neuronal network as compared to periods preceding correctly executed trials. In contrast, spiking activity does not reflect the erroneous behavioral responses, indicating the relevance of correctly configured networks for successful behavior.

### 3.1.5 Discussion

Within the frame of this work, we examined whether the ability of neuronal networks to perform different functions on the same input could be implemented by an attention-dependent reconfiguration of the local neuronal networks. We hypothesized that this reconfiguration within the local neuronal networks is established by changing the pattern of functional connections between the network's neurons by adjusting the strength of their  $\gamma$ -synchronization. Thus, for effective processing of an attended stimulus, a stimulus-specific pattern of  $\gamma$ -synchronization would be necessary and patterns deviating from this specific configuration would result in a decreased stimulus processing.

Indeed, our results show that in the presence of two stimuli in the pRF, the  $\gamma$ -PhC between the spiking activity and the overall population activity within a local network depends on the attended stimulus and is highly similar to the values observed when the attended stimulus was presented alone in the pRF. The same holds true for  $\gamma$ -PhC of spiking activity between two groups of neurons of the same local network, but only when both responded sufficiently well to this stimulus and both shared the same stimulus preference. Correspondingly, the attentional modulation index (AMI) for ESA-LFP  $\gamma$ -PhC and ESA-ESA  $\gamma$ -PhC reached 82 % and 85 %. Similarly, ESA-responses were modulated during double conditions in the direction of levels observed for the attended stimulus presented alone, but to a lesser extent as indicated by the smaller AMI of 68%. Contrary to these qualitatively similar dependencies of  $\gamma$ -PhC and ESA-responses on the attended stimulus, both measures behaved qualitatively different prior to behavioral errors. ESA-responses in periods preceding false alarms were very similar to the responses observed prior to correctly terminated trials. In contrast, high levels of ESA-LFP  $\gamma$ -synchronization were strongly reduced in error trials. Furthermore, the  $\gamma$ -PhC between the ESAs of two groups of neurons where at least one site responded poorly to the attended stimulus, or very similar for both stimuli, strongly reduced when a distractor was added. A similar pattern was observed for the comparison of misses and correctly executed trials shown for the monkey with a sufficient number of misses (Fig. 16). These observations suggest that attention configures the pattern of functional coupling between the networks neurons specifically for effective processing of the relevant stimulus. Furthermore, our findings point to a top-down mechanism, which works in parallel to mechanisms gating relevant information to downstream areas and configures the synchronization within local network.

The results of attention-dependent modulations of spiking activity are well in line with previous

work. Our task paradigm evoked different spiking activity for the two stimuli based on differences in location instead of orientation or motion direction as in previous studies. Furthermore, the stimuli were attended in conditions with and without distractor. Nevertheless the observed ESA-responses showed an attention-dependent modulation which was very similar to previous results<sup>54,90,91,113,115,231</sup>. Furthermore, a dependence of local synchronization on different stimulus configurations has been observed for anaesthetized cats<sup>142,161,232</sup> and for monkey under passive viewing conditions<sup>221,233,234</sup>. The latter results support the notion that processing of specific stimuli is associated with a specific pattern of synchronization within a local neuronal network, which is thought to reflect the functional coupling within this network. However, we were interested in whether attention invokes stimulus-specific network configurations depending on the momentary behavioral demand, even though the stimulus input does not change. These attention-dependent changes would allow for an extensive number of different network configurations within the framework of the given anatomical connections by selectively modulating the strength of functional coupling between the network's neurons<sup>107,116,149,177,210,235,236</sup>. If such a specific pattern of  $\gamma$ -synchronization within a local network is crucial for its ability to process a specific, behaviorally relevant stimulus, the pattern should change as attention switches between stimuli. Furthermore, it should be very similar to the pattern observed in the absence of the distractor stimulus. Our results confirm this prediction. When instead of a single stimulus two closely spaced stimuli provided input signals to a local neuronal network in V4, the  $\gamma$ -PhC depended on which stimulus was attended and was very similar to the values observed when this stimulus was presented alone. The AMI of 85 % for the  $\gamma$ -PhC between ESA of two groups of neurons of the same local network illustrates the high precision by which selective attention adjusts the functional coupling strengths when the same stimulus is attended. The significantly weaker AMI for the ESA-responses support the notion that response strength and  $\gamma$ -PhC are not trivial consequences of each other, but reflect different aspects of neural processing<sup>105,176</sup>.

The hypothesis of attention-dependent dynamic network configuration by  $\gamma$ -band synchronization is further supported by pairs, which do not preserve their high  $\gamma$ -PhC for an attended stimulus when a distractor stimulus is added. Of those pairs, at least one site responds either very weakly to the attended stimulus or relatively strong to the distractor stimulus. These neurons are likely to receive a comparably high proportion of input signals representing the distractor, since even an attention-dependent, input gating mechanism suppresses distractor related signals only to a limited extent. The reduced strength of functional coupling between those neurons and neurons of the dynamically defined network processing the attended stimulus

should therefore help to avoid interference of distractor signals with processing of the attended stimulus. If in contrast only one stimulus is present, even weakly driven neurons can contribute to a network processing this stimulus since they carry no signals of distractors that could interfere. Well in line Vinck et. al. (2013)<sup>237</sup> gave evidence for a decoupling of those neurons from the processing network, which provided only poor information about an attended stimulus, even though no nearby distractor was present.

The relevance of  $\gamma$ -synchronization for the functional configuration of the local neuronal network in V4 is further supported by the characteristics of neuronal activity directly preceding behavioral errors. While the attention-dependent modulation of ESA-responses were almost unchanged in comparison to correctly executed trials, strong  $\gamma$ -synchronization between groups of neurons and the local population activity (LFP) in correctly executed trials vanished before an error. Several other studies also reported correlations between behavioral performance and oscillatory power or synchronization as well as firing-rates. In contrast to our study, they either used a task with only one stimulus in the RF to investigate error-dependent differences of synchronization<sup>238</sup>, or compared conditions with attention directed into the RF versus away from the RF<sup>104,239</sup>. The latter two studies report that firing rates and synchronization show qualitatively similar differences when comparing either slow and fast reaction times<sup>104</sup> or error-dependent changes<sup>239</sup>. The level of synchronization and the firing rates were higher during fast trials as compared to slow trials and during correctly executed trials when compared to erroneously terminated trials. However, for our specific behavioral paradigm, recording constellation, and the attentional conditions compared here (attention directed always to a stimulus within the pRF of the recorded V4 population), we observed qualitatively different results for firing rates and  $\gamma$ -synchronization.

To put these results into perspective, we briefly recapitulate the selective gating of relevant information between and within visual areas. Previous work showed that V4 neurons synchronize selectively with afferent V1 neurons representing the attended stimulus while desynchronizing with those representing distractors<sup>183,184</sup>. Furthermore, we showed that mainly signals carrying specific signatures related to the attended stimulus enter into the local processing network in V4.<sup>118</sup> These findings, together with theoretical investigations, point towards an attention-dependent routing mechanism based on highly selective changes of functional coupling between V4 neurons and different subsets of their afferent inputs<sup>179,182,208,209,236,240</sup>. The almost unchanged level of firing rates during error and correctly performed trials in both task conditions, as shown in Figure 14 A, indicate that attention was correctly directed to the target stimulus: If monkeys had attended the nearby distractor in the

same pRF, the firing rates should have approached the strength associated with the distractor. A similar consideration holds if the animals would have allocated attention elsewhere. In this case, one would expect an intermediate firing rate, as observed for trials with attention directed away from the pRF ( $D^0$ -condition, Fig. 12B). Our findings therefore indicate that those attention-dependent top-down mechanisms that selectively route the signals of the attended stimulus from upstream areas to the V4 neurons, were unlikely the source of the error.

The degradation of local  $\gamma$ -synchronization preceding errors rather indicates that successful processing of an attended stimulus also depends on a specific synchronization in the supragranular layers of V4. The recorded neurons in the upper layers of V4 show the expected level of spiking activity and are therefore likely to receive the correctly selected signals from the granular layer of V4. Thus, their local  $\gamma$ -synchronization is unlikely to depend solely on successful gating of the afferent stimulus related signals to V4. Rather, it is subject to attention-dependent top-down mechanisms, independent of a gating mechanism for the afferent bottom-up input to V4. In line with our findings, Vinck and Bosman (2016)<sup>241</sup> concluded in a recent review based on experimental data, that  $\gamma$ -oscillations in superficial and in granular layers can be generated fairly independent of each other. Thus, our observed strong degradation of  $\gamma$ -synchronization within the local network in superficial layers during error trials, might arise from a failure of attention-dependent top-down mechanisms to synchronize the neuronal network in layer 2/3. At the same time, attentional mechanisms are still successful in selective gating of relevant information to layer 4 neurons. However, since neurons located in supragranular layers provide the cortico-cortical output projections, the disappearance of their strong  $\gamma$ -synchronization results in a reduced impact of their spikes on down-stream neurons<sup>110</sup>. Thus, the signal-to-noise ratio of the behaviorally relevant signal, and therefore its processing further downstream, is expected to be compromised. This may well give rise to erroneous responses<sup>103,104,242</sup> and might explain the different correlations between local  $\gamma$ -synchronization and firing-rates with behavioral outcome.

### 3.1.6 Conclusion

In summary, our results show clear similarities as well as specific differences between the attention-dependent modulation of  $\gamma$ -synchronization and spiking activity in local neuronal networks of area V4. These results are well in line with the expectations for an attention-dependent mechanism that structures functional coupling strengths and hence the functional

configuration of a local network by modulating  $\gamma$ -band synchronization. We conclude that: (1) Attention adjusts the pattern of functional coupling strengths within a local neuronal network specifically for processing of an attended stimulus. (2) Attention dynamically decouples neurons from a network processing the attended stimulus when they would compromise processing with additional distractor related signals. (3) Degraded synchronization within the local network occurs just before behavioral errors in spite of almost intact attention-dependent firing-rates, indicating an error-location beyond afferent signal gating.

### **3.1.7 Author Contributions**

AK, SM, and IG designed the experiment. ED and MH performed the experiment and analysis. ED and AK wrote the manuscript. SM, MH, and IG discussed and reviewed the manuscript.

### **3.1.8 Funding**

The Bernstein Group for Computational Neuroscience Bremen (Grant 01GQ0705) and the German Research Foundation (Grant KR 1844/4-1) have supported this work. Furthermore, ED was supported by the Fazit-Stiftung and IG was supported by the Leibniz Graduate School for Primate Neurobiology.

### **3.1.9 Acknowledgments**

We like to thank Aleksandra Nadolski for the support and valuable help with animal training and experiments, as well as Katrin Thoß and Ramazani Hakizimana for animal care. We also thank Dr. Detlef Wegener and Bastian Schledde for helpful comments on the manuscript.

### 3.2 Supplements

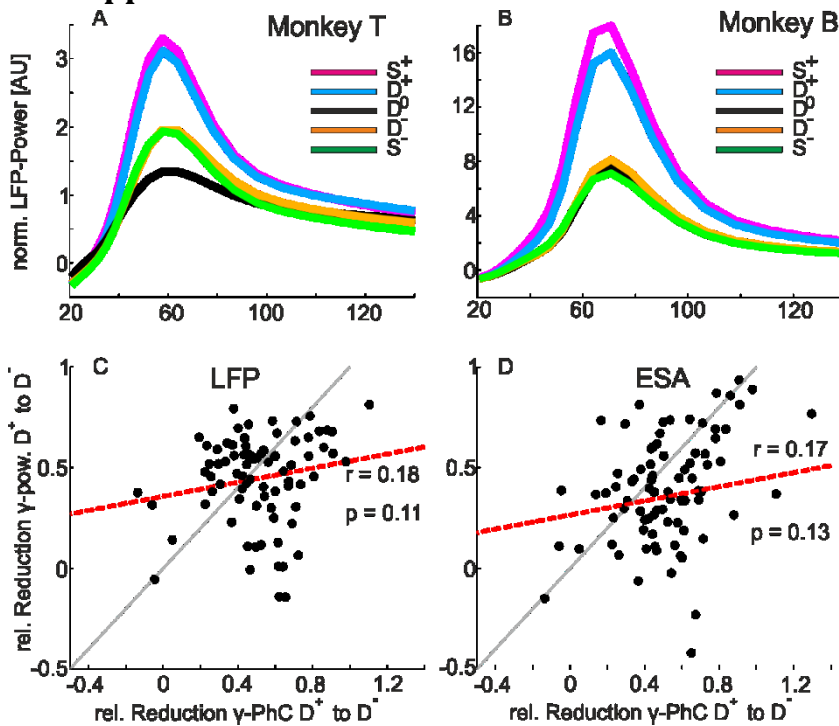
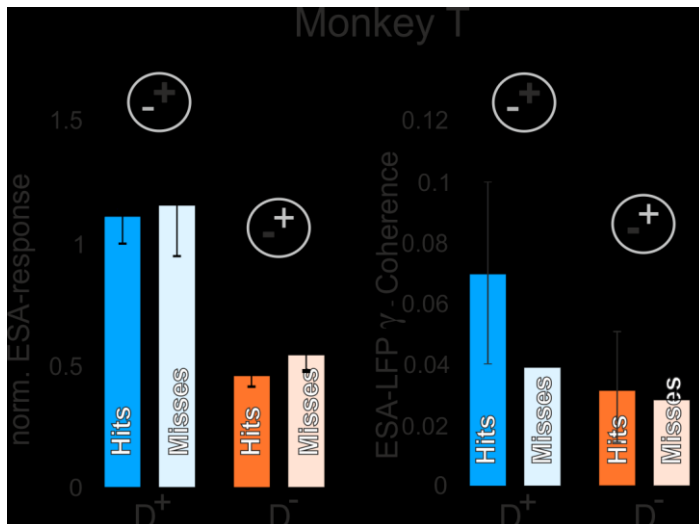


**Figure 15:** *A*, Average spectrum of normalized LFP-power during MCs 2/3 for the 5 task conditions of all recording sessions for monkey T. *B*, same as in A but for monkey B. *C*, Scatterplot of attention-dependent relative reduction of ESA-LFP  $\gamma$ -PhC from  $D^+$  to  $D^-$  vs. the relative reduction of LFP  $\gamma$ -power between these conditions. The gray line is the line of identity, the red dashed line the regression line. *D*, same as in *C*, but for comparison ESA-LFP  $\gamma$ -PhC vs. ESA  $\gamma$ -power.

#### 3.2.1 Supplementary Results

Neuronal correlates and behavioral outcome for misses vs. hits

Due to the small number of trials where monkey B failed to detect the reappearance of the target shape (misses), the comparison between misses and correctly executed trials was restricted to monkey T. In contrast to false alarms, there is no behavioral response to which the analysis could be triggered. We therefore compared the time period representing the second half (400 ms) of the morph cycle in which the target shape became apparent, to the same period of correctly terminated trials (ending 200 ms prior to the behavioral response). The normalized ESA-responses for conditions which required attending the stimulus inducing stronger responses ( $D^+$ ) were not significantly different between hits and misses (hits: 1.16, misses: 1.15,  $n = 68$ ,  $z$ -score = 0.3745;  $p = 0.355$ ,  $z$ -transform, cf. 3.1.3 Materials and Methods). There was a small and significant difference between misses and correctly executed trials for double conditions requiring to attend the stimulus inducing weaker responses ( $D^-$ ) with higher ESA-responses for misses (hits: 0.46, misses: 0.54,  $n = 108$ ,  $z$ -score = 1.82;  $p = 0.034$ ,  $z$ -transform). In contrast, the magnitude of  $\gamma$ -synchronization decreased by 43 % for misses as compared to correctly executed trials during  $D^+$  conditions. This difference was significant (hits: 0.07, misses: 0.04,  $n = 49$ ,  $z$ -score = -1.65;  $p = 0.0495$ ,  $z$ -transform), whereas there was no significant



difference between misses and hits for D<sup>-</sup> conditions (hits: 0.03, misses: 0.0288, n = 103, z-score: -0.3659, p = 0.3557)

**Figure 16:** Neuronal correlates of different behavioral outcomes. **Left,** Median normalized ESA responses just before correct (dark blue and orange) and erroneous (light blue and orange bars, misses) responses in trials requiring attention for one of the two stimuli within the pRF. Error-bars indicate 95% confidence intervals. **Right,** same as for left subplot but for  $\gamma$ -synchronization between ESA and LFP, Note, that error-bars here indicate 95 % of coherence values generated from 1000 times compiling sets of correctly performed trials (c.f. Materials and Methods). The synchronization value for error trials represents the coherence of all error trials pooled

## Chapter 4

### 4.1 Optimizing the Yield of Multi-Unit Activity by Including the Entire Spiking Activity

Declaration on the contribution of the candidate to a multi-author article, which is included as a chapter in the submitted doctoral thesis.

Experimental concept and design: 45 %

Data acquisition: 20 %

Data analysis: 60 %

Data interpretation: 60 %

Preparation of Figures and Tables: 50 %

Drafting of the manuscript: 40 %

Date:

Signature:

This chapter was published as: *Drebitz, E., Schledde, B., Kreiter, A. K. & Wegener, D. Optimizing the Yield of Multi-Unit Activity by Including the Entire Spiking Activity. Front. Neurosci. 13, 83 (2019)*

## **Optimizing the Yield of Multi-Unit Activity by Including the Entire Spiking Activity**

Eric Drebitz<sup>1</sup>, Bastian Schledde<sup>1</sup>, Iris Grothe<sup>1</sup>, Andreas K. Kreiter<sup>1</sup>, Detlef Wegener<sup>1</sup>

<sup>1</sup> Brain Research Institute, Center for Cognitive Sciences, University of Bremen

### **4.1.1 Abstract**

Neurophysiological data acquisition using multi-electrode arrays and/or (semi-) chronic recordings frequently has to deal with low signal-to-noise ratio (SNR) of neuronal responses and potential failure of detecting evoked responses within random background fluctuations. Conventional methods to extract action potentials (spikes) from background noise often apply thresholds to the recorded signal, usually allowing reliable detection of spikes when data exhibit a good SNR, but often failing when SNR is poor. We here investigate a threshold-independent, fast, and automated procedure for analysis of low SNR data, based on fullwave-rectification and low-pass filtering the signal as a measure of the entire spiking activity (ESA). We investigate the sensitivity and reliability of the ESA-signal for detecting evoked responses by applying an automated receptive field (RF) mapping procedure to semi-chronically recorded data from primary visual cortex (V1) of five macaque monkeys. For recording sites with low SNR, the usage of ESA improved the detection rate of RFs by a factor of 2.5 in comparison to MUA-based detection. For recording sites with medium and high SNR, ESA still delivered 30% more RFs than MUA. This significantly higher yield of ESA-based RF-detection still hold true when using an iterative procedure for determining the optimal spike threshold for each MUA individually. Moreover, selectivity measures for ESA-based RFs were quite compatible with MUA-based RFs. Regarding RF size, ESA delivered larger RFs than thresholded MUA, but size difference was consistent over all SNR fractions. Regarding orientation selectivity, ESA delivered more sites with significant orientation-dependent responses but with somewhat lower orientation indexes than MUA. However, preferred orientations were similar for both signal types. The results suggest that ESA is a powerful signal for applications requiring automated, fast, and reliable response detection, as e.g. brain-computer interfaces and neuroprosthetics, due to its high sensitivity and its independence from user-dependent intervention. Because the full information of the spiking activity is preserved, ESA also constitutes a valuable alternative for offline analysis of data with limited SNR.

### 4.1.2 Introduction

As an early step during analysis of extracellularly recorded signals, the actual spiking response of a neuron, or a group of neurons, usually needs to be separated from the background noise of the recorded signal. A common procedure is to set up an amplitude threshold to the high-passed neuronal signal. This threshold can be set manually or be defined automatically based on statistical likelihood. Frequently used methods for automatic threshold definitions use multiples of the standard deviation of the high-passed signal<sup>243</sup> or the median of the absolute signal<sup>244</sup>. Amplitude threshold-based spike detection has been proven successful in data with good SNR, but its performance declines significantly with decreasing SNR<sup>245</sup>. Other methods such as template matching<sup>246</sup> and wavelet-based extraction of time- and frequency-resolved spike features<sup>244,245,247,248</sup> either require a priori knowledge about the spike form, or an extensive amount of processing<sup>249</sup>. Yet, robust methods for dealing with low SNR data become particularly important with the increased importance of multi-electrode arrays used for large-scale neuronal recordings and brain-computer interfacing<sup>250-252</sup>, and other semi-chronic recording techniques<sup>253-255</sup>. In contrast to acute recordings with separately controlled microelectrodes, however, the position of array electrodes is fixed, or electrodes are more difficult to adjust. It is hence either impossible or difficult to carefully guide individual electrodes for optimizing a neuron's signal, resulting in highly variable magnitudes of extracellular action potential waveforms<sup>256</sup>. Additionally, signals of (semi-) chronically implanted electrodes degrade over time, due to local tissue responses<sup>257,258</sup>. Both issues are likely to result in a high number of channels exhibiting low SNR.

Analysis of such data is usually confined to the local field potential (LFP), because thresholding spikes in low SNR responses potentially results in a high number of either false positives or false negatives, depending on the threshold level. Hence, thresholding may have a significant impact on the estimated strength and temporal structure of the response, and interpretation of such data is problematic. The LFP, on the other hand, represents the integrated neuronal activity in close neighborhood of the electrode and constitutes a sensitive measure of neuronal activity<sup>259,260</sup>. Yet, the LFP reflects the sum of all local transmembrane currents rather than the output signal of the recorded neurons. Analysis of the latter, therefore, requires a reliable method to efficiently segregate stimulus responses from unspecific background noise, particularly at low and medium SNR recording sites. At the same time, there should be no trade-off at recording sites with high SNR when compared to established methods based on

thresholding.

We hypothesized that a method introduced in the early 1990s by Eckhorn and colleagues<sup>219,261-263</sup> possesses the critical properties to serve as such a reliable signal for detecting evoked responses in low SNR data. This method was invented for analyzing correlated activity at multi-unit recording sites, and is based on a fullwave-rectification of the high-passed neuronal signal (containing the spike information), followed by low-pass filtering. The method delivers a continuous instead of a binary signal, and represents the aggregated spiking activity of neurons located about 50  $\mu\text{m}$  around the electrode's tip<sup>219,220</sup>. Its most important advantage is that it does not rely on setting up a threshold but takes all the available spiking information. Because of the final low-pass filtering it should be rather insensitive to random high-frequency noise, making it a highly promising candidate approach for detecting evoked responses when SNR is weak. For the remainder of the paper, we denote this signal as ESA (Entire Spiking Activity).

Since its introduction, ESA has been used as an alternative measure for multi-unit activity by several groups<sup>185,264,265</sup>, but many of its important properties are still awaiting quantitative description. The purpose of the present study is to analyze the potential of ESA for increasing the yield of multi-unit recordings at different SNRs, and to quantitatively compare evoked responses based on ESA and thresholded MUA. For the example of receptive field (RF) mapping, we analyze semi-chronic recordings from primary visual cortex (V1) of five macaque monkeys (*Macacca mulatta*), and compare ESA-based RF detection rates with both conventionally thresholded MUA and the LFP, and further analyze RF size and orientation selectivity between ESA- and MUA-based RFs obtained from the same high-frequency signal. We use two approaches to set the threshold for analyzing MUA: a standard procedure with a fixed threshold for all units, and a second, computationally time-consuming iterative procedure to determine the optimal threshold for each unit individually. The results show that ESA outperformed MUA in both cases, particularly when SNR was low. ESA-based RF detection was almost as sensitive as LFP-based detection, and RF parameters corresponded to those found with thresholded MUA. RF-sizes were slightly larger than MUA-RFs, due to considering all available spiking information, but size differences were consistent over all SNR fractions. Relative orientation sensitivity (i.e. number of sites with significantly biased responses for different orientations) was higher for ESA, while absolute orientation selectivity (i.e. orientation indexes) was slightly attenuated as compared to thresholded MUA. Independent of these differences, the majority of recording sites delivering a RF with both signal types was found to have similar preferred orientations. Thus, ESA constitutes a powerful source of information to be considered when depending on reliable and fast neuronal response detections,

such as for (semi-) chronic recordings or BCI-approaches, as well as for increasing the information content of low SNR data for offline analysis.

### **4.1.3 Materials and Methods**

#### ***Subjects and Surgical Procedures***

Five male macaque monkeys (*Macaca mulatta*) were implanted with custom-made head holders and recording chambers under aseptic conditions and propofol/remifentanyl anesthesia. Four animals (monkeys B, P, V, and F) were implanted with a V1 microdrive array, allowing for bidirectional movement of six semi-chronically inserted electrodes<sup>254</sup>. The fifth animal (monkey T) was implanted with a recording chamber located above areas V4 and V1, allowing for bidirectional movement of up to four electrodes. Details on anesthesia, analgesia, and surgical procedures are reported elsewhere<sup>86,185,213,254</sup>. All procedures were in accordance with the Regulations for the Welfare of Experimental Animals issued by the Federal Government of Germany and with the guidelines of the European Union (2010/63/EU) for care and use of laboratory animals, and were approved by the local authorities (Senator für Gesundheit, Bremen, Germany).

#### **Visual Stimuli and Behavioral Task**

Data was acquired with an automatic bar-mapping procedure to stimulate the visual field region of interest, similar to the method described by Fiorani et al. (2014)<sup>266</sup>. The mapping was performed for different scientific projects not reported here. For the stimulation details that follow, task parameters of monkey T are stated in the text, and deviating parameters of one or more other animals are given in brackets. Visual stimulation was performed on a 20-inch (22-inch) CRT-screen, with a resolution of 1024 x 768 (1280 x 1024) pixels at 100 Hz vertical refresh rate. Monkeys were placed in a custom-made primate chair 90 (80) cm in front of the screen. Appearance of the central fixation point (FP) indicated trial start and animals were given 2 sec to initiate the trial by gazing at the FP and pressing a lever. Following a blank period of 820 (300) ms, a high-contrast bar appeared on screen and moved with constant speed in one of 12 motion directions (separated by 30°), and disappeared at the end of the trajectory. Length of bars (3.2 - 8.2°), motion trajectories (2.5 - 10.75°), and stimulus speed (1.9 – 4.7 °/sec) varied between animals, recording sites, and occasionally between recording sessions, depending on

the spatial area to be covered (16 – 64 deg<sup>2</sup>). Monkeys were required to keep fixation throughout the trial and to indicate a decrease in FP luminance occurring during a pseudo-random interval between 250 and 1250 ms after bar disappearance, by releasing the lever within a time period from 150 to 750 ms after FP dimming. To ensure that animals stayed alert throughout the trial, FP dimming occurred already during bar presentation in about 10 % of trials. These trials did not enter data analysis. Successive trials were separated by a 2 sec inter-trial interval. Eye position was monitored by video-oculography (monkey T: ISCAN Inc., MA, USA; monkeys B, P, V, and F: custom-made eye tracking system). Correctly performed trials were rewarded with a small amount of water or diluted grape juice. Responding too soon or too late, and eye movements of more than 0.5° (1°) away from the FP caused immediate trial termination without reward.

### **Data acquisition**

Neuronal data was recorded using up to six epoxy- or glass-insulated tungsten electrodes (125 µm diameter, 1-3 MΩ, FHC Inc., Bowdoin, ME, USA). Two different recording setups were used for data acquisition. In the first setup (monkeys B and P), the electrode signal was sampled at 25 kHz frequency, amplified 3000 fold (10 x, custom-made head stage, 300 x, custom-made main-amplifier), and band-passed between 0.7 and 5 kHz for receiving the spike information. For the LFP, the amplified electrode signal was low-passed at 300 Hz and down-sampled to 1 kHz. Hardware-filtered data was then digitized at 16 bit ADC resolution. In the second setup, the electrode signal was amplified using either a custom-made head stage (monkeys V and F), or a wideband preamplifier (monkey T; MPA32I, Multi Channel Systems, Reutlingen, Germany), both with a gain of 10, and a main-amplifier (PGA 64, 1 -5000 Hz, Multi Channel Systems, Reutlingen, Germany) with a gain of 1000. The amplified raw-signal was digitized with a sampling-rate of 25 kHz and a resolution of 12 (monkey T) or 16 bits (monkeys V and F). Electrode signals were referenced either against a low impedance electrode (< 0.1 MΩ) implanted into the frontal skull bone and touching the dura (monkeys B, P, V, F), or against the titanium recording chamber (monkey T), which was screwed into the bone and touching the dura.

### **Data analysis**

All offline analyses were performed with customized MATLAB-scripts (Mathworks, Natick, MA, USA). As described above, data of monkeys B and P was already band-pass filtered before

digitizing. Data of monkeys T, V, and F was filtered offline either between 0.7 – 5 kHz (monkeys V and F) or 0.3 – 12.5 kHz (monkey T) for isolating the high-frequency components (spikes), and low-passed either below 300 Hz (monkeys V and F) or 170 Hz (monkey T) for the low-frequency components (LFP). All offline filters were equiripple FIR-filters, applied in forward and backward direction to avoid phase shifts.

Spike detection for analyzing thresholded MUA was done using the method introduced by Quiñero et al. (2004), defining the threshold  $Thr$  as:

$$(1) \quad Thr = a * \text{median} \left( \frac{|x|}{0.6745} \right),$$

where  $x$  represents the high-passed data of which the median is taken and  $a$  represents a factor for different threshold levels. This factor was set to  $a = 3$  for the standard procedure, and was varied between  $a = 2$  and  $a = 4$  (in steps of 0.5) for the iterative procedure. To take advantage of the full spike information, no further spike sorting was performed, and all events surpassing the threshold were used (Figure 17A). Spike times were binned with a resolution of 1 ms and convolved with a Gaussian kernel ( $\sigma = 25$  ms) to obtain the spike-density function (SDF).

ESA was calculated on the same high-passed data, but instead of setting a threshold the data was full-wave rectified and low-pass filtered in forward and backward direction (Figure 17B), and down-sampled to 1 kHz<sup>220,261,262</sup>. To achieve best comparability, low-pass filtering was performed by a Gaussian filter with the same characteristics as used for calculating the SDF.

LFP power was calculated by convolving the low-passed signal with complex Morlet's wavelets<sup>223</sup>, as described in more detail elsewhere<sup>103,224</sup>. The resulting complex coefficients  $\tilde{x}$

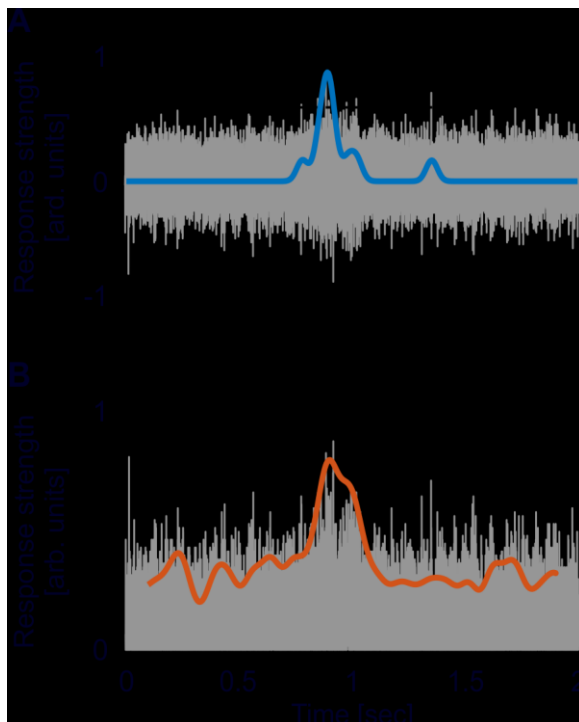


**Figure 17:** Exemplary trace of a single-trial illustrating analysis of MUA and ESA. (A) For MUA, a threshold (dashed line, cf. equation 1) based on the method introduced by Quiñero et al. (2004) was applied to the high-passed signal (gray trace). All events surpassing the threshold were then used for calculating the SDF (blue line). (B) For ESA, analysis is based on the full-wave rectified signal, i.e., the absolute values of the high-passed signal (gray trace), and then low-pass filtered (red line), using the same filter settings as for the SDF. This computation is independent of setting a threshold. Ordinate scaling is identical in both plots, SDF and ESA traces are both upscaled by a factor of 5 for visual purposes. Note that due to line thickness and time span, gaps between adjacent spike events are hardly visible. The inset in (B) shows a time period of 100ms to illustrate the time course of the rectified signal in more detail.

at time  $t$  and frequency  $f$  can also be expressed by their amplitude  $A$  and phase  $\Phi$  such that:

$$(2) \quad \tilde{x}(t, f) = A(t, f)e^{i\Phi(t, f)}.$$

Power was calculated by taking the square of the absolute value of  $\tilde{x}(t, f)$ , divided by the Nyquist-frequency (500 Hz). For each recording site, the power values for each time-frequency bin were normalized by first subtraction of and then division by the mean power spectrum of the spontaneous activity (obtained during the blank period prior to bar onset, excluding the first 100 ms). From this time–frequency representation of the LFP power we extracted the time course of the average power between 40 and 120 Hz.

### Receptive field detection

RF analysis was limited to data having at least five repetitions of each bar direction. To allow for direct comparison between MUA, ESA, and LFP, all data was  $z$ -transformed according to Fiorani et al. (2014)<sup>266</sup>. To this end, we first subtracted the mean spontaneous activity (averaged over all trials and orientations) from the response to a given motion trajectory, and then divided by the standard deviation of the responses to this direction. For the LFP, this was based on the average power in the broad  $\gamma$ -frequency range (40 – 120 Hz). RF-locations were calculated using the back-projection method, which is described in more detail in Fiorani et al. (2014)<sup>266</sup>. In brief, for each specific time point mean  $z$ -transformed responses to each of the twelve motion directions were back-projected to the location and orientation of the bar on screen, to obtain activity maps spanned by the bars' size and path length (see Figure 2, Fiorani et al., 2014<sup>266</sup>). The geometrical mean of the averaged, aligned responses to each of the 12 bar motion directions then provides the merged activity map. To avoid multiplying by values below one, each activity map with a minimum  $z$ -value  $< 1$  was shifted by an offset parameter  $R_{off}$ , given by the difference between the actual minimum value and one. The final merged map was corrected for these offsets by subtracting the geometrical  $R_{off}$  mean. We then searched for areas with mean activity higher than half the maximum of all values within the map. Such areas were considered a RF if first, the diameter (recalculated from estimated RF area) was between  $0.6^\circ$  and  $2.6^\circ$ , and second, the average  $z$ -value was larger than 0.8. Recording sites with low SNR often contained several connected areas in their activity maps with values larger than half of the maximum amplitude. In these cases, we only considered the largest of these areas as RF, if all other areas were smaller than  $0.5^\circ$  in diameter. These rather conservative criteria are more likely to deliver false negatives than false positives. RF size was calculated based on the spatiotemporal resolution of the activity map and the number of entries defining the RF. With the exception of

estimating significance of orientation tuning (described below), all other analyses were based on the mean  $z$ -transformed response within these RF borders, calculated separately for each of the 12 motion trajectories.

### Orientation Tuning

For analysis of orientation tuning, we first verified whether a site's tuning was significant ( $P < 0.05$ ), using a method introduced by Grabska-Barwinska et al. (2012)<sup>267</sup> to test the reliability of response differences to different orientations for repeated stimulus presentations. The response in any given trial is represented by the mean, non-transformed activation over the time the bar is passing the RF. In detail, for identifying significantly tuned sites, the full set of  $n_\phi$  bar orientations was shown for  $n_k$  repetitions, and the average in the complex plane  $z_{PO(k)}$  was calculated for each of the repetitions  $k$ :

$$(3) \quad z_{PO(k)} = \frac{1}{n_\phi} \sum_\phi f(\Phi, k) e^{2i\Phi},$$

with  $f(\Phi, k)$  representing the neuronal response to each orientation  $\Phi$ . The angle of  $z_{PO(k)}$  delivers the preferred orientation  $PO$  from each repetition. The vector average  $\langle z_{PO} \rangle$  of the normalized vectors  $z_{PO(k)}$  for all repetitions can then be calculated by:

$$(4) \quad \langle z_{PO} \rangle = \frac{1}{n_k} \sum_k \frac{z_{PO(k)}}{|z_{PO(k)}|} = \frac{1}{n_k} \sum_k e^{2iPO(k)}.$$

The reproducibility of the preferred orientation  $r_{PO}$  is defined as the length of  $\langle z_{PO} \rangle$ :

$$(5) \quad r_{PO} = \frac{1}{n_k} \left| \sum_k e^{2iPO(k)} \right|.$$

The reproducibility is 1 if the  $PO$  is equal for all repetitions, and 0 if  $PO$  values are uniformly distributed on the  $0 - 180^\circ$  range. Significance of orientation tuning was determined by comparing the reproducibility  $r_{PO}$  to a probability distribution  $P(r_{PO(n_k)})$  obtained from Monte-Carlo simulations under the assumption of a uniform distribution of  $PO$ s.

Sites with significant orientation tuning were used for comparing the tuning between signal types based on an orientation selectivity index calculated by vector averaging<sup>268</sup>. If an average  $z$ -transformed response to any of the twelve bar directions was below zero, this value was multiplied with -1 and added to each of the twelve response vectors. Neuronal responses  $f(\Phi)$  to each of the  $n_\phi$  bar directions were represented in the complex plane and averaged:

$$(6) \quad \langle z \rangle = \frac{1}{n_\phi} \sum_\phi f(\Phi) e^{i2\Phi}.$$

The preferred orientation is then given by the halved angle of the average vector  $\langle z \rangle$ , and the tuning strength by its length  $|\langle z \rangle|$ .

### Statistical Analysis

For each monkey and signal type, the detection ratio  $DR$  of significant RFs was given by:

$$(7) \quad DR = \frac{N_{Signal}}{N_{all}},$$

where  $N_{Signal}$  corresponds to the number of significant RFs found for the signal type under investigation, and  $N_{all}$  corresponds to the total number of recording sites with a significant RF independent of signal type. Note that for each signal type, each recording site delivered maximally one RF by definition. Statistical analysis of detection rates was done by performing paired ANOVAs on the mean detection rates of each animal and post-hoc testing with Tukey's honestly significant difference (HSD) procedure, correcting for multiple comparisons. Statistical analysis of RF size and orientation selectivity was performed on sites delivering a significant RF for both ESA and thresholded MUA, pooled over all animals, using Wilcoxon signed rank tests. Effect size  $R$  was calculated by:

$$(8) \quad R = \frac{|Z|}{\sqrt{N}},$$

where  $Z$  is taken from the Wilcoxon test statistics, and  $N$  represents the total number of samples.

### 4.1.4 Results

The aim of the study was to assess the sensitivity of the fullwave-rectified, low-passed spiking activity (ESA) for unsupervised detection of visual responses. For directly comparing ESA performance under different SNR conditions with conventionally thresholded MUA and with the LFP, we used a data-set of semi-chronic intra-cortical recordings from area V1 of five macaque monkeys. Data was acquired during an automatic bar mapping procedure. We used two approaches to set the threshold for analyzing MUA-based detection. The first approach (standard procedure) used a multiplication factor of  $a = 3$  for all data (see 4.1.3 Material and Methods). The resultant threshold level was found to be quite robust against false positives and false negatives. The second approach used an iterative procedure with multiplication factors of  $a = 2$  to  $a = 4$  (in steps of 0.5) to find the optimal threshold for each individual unit. Although this procedure is time-consuming and requires computing of RF maps for each threshold, it maximizes the yield of MUA-based RF detection. Note, however, that it requires a priori knowledge to distinguish evoked responses from false positives. The final dataset included all

recording sites delivering an RF for at least one of the three signals types (standard procedure:  $N = 653$ , iterative procedure:  $N = 656$ ).

### Quantitative comparison of RF detection between signal types

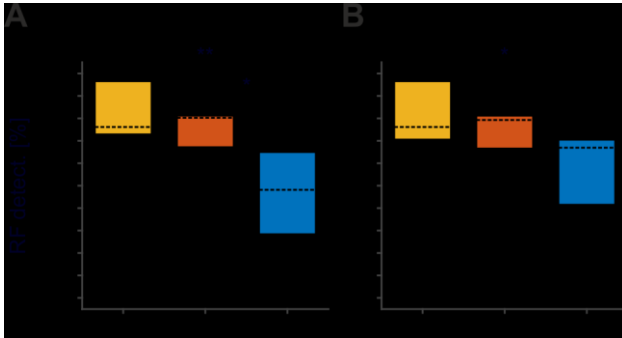


**Figure 18:** Comparison of RF detection rate between LFP, ESA, and MUA. (A) Standard approach for thresholding MUA. (B) Optimized, iterative approach for thresholding MUA to maximize MUA-based detection rate. For each signal type, boxplots are based on detection rates of individual animals. Detection rates refer to the absolute number of RFs detected relative to the number of recording sites with a significant visual activation for at least one of the signals, merged over all animals. Boxes indicate the 25<sup>th</sup> and 75<sup>th</sup> percentile, dashed lines indicate the medians, and whiskers indicate the full range of data. Asterisks indicate statistical difference for  $\alpha < 0.5\%$  (\*) and  $\alpha < 0.05\%$  (\*\*), respectively.

We first analyzed RF detection rates for ESA and conventional MUA, based on signal strength and area of activation (see 4.1.3 Material and Methods), and compared it to LFP-based detection rates. Figure 18 provides boxplot histograms of the pooled data across signal types for each of the two MUA procedures. ESA delivered an RF at 500 recording sites, which was close to the detection rate of the LFP ( $N = 570$ ). In contrast, MUA delivered an RF at 337 recording sites using the standard procedure, and at 399 recording sites using the iterative procedure. The latter provides the maximum of RFs to be obtained by thresholding. Table 2 summarizes the number of RFs for each individual animal and signal type.

Comparing across animals, ESA-based detection delivered most RFs in three of the five animals, while in the remaining two animals most RFs were obtained using the LFP. Importantly, ESA delivered more RFs than thresholded MUA in each individual animal, regardless of the procedure to set the threshold. Note that this was true albeit individual animals were recorded for different experimental purposes, using different recording setups and filter settings, and predominant recording layers varied between animals. Thus, the higher detection rates obtained with the ESA signal were not due to specific experimental conditions but a general outcome independent of the specific recording details.

We performed the statistical analysis on RF detection rates per thresholding procedure and across animals. For the standard procedure, a 1-way RM-ANOVA confirmed significant differences between signal-types ( $F(2,14) = 9.28$ ,  $P = 0.008$ ,  $N = 5$ ). Post-hoc Tukey HSD tests showed that the percentage of detected RFs based on ESA was significantly higher than detection rates for thresholded MUA ( $P = 0.026$ ), while detection rates between ESA and LFP

were statistically indistinguishable ( $P = 0.739$ ). For the iterative procedure, the difference between ESA- and MUA-based detection now failed to reach significance ( $P = 0.113$ ). Note, however, that also in the iterative procedure ESA delivered considerably more RFs than MUA in each individual animal (mean increase: 25%, range: 9 - 125%).

**Table 2:** Number of detected RFs for individual subjects and signal types.

Monkey	Total $N$	LFP		ESA		MUA	
		$N$	%	$N$	%	$N$	%
B	130	99	76.2	109	83.9	83 (87)	63.9 (66.9)
F	81 (82)	55	67.9 (67.1)	65	80.3 (79.3)	39 (57)	48.2 (69.5)
P	219	212	96.8	176	80.4	150 (161)	68.5 (73.5)
T	172	166	96.5	118	71.1	65 (80)	37.8 (48.2)
V	51 (53)	38	74.5 (71.7)	32	62.8 (60.4)	0 (14)	0 (26.4)
Total	653 (656)	570	87.3 (86.9)	500	76.6 (76.2)	337 (399)	51.6 (60.8)

*If different between standard procedure and iterative procedure, numbers in brackets refer to the iterative procedure.*

### Dependence of RF detection on SNR

We next investigated detection rates under different SNR conditions. When recording with (semi-) chronically implanted electrodes or electrode arrays, the electrodes' tips are usually not optimally positioned to the neurons in their vicinity, such that spike amplitudes may surpass background fluctuations only marginally. Figure 19A provides an example of a single trial under such poor SNR conditions. Although there was a significant visual response in the LFP, spike events at this site had very small amplitudes and only a few passed the threshold, calculated based on equation 1 with  $a = 2$  (Figure 19A, top panel). The resultant visual response map, computed over all trials, did not reveal any responsive region in the stimulated visual space based on the thresholded MUA (Figure 19E, left panel). Full-wave rectification and low-pass filtering the signal, however, revealed a small amplitude modulation during the course of the trial (Figure 19A, lower panel). Because in the ESA-signal such small modulations can be reliably detected in trials with low SNR, the ESA-based analysis of the same data provided a visual response map with a significant area of activation (Figure 19F, left panel). A second example from a different monkey is presented in the second-most left panels in Figures 19E and 19F. Under conditions of high SNR, on the other hand, both thresholded MUA and ESA reliably isolate the evoked spiking activity from background noise (Figure 19C), resulting in

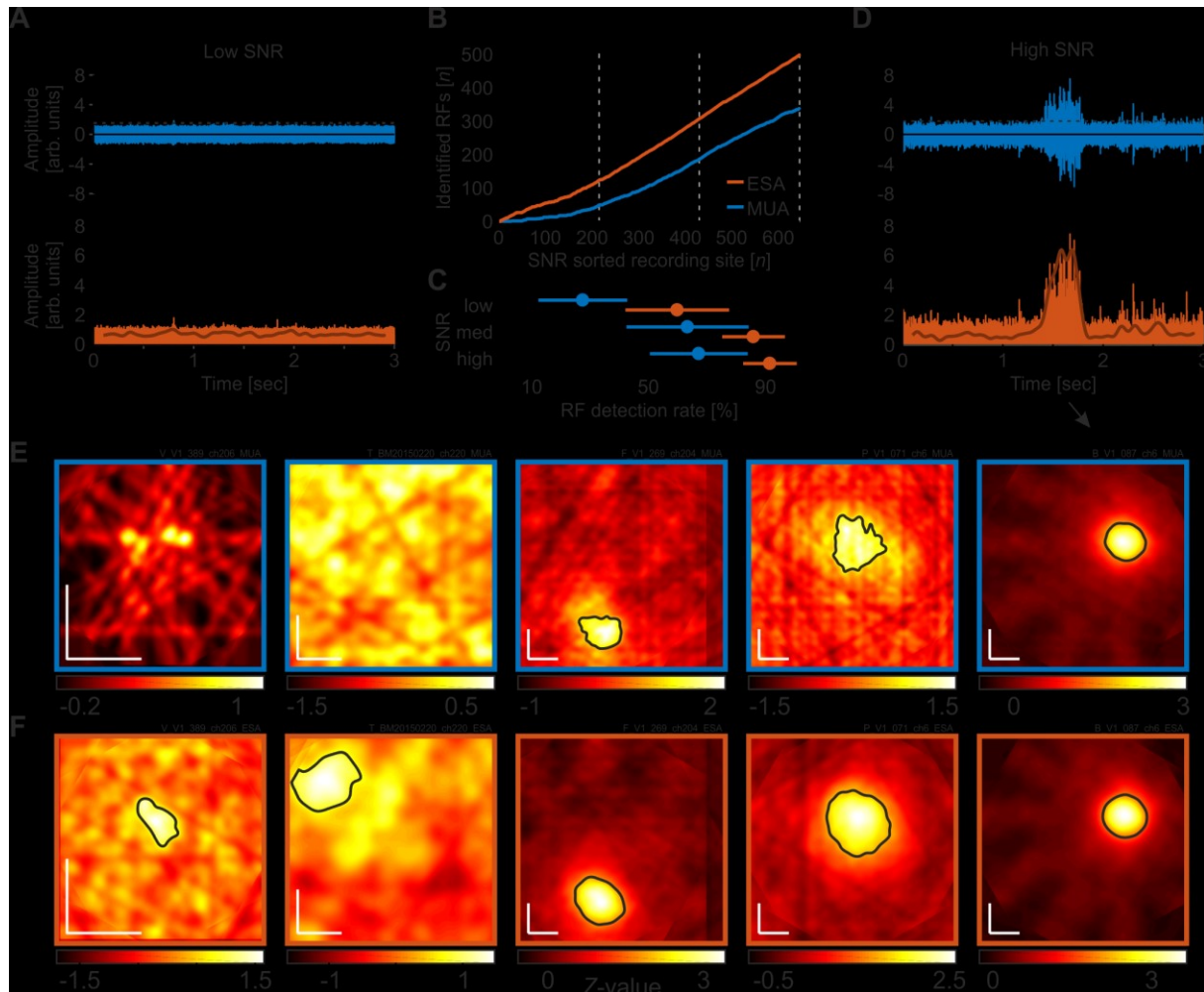


**Figure 19:** RF detection rates in dependence of signal-to-noise ratio (SNR). **(A)** High-pass filtered neuronal activity with very poor SNR (rank 4 out of 653). The upper panel depicts a single trial in response to a motion direction that reliably modulated the LFP. The dashed line indicates the threshold as calculated over all trials, using the method of Quiroga et al. (2004) with a median multiplication factor of  $a = 2$ . Events surpassing the threshold are used to calculate the spike density function. The lower panel shows the same high-passed signal after full-wave rectification. Subsequent low-pass filtering provides the ESA-signal (thick line), revealing a small amplitude modulation during the course of the trial. **(B)** Cumulative distribution of the number of RFs detected using either MUA or ESA, sorted by SNR. Dashed lines distinguish equally large fractions of recording sites with low, medium, and high SNR, as used for statistical analysis. Arrows indicate the SNR ranks of the five example sites shown in (E,F). **(C)** Detection rates for low, medium, and high SNR sites, based on the respective detection rates of data from the individual animals, separately for ESA and MUA. Disks and lines indicate mean  $\pm$  S.D., respectively. **(D)** Same as in (A), for a recording site with high SNR (rank 632). **(E,F)** Visual response maps based on thresholded MUA (**E**) and ESA (**F**) for the five recording sites indicated in (B). SNR rank increases from left to right. Vertical and horizontal white bars in the lower left corners indicate  $1^\circ$  of visual space. Black outlined areas depict significant visual responses (receptive fields). For the two left-most maps in (E) no significant visual response was found with any of the thresholds tested during the iterative procedure. Actual maps were calculated based on a median multiplication factor of  $a = 2$  for setting the threshold. Remaining maps (middle to right) were calculated after thresholding with  $a = 3$ .

visual response maps with clearly defined and similar RFs (Figure 19E and F, middle to right panels). However, when based on MUA, the detected RF regions sometimes appear a little bit

noisier and smaller (Figure 19E and F, middle and second rightmost panels).

To investigate the relation between RF detection rate and SNR in more detail, we calculated the SNR of all recording sites and determined detection rates as a function of SNR. SNR was calculated by dividing the median amplitude of all spike events surpassing the threshold by the threshold value itself. For reasons of comparability, the threshold was calculated by a multiplication factor of  $a = 3$ , as applied in the standard procedure. We used the same dataset as before, i.e. we also included those recordings for which we detected an RF in the LFP only to keep the total  $N$  constant. Figure 19B depicts the cumulative distribution of the number of RFs detected using either ESA or MUA, sorted from low to high SNR. Note that at low SNR, the two traces representing ESA and MUA strongly deviate, and even with medium and high SNR, the ESA slope is still steeper than the MUA slope.

For statistical analysis, we divided the dataset into three equally large groups of sites with low, medium, and high SNR (indicated by dashed lines in Figure 19B), and calculated the RF detection rate of each animal and group. Based on ESA, a significant visual response was detected at 59.3 %, 84.7 %, and 90.2 % of recording sites with low, medium, and high SNR, respectively. For thresholded MUA, the corresponding detection rates obtained by the standard procedure were 28 %, 62.8 %, and 66.5 %. A 2-way RM-ANOVA with the factors signal type and SNR revealed a main effect of both factors (signal type:  $F(1,2) = 14.87, P = 0.0182$  ; SNR:  $F(2,2) = 4.85, P = 0.0417, N = 5$ ), and no interaction ( $F(2,8) = 0.018, P = 0.548$ ). Post-hoc Tukey HSD multiple comparison tests showed that at low SNR, ESA-based detection rates were higher than MUA-based detection rates at the 95 % confidence level, while the difference in detection rates at medium and high SNR was statistically not significant (Figure 19C). The iterative procedure delivered equivalent statistical conclusions.

Additionally, because ESA delivered RFs at recording sites where MUA did not (iterative procedure:  $N = 115$ ), we estimated the likelihood to get a false positive RF detection. This was done by re-shuffling the time bins and labels of the raw PSTH. We then computed visual activity maps as before (cf. chapter 3.1.4). The actual number of RFs found with this procedure was zero, indicating a very low likelihood that the additionally detected ESA-RFs consist of a significant number of false positives.

### **RF size and orientation Tuning**

Higher detection rates in data with poor SNR do not necessarily imply that they will provide reliable estimates about the response characteristics of the underlying group of neurons. We

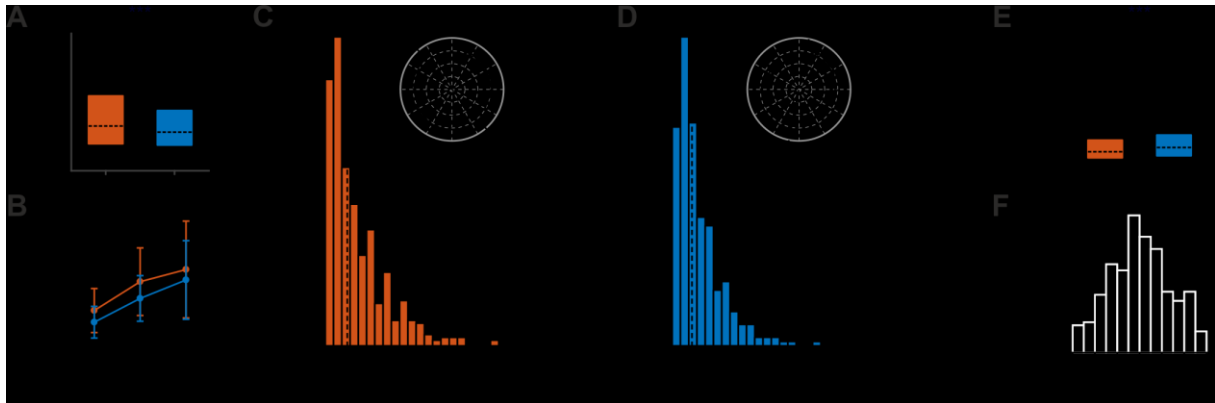


**Figure 20:** Comparison of stimulus selectivity between ESA and MUA. **(A)** RF area of recording sites with significant visually evoked response modulation for both ESA and MUA ( $N = 385$ ). **(B)** RF area as a function of SNR for same units as in (A). Error bars indicate S.D. **(C,D)** Distribution of orientation indexes for ESA **(C)** and MUA **(D)**. Dotted lines indicate median OI. Polar plot insets show exemplary orientation selective responses at median OI value for either signal type. **(E)** Direct comparison of orientation selectivity of units with significant orientation-selective responses for both MUA and ESA ( $N = 275$ ). **(F)** Signal-dependent difference in preferred orientation (IPO) for same units as in (E). Boxplot conventions as in Figure 2. Asterisks indicate statistical difference for  $\alpha < 0.005\%$  (\*\*\*)

therefore investigated the selectivity of ESA and thresholded MUA with respect to the estimated RF size and orientation tuning of the detected units. To get the maximal RF yield, we based this analysis on the iterative procedure for thresholding. Likewise, to obtain the maximal spike information from each unit, we used the smallest threshold that allowed detection of a significant visual response for that unit. Assuming idealized circular RFs, the mean calculated diameter  $\pm$  S.D. of ESA- and MUA-RFs was  $1.6 \pm 0.45$  and  $1.49 \pm 0.46^\circ$ , respectively. For comparison, the size of LFP-RFs was  $1.7 \pm 0.38^\circ$  and thus was slightly larger than for ESA and MUA. For statistical analysis, we limited the dataset to those units delivering a significant RF for both ESA and MUA and based the calculation on actual RF areas. ESA-RFs were found to be significantly larger than MUA-RFs (Wilcoxon signed rank test,  $Z = 9.84$ ,  $P < 10^{-22}$ ,  $N = 385$ ,  $R = 0.355$ ) (Figure 20A). A Tukey HSD multi-comparison analysis for units with low, medium, and high SNR revealed that the estimated size of both signals increased from low to high SNR (both  $P < 10^{-5}$ ,  $N = [30 \ 60 \ 295]$ ), but the size difference between ESA- and MUA-RFs did not differ between SNR groups (1-way ANOVA,  $F(2,382) = 2.394$ ,  $P = 0.09$ ,  $N = [30 \ 60 \ 295]$ ) (Figure 4B).

Orientation selectivity was estimated based on vector averaging the responses to the six bar orientations, according to Grabska-Barwinska et al. (2012)<sup>267</sup>. The method labels orientation tuning as significant depending on the reliability of orientation-related responses over trials, but independent of the absolute orientation index (OI). Orientation tuning was considered significant at 97.8 % ( $N = 489$ ) of all recording sites with a significant ESA-RF, and at 72.2 %

( $N = 288$ ) of all sites with a significant MUA-RF. Figures 20C and D show the distribution of OI values for the two signal types. Polar plot insets depict two exemplary recording sites with an OI close to the population medians for ESA (0.053) and MUA (0.048).

Statistical analysis was performed on units with a significant orientation tuning for both ESA- and MUA-RFs (Fig. 20E). For this subset of sites, MUA turned out to be significantly more orientation selective than ESA (Wilcoxon signed rank test,  $Z = 3.8$ ,  $P < 10^{-3}$ ,  $N = 275$ ), but the effect size was small ( $R = 0.162$ ). Despite this reduction in absolute selectivity, 43 % ( $N = 117$ ) of the recording sites had about the same preferred orientation (deviation  $< 15^\circ$ ) independent of signal type, and 70 % ( $N = 164$ ) of recording sites did not differ by more than  $30^\circ$ , i.e. preferred orientation was within the range of two neighboring stimulus orientations (Fig. 20F).

### 4.1.5 Discussion

Full-wave rectification and subsequent low-pass filtering of multi-unit spiking activity was introduced by Eckhorn and colleagues<sup>219,261-263</sup> to improve spectral frequency analysis of correlated activity, and has been used by several groups as an alternative measure for multi-unit activity<sup>185,264,265</sup>. Because this method does not involve setting a threshold for cutting spike amplitudes, full information about the neuronal response is preserved. We hypothesized that this way of pre-processing is particularly effective for data with poor SNR. Even if spike amplitudes do not surpass the background, aggregated spike events in the rectified signal will be reflected in the low-passed derivate due to their different temporal structure, while random background fluctuations get attenuated. Thresholding of such small spikes, on the other hand, is likely to result in both false positive and false negative spike events, thus blurring the available stimulus information.

We tested this hypothesis by using data from semi-chronic recordings of primary visual cortex that was acquired during mapping procedures for testing visually evoked activity. The mapping procedures were performed for different research projects having different target layers within V1. In addition, electrodes were located within the tissue for variable time periods (days to weeks to months), and recording details (hardware, filter) varied across animals. This explains the variance in detection rates across animals (Table 2), but more importantly, it shows that the findings of the current study do not result from specific experimental conditions. Instead, the basically same result across animals suggests a general advantage of ESA over thresholded MUA for detecting evoked activity in the high-frequent signal of neuronal responses. Over all

SNR fractions, ESA delivered about 50 % more RF estimates than conventional MUA, and was only slightly less sensitive than the broadband-gamma LFP (40 – 120 Hz). This increased detection rate was mainly due to a much higher sensitivity for detecting RFs in low SNR recordings. With the standard procedure, ESA delivered 2.5 times the number of RFs as compared to MUA. Optimizing the yield of MUA-based detection by iteratively applying a series of thresholds to each unit allowed to increase the number of detected RFs in low SNR data by about 60 %, but this was still significantly less than ESA-based detection rates. For medium and high SNR, ESA delivered more RFs than MUA in each individual animal, independent of the procedure, but detection rates for ESA and MUA approximated and were statistically not different over the sample size of five animals.

Average RF size slightly increased from low to high SNR for both ESA and MUA, and ESA-RF size was about 17 % larger than MUA-RF size in units delivering an RF with both signals. Yet, this difference was consistent over all SNR fractions, indicating about the same reliability of both signal types. Similarly, ESA-RFs were found to have a slightly smaller absolute orientation selectivity than MUA-RFs, but for 70 % of recordings ESA and MUA delivered the same or a very similar preferred orientation. These results support the notion that ESA is a highly sensitive, selective, and reliable signal type significantly increasing the yield of recordings, particularly under conditions that do not allow optimal positioning of electrodes to isolate single units.

### **Increased sensitivity for detection of evoked responses**

As a rule of thumb, the amplitude of a spike decays as the inverse of the square of the distance to the recording electrode's tip. For example, the voltage amplitude of a spike generated at a soma with 10 to 30  $\mu\text{m}$  diameter will decay by about 90 % in 60 to 65  $\mu\text{m}$  distance from the recording electrode tip<sup>269-271</sup>. Thus spikes generated at larger distances from the electrode tip get lost in general background noise when not surpassing the threshold, or will be intermixed with noise when threshold is too low. Because of this negative effect on SNR, this introduces a significant limitation for detecting evoked responses. ESA, on the other hand, is sensitive for aggregated spikes even when having small amplitudes, and rather insensitive to random background noise. The resultant signal has a clearly improved SNR, as indicated by the strong increase in the yield of significantly modulated ESA-RFs with low SNR, and even the moderate though insignificant increase in yield for medium and high SNR data.

It is worth to note yet that the division into the three SNR groups is to some extent arbitrary.

We divided our dataset into equally large SNR fractions and categorized these as low, medium, and high. Our recordings were obtained from different cortical layers, in many sessions we were primarily interested in the LFP. Thus, only a few data may have been recorded under truly high SNR conditions, while some of the data representing the high SNR pool might have had a weak absolute SNR in fact. Thus, the slightly higher ESA-detection rates for medium and high SNR may disappear under conditions with overall higher SNR. However, our analyses show that ESA is particularly powerful to detect evoked responses when SNR conditions do not allow to set a legitimate threshold. This is particularly evident when comparing ESA detection rates with the optimized yet much weaker detection rates obtained after iteratively searching for the most appropriate threshold of each unit. Such low SNR conditions may result from larger distances between electrode tips and somata when using permanently implanted probes, or from cell loss, gliosis, or local tissue responses potentially associated with (semi-) chronic recording approaches<sup>258,272-276</sup>, which in turn makes it necessary to exclude single electrodes from further analysis. Here, ESA represents a powerful alternative to conventional thresholding of MUA activity and allows for a strongly increased yield of data, with the additional advantage that its application can be fully automatized.

### **Stimulus selectivity**

Because ESA is a neuronal mass signal and reflects the activity of a local population of neurons, the slight differences in RF size and absolute orientation selectivity may primarily be due to a larger group of neurons underlying the ESA-signal as compared to thresholded MUA. Supèr and Roelfsema (2005)<sup>222</sup> compared direction selectivity, response latency, figure ground segregation, and attentional modulation of ESA (denoted as MUA<sub>E</sub> in their article) to single units. In line with our results, the authors found a somewhat reduced direction selectivity but otherwise largely identical response characteristics. Because axonal and dendritic spikes are very small and the time course of postsynaptic potentials is slow, they concluded that ESA is representing the summed action potentials of neurons with a soma in the vicinity of the recording site rather than electrical fluctuations from other sources. This interpretation also explains the increase in RF size and the reduction of absolute orientation selectivity (Fig. 20). Because ESA is not discarding spikes below threshold, it integrates over more sources than conventional MUA, which necessarily results in a somewhat reduced stimulus selectivity. Brosch et al. (1997)<sup>219</sup> specified the effective range of ESA as approximately 50  $\mu\text{m}$  around the electrode tip. Referring to the classical finding that orientation preference of neurons only 25

to 50  $\mu\text{m}$  apart from each other may shift by about  $10^{\circ 277}$ , integration of smaller spikes from more distant somata is likely to explain the reduction in absolute orientation selectivity. In addition to this, the higher sensitivity for small spikes prevents, or at least attenuates the typical sampling bias towards large pyramidal neurons when thresholding spikes. Thus, the ESA database may include a larger diversity of cell types than the MUA database, including cells with larger RFs, smaller orientation selectivity, or different center-surround interactions, as found in different layers of V1<sup>278-280</sup>.

Apart from the slightly attenuated total stimulus selectivity, both the analysis of RF size as a function of SNR and cross-comparison of orientation selectivity across signal types primarily revealed that ESA delivers a reliable estimate of the response properties of the recorded group of neurons. First, although RFs were getting slightly larger with better responsiveness of the recording site (due to the reasons outlined above), this increase was found for both signal types and to equal extent. This indicates that even with poor SNR evoked responses were sufficiently well detected to allow for a reasonable estimation of the response properties of the local set of neurons. Second, the estimated preferred orientations were similar between ESA and MUA for the majority of recording sites. Importantly, the method we used for denoting a cell's response as either significantly or insignificantly being influenced by the orientation of the stimulus relies on reproducibility of responses rather than on absolute orientation selectivity. This diminishes the influence of random singular events for estimating response properties of the recorded group of neurons. The finding that almost 98 % of the ESA responses were classified as orientation-dependent (as compared to 72 % of the MUA responses) proves the high reliability of the ESA-signal to reveal even a small response bias towards one orientation. Detectability of such biases might be important for different purposes, as e.g. for selecting proper stimulus conditions or improving performance of decoding techniques.

Taken together, full-wave rectification and subsequent low-pass filtering of spiking activity effectively increases the signal's SNR and allows for more reliably detecting evoked responses in data with low SNR. Because no thresholding is applied, ESA considers the full spiking information and allows for reliable characterization of the response properties of the underlying group of neurons when conventional techniques may fail.

### **4.1.6 Author Contributions**

ED, AK, and DW designed the research. ED, BS, and DW performed the research. ED and DW

analyzed the data, prepared the figures, and drafted the manuscript. ED, BS, AK, and DW interpreted the results, edited and approved the final version of the manuscript.

### **4.1.7 Funding**

The work was supported by the German Research Foundation (DFG grants WE 5469/2-1, WE 5469/3-1, KR 1844/2-2, and KR 1844/4-1).

### **4.1.8 Acknowledgments**

The authors acknowledge support by Fingal Orlando Galashan, Johanna Barnstorf-Brandes, Hendrik Borgmeier, Emel Erdogdu, Lea Greifenberg, and Deniz Parmuk during data acquisition and analysis, Katrin Thoß and Ramazani Hakazimani for animal care, and Aleksandra Nadolski and Peter Bujotzek for technical assistance.

## Chapter 5

### 5.1 A novel approach for removing micro-stimulation artifacts and reconstruction of broad-band neuronal signals

Declaration on the contribution of the candidate to a multi-author article, which is included as a chapter in the submitted doctoral thesis.

Experimental concept and design:	50 %
Data acquisition:	65 %
Data analysis:	100 %
Data interpretation:	60 %
Preparation of Figures and Tables:	100 %
Drafting of the manuscript:	85 %

Date:

Signature:

This chapter is a manuscript that is currently under revision for submission.

## **A novel approach for removing micro-stimulation artifacts and reconstruction of broad-band neuronal signals**

Eric Drebitz<sup>1</sup>, Lukas-Paul Rausch, Andreas K. Kreiter<sup>1</sup>

<sup>1</sup> Brain Research Institute, Center for Cognitive Sciences, University of Bremen

### **5.1.1 Abstract**

#### **Background**

Electrical stimulation is a widely used method in the neurosciences with a variety of application fields. However, stimulation frequently induces large and long-lasting artifacts, which superimpose on the actual neuronal signal. Existing methods were developed for analyzing fast events such as spikes, but are not well suited for the restoration of LFP signals.

#### **New Method**

We developed a method that extracts artifact components while also leaving the LFP components of the neuronal signal intact. We based it on an exponential fit of the average artifact shape, which is subsequently adapted to the individual artifacts amplitude and then subtracted. Importantly, we used for fitting of the individual artifact only a short initial time window, in which the artifact is dominating the superimposition with the neuronal signal. Using this short period ensures that LFP components are not part of the fit, which leaves them unaffected by the subsequent artifact removal.

#### **Results**

By using the here presented method, we could diminish the substantial distortions of neuronal signals caused by electrical stimulation to levels that were statistically indistinguishable from the original data. Furthermore, the effect of stimulation on the phases of  $\gamma$ - and  $\beta$ - oscillations was reduced by 85 and 75 %, respectively.

#### **Comparison with Existing Methods**

This approach avoids signal loss as caused by methods cutting out artifacts and minimizes the distortion of the signals' temporal structure as compared to other approaches.

#### **Conclusion**

Our here presented method allows for a successful reconstruction of broad-band signals.

### 5.1.2 Introduction

Intra-cranial electrical stimulation of brain tissue is a standard method in the neurosciences. It is widely used in various fields of application. Among many others, it has been utilized for the topographical mapping of sensory and motor cortices (for detailed reviews see: Berlucchi, 2009<sup>281</sup>; Humphrey, 1986<sup>282</sup>), or for investigating the causal role of sensory neurons for perception<sup>283-287</sup>.

All these investigations exploit that neurons close to the stimulation site generate action potentials (APs) due to the applied currents<sup>288,289</sup>. The impact of these electrically evoked spikes can then be directly correlated to changes in perception and behavior or reveal anatomical connections between neurons at the stimulation site and other brain regions<sup>290-292</sup>. On the other hand, simultaneous recording of neuronal activity, while electric pulses are applied, is problematic because these pulses affect data acquisition by superimposing artifacts onto the actual neuronal signal<sup>293,294</sup>. These artifacts are often characterized by large initial transients, which subsequently decay rather slowly until reaching the pre-stimulation level of the neuronal signal<sup>295</sup>. For direct electrical stimulation of brain tissue, the course of this decaying period often resembles the sum of multiple exponential functions with different decay times. It reflects the resistive and capacitive properties of several components of the recording setup, as well as the recording electrodes<sup>289,296,297</sup>.

There have been several approaches for dealing with these signal obscuring artifacts in order to enable detection of APs and thereby characterize spiking activity. These approaches have been proven very successful in enabling AP detection for different experimental conditions resulting in different artifact shapes.

One approach is to cut out the stimulation period and replace it by linearly interpolating between the last data point before, and the first data point following the cutout period<sup>298,299</sup>. This method has been proven effective, for example, when recording auditory nerve action potentials while applying electric pulses to the cochlear<sup>300</sup>. This procedure is computationally efficient and particularly well suited for extracting short stimulation artifacts (170  $\mu$ s on average in Heffer and Fallon, (2008)<sup>300</sup>).

A method appropriate for removing longer-lasting artifacts of uniform size and shape is template subtraction. It is based on first calculating the artifact's shape by averaging over multiple stimulation periods and subsequently subtracting this average shape from each

individual stimulation period<sup>301-303</sup>. The template subtraction method is based on the assumption that the artifact characteristics, such as duration, amplitude, or decay characteristics are equal across stimulations.

Another approach for removing artifacts with variable size and shape employs a fitting procedure<sup>295</sup>. As mentioned above, Harding (1991)<sup>296</sup> reported that in their data, the stimulation artifact follows an exponentially decaying function composed of several terms with different decay times after the initial onset transient. Based on this, they performed a fitting procedure aiming to find an optimal exponential fit for each individual stimulation artifact and subtracted it from the actual data.

As previously mentioned, these methods were developed in the context of spike-train analyses, but not explicitly for investigations regarding the much slower components of the neuronal signal as contained in the local field potential (LFP). However, the LFP has gained more and more interest in the past years, since it is thought to reflect the temporal activity patterns of a local neuronal population<sup>103,178,185</sup> and it has proven very useful for investigations of long-range interactions<sup>9,107,183,184,240,304</sup>. Therefore, a method is required that is capable of removing artifact components, while leaving the original time course of the LFP unaffected, to allow for meaningful analysis of it in data-sets containing electrically evoked artifacts.

For several reasons, the previously mentioned methods do not optimally serve this purpose. When dealing with comparably long artifacts, the cutout method leads to a loss of signal information and strongly disturbs the original shape and composition of the neuronal signal, since it replaces the cutout period by linear interpolation. The template subtraction method is capable of reconstructing the LFP even for longer-lasting artifacts, but only when the artifacts sizes and shapes are highly constant across stimulations. In the frequent cases not fulfilling this requirement<sup>300,305,306</sup>, the subtraction of a non-optimal template would induce either inverted artifact components, when the template is too large or residual components will be left behind when the template is too small. In both cases, the temporal structure of the LFP will be strongly disturbed. Using a fit of each individual artifact, which is subtracted subsequently from the actual data does not solve the problems either. Especially within the temporally extended, gradually decaying, and smaller part of the artifact, these fits will inevitably include both artifact and signal components. Subtracting it would strongly disturb the temporal structure of the LFP. In summary, another method is required if (1) the LFP is in the focus of interest, and (2) the entire artifact duration is comparably long.

We, therefore, developed a method for signal reconstruction based on subtraction of an exponential fit, but in contrast to the previous work, we based this fit not on each individual

artifact, but the average artifact shape of a recording site. The averaging across artifacts ensures that the components of the artifacts are extracted and become subject of the fit, but not components of the neuronal activity during the stimulation periods since they are averaged out. We used the decay characteristics derived from this average fit and fixed them for the subsequent fitting of each individual artifact. We performed the second fitting for adapting the fitted function in amplitude to each individual artifact. For this, we used only a short initial period of each artifact, because these periods represent almost entirely the electric artifact, whereas the neuronal signal dominates later stages of the superimposition. Subsequently, we subtracted this second fit from the individual artifacts for signal reconstruction.

We demonstrate the reliability of our method for artifact removal and successful signal reconstruction using data recorded in the visual cortex of two macaque monkeys (*Macaca mulatta*) performing a visual attention task. While animals performed the task, we applied single electric pulses via micro-electrodes. The electric stimulation induced large and long-lasting artifacts superimposed on the recorded neuronal signal, which strongly interfered with the LFP.

Our here presented method reduced the substantial distortions of the neuronal signal to levels that were statistically indistinguishable from the period directly preceding the electrical stimulation. As a second measure for quantifying the degree of signal reconstruction, we compared the phases of  $\gamma$ - and  $\beta$ - oscillations determined in non-stimulated data, to the phases determined in the same data but with a superimposed artificial artifact, and the phases determined after application of our artifact removal procedure. We found that our method reduced phase differences by more than 85 % and 75 %, respectively. Also, we could show that the method is comparably well suited in enabling spike detection as other methods explicitly developed for this aim. In conclusion, the here presented method is a simple and effective approach for removing electrically evoked artifacts in neuronal data. The restored signal deviates only marginally from the actual neuronal signal, which allows for meaningful analyses of spikes and, more importantly for this work, the LFP.

### **5.1.3 Materials and Methods**

#### **Surgical preparation**

The data used in this study was recorded in two male macaque monkeys (*Macaca mulatta*) while they performed an attention task. Task design and surgical details are described in detail

in Drebitz et al. (2018)<sup>185</sup>. Experiments and surgical procedures were approved by the local authorities (Der Senator für Gesundheit, Bremen, Germany) and were in accordance with the regulation for the welfare of experimental animals issued by the Federal Government of Germany and with the guidelines of the European Union (2010/63/EU) for care and use of laboratory animals.

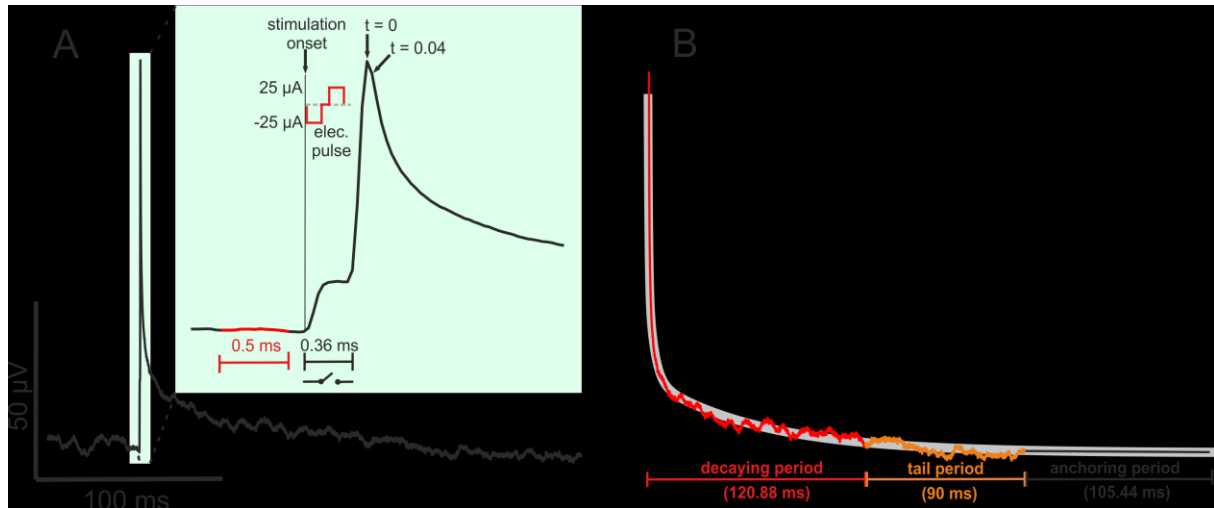


**Figure 21:** Example of an average artifact and definitions of signal periods. **A** Average artifact from 50 ms before until 220 ms after stimulation onset. Highlighted in green is the period shown in the inset. The inset depicts the averaging period for the pre-stimulation value (red colored), the onset time of the electrical stimulus (vertical black line) and its time course (red, elec. pulse). Simultaneously with stimulation onset, the main amplifier is decoupled from pre-amplifier, as indicated by the open switch symbol. The beginning of the decay period ( $t = 0$ ) and the beginning of the fitting period ( $t = 0.04$  ms) are indicated by arrows. **B** Structure of the fitting period for the average artifact shown in **A** as defined by our method. The fitting period (gray trace in the background) starts at  $t = 0.04$  ms (see **A**) and comprises the decaying period (red) until the artifact approaches the pre-stimulation level (see **A**, red period), the tail period (orange) and the anchoring period (black). It is used for fitting the average artifact. The duration of each period for this example is given in brackets.

## Electrical stimulation

For stimulation, a single glass-insulated microelectrode (1 M $\Omega$ , FHC Inc., Bowdoin, ME, USA) was placed semi-chronically in the supragranular layers (output layers) of area V2 before the actual recordings began. The distance between the recording electrodes in V4 and the stimulation electrode in V2 was between 8 and 12 mm. As return electrode served a low impedance (< 100 k $\Omega$ ) epoxy-insulated tungsten electrode (FHC Inc., Bowdoin, ME, USA) placed on top of the dura mater above V2.

A real-time stimulus generator (STG 4008, Multi-Channel Systems GmbH, Reutlingen, Germany) applied constant current stimuli. They consisted of a single, charge-balanced,

biphasic pulse with of a 100  $\mu\text{s}$  cathodic phase followed by a 60  $\mu\text{s}$  inter-phase gap and a 100  $\mu\text{s}$  anodic phase resulting in a total pulse duration of 260  $\mu\text{s}$  (Fig 1A). Pulse amplitude was 25  $\mu\text{A}$  (in Monkey II: 15  $\mu\text{A}$  in part of the data).

During each trial, single pulses were applied randomly in time but separated by at least 550 ms. The attention task contained trials of different lengths: the shortest trials contained two stimulation periods and the most extended four. Between trials was an inter-trial period of 2 s.

### **Electrophysiological recordings**

Simultaneous intra-cortical recordings in visual area V4 (parafoveal, dorsal V4) were performed using up to four epoxy-insulated tungsten microelectrodes (1–3  $\text{M}\Omega$ , FHC Inc., Bowdoin, ME, USA). Neuronal signals of monkey I were amplified 8000 fold and 20000 fold for monkey II (4x by wideband preamplifier MPA32I and 2000x (5000x) by PGA 64, 1-5000 Hz, Multi-Channel Systems GmbH, Reutlingen, Germany) and digitized at 25 kHz sampling frequency with 12-bit resolution. An electronic switch disconnected the main-amplifier inputs from the preamplifier while electric stimulation was applied for a period of 360  $\mu\text{s}$ , beginning simultaneously with electric stimulation (Fig 21A, inset). The signals were referenced against the individual titanium recording chambers (25 mm diameter), which were screwed into a corresponding trepanation of the cranial bone and touched the dura mater.

### **Artifact removal**

Stimulation artifacts differed in shape and duration considerably between different electrodes (compare, e.g., Fig. 21A, Fig 22A upper and lower panel) and have been described successfully by decaying functions with one or more exponential terms<sup>296,297</sup>. Their amplitude often exceeds the neural signal by order of magnitude or more and varies considerably, even at the same electrode. Moreover, due to the artifact size, the neuronal signal frequently reaches the recording chains working range limit (clipping). We, therefore, developed the artifact removal procedure based on fitting an exponentially decaying function to a recording site's average artifact shape. The amplitude of the fit is subsequently adjusted to the amplitude of each individual artifact before we subtracted it from the recorded signal. To avoid overfitting, we only used data from the first steep decay period of each individual artifact; the artifact strongly dominates this period of the superimposition. By using only this short initial period, we prevent the potential inclusion of neural signal components into the fit and their removal during signal

reconstruction.

### Fitting of average artifact shape

To determine the shape of the artifact, we computed the average across all stimulation periods of a recording site in the range between 500 ms before stimulus onset and 300 ms after that (see Fig. 21A, Fig. 22A upper and lower panels for examples). The decaying part of this average artifact was fitted by an exponential function composed of three exponential terms:

$$y(t) = A * (e^{\tau_1 * t} + b * e^{\tau_2 * t} + c * e^{\tau_3 * t}) + O \quad , \quad (1)$$

with  $t$  denoting time and  $\tau_1$ ,  $\tau_2$  and  $\tau_3$  defining the decay characteristics of the three exponential terms. The amplitude parameter  $A$  scales the entire function except offset  $O$ . Parameters  $b$  and  $c$  determine the relative contribution of the exponential terms to the functions' shape.

Successful fitting of non-linear data with an iterative algorithm depends on the correct choices of the starting point ( $t=0$ ) of the average artifact, the extent of the time window used for fitting, as well as reasonable initial parameter values and their-range limitations<sup>307,308</sup>. The following subsections describe how to determine these parameters.

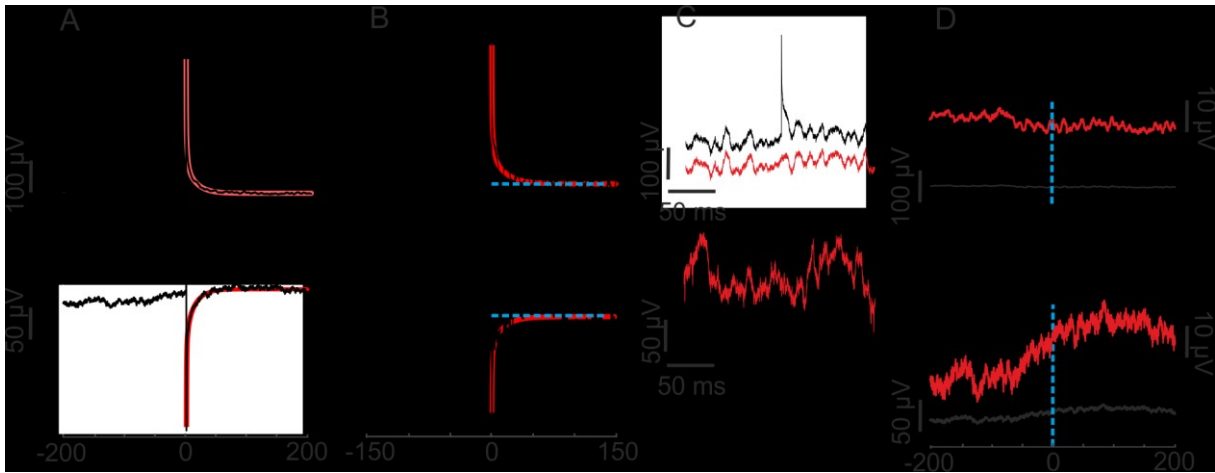


**Figure 22:** Artifact removal and signal reconstruction based on the average artifact shape. **A** The black lines show examples of average artifact shapes for two recording sessions taken from monkey I (upper panel,  $n = 234$  artifacts) and monkey II (lower panel,  $n = 110$  artifacts). The red lines depict the exponential fit based on equation (1). **B** Individual artifacts taken from the same recording sites as in A. The red curves show the exponential fit with decay parameters derived from average fit shown in A and adapted in size to the individual artifacts based on their time courses of the first 2 ms after stimulation onset. The horizontal blue dashed lines indicate the pre-stimulation values which define the offset (offset parameter  $O_i$  as in eq. (2)). Note that the offset is not subtracted from the superimposed data but is added here to the exponential fit for illustrative purposes only. **C** Lineup of the same data segments as in B, before (black) and after signal reconstruction (red). For a better visibility, curves are shown vertically offset. **D** Average over the same data as in A, but after signal reconstruction. For comparability, black graphs are scaled as in A, whereas red graphs are shown on a smaller scale. The vertical blue dashed vertical lines indicate the time of electrical stimulation.

All the following analyses and procedures were computed using custom made Matlab-scripts (v. R2016b, MathWorks, Natick, MA, USA). Curve fitting procedures for characterization of artifacts were performed using the Matlab curve-fitting toolbox (MathWorks, Natick, MA, USA).

***Starting point and period for fitting:*** We defined the starting point ( $t = 0$ , Fig 21A inset) as the time of the artifacts peak value within a short time window (here: 0.64 ms) following stimulus onset. If the artifact reached the limit of the recording system (clipping), we defined the time of the first value reaching the working range limit as the starting point. The latter is justified since the onset transient is very steep but should be adapted when other experimental setups deliver flatter onset transients resulting in later peak values.

The period of the average artifact used for fitting the above-described function (1) started at the first data point after the peak (for 25 kHz sampling rate at  $t = 0.04$  ms, Fig. 21A inset). If the average artifact shows clipping, the corresponding part of its time course is not used for in the fitting procedure. Note that in those cases in which artifacts caused clipping also the first few data points after the averaged signal returned into the working range were often distorted since some contributing individual artifacts were still clipped. Because of this observation and to avoid corresponding distortions of the fit, the period used for fitting started at 0.6 ms after stimulation onset (instead of 0.04 ms). We choose this delay of start time because none of the individual artifacts in the data-set were clipped at that time point anymore.

For determining the end of the fitting period, one has to consider the substantial differences between recovery times of signals obtained from different recordings. For example, in our test data-set, the time for a complete decay back to pre-stimulation level ranged from a few milliseconds up to 200 ms. For finding an optimal fit reflecting the later asymptotic time course of an artifact correctly, it is necessary to use a period comprising not only the decay period but also a sufficiently long period with values back on pre-stimulation level (tail, see Fig. 21B for an example). Otherwise, the curve fitting often results in functions, which do not approach this level, which in turn will induce artifacts during signal reconstruction. On the other hand, an unnecessarily long tail gains too much weight at the expense of the initial steep decay period, which also leads to a less precise fit. Thus, the optimal length of the tail depends on the size and duration of the artifact.

For these reasons, we first estimated the time at which the average artifact returned into a range of  $\pm 1\sigma$  around the pre-stimulation value, with  $\sigma$  calculated for the values of the average artifact shape within the 500 ms time window ending 1ms before stimulus onset. We defined the pre-

stimulation value as the average within the 0.5 ms window ending 0.1 ms before stimulation onset (Fig. 21A, red-colored period). The period to the point at which values decay back to  $\pm 1 \sigma$  around the pre-stimulation value comprises most but not all of the decaying part of the average artifact (Fig. 21B, red, decaying period). Therefore, we extended the period by a tail (Fig. 21B, orange-colored period). Finally, we added a subsequent anchoring period (Fig. 21B, black-colored period) in which we set all values to the pre-stimulation value. In this way, we ensured that the fitted function converges to the pre-stimulation level. The anchoring period lasted for 50 % of the duration of the decaying period and tail together, but at least 4 ms. To determine an adequate duration of the tail period we iteratively prolonged the tail period from 1 ms in 1 ms steps and calculated a fit based on equation (1) using the same starting values as described above. The iteration ended, and the corresponding tail length was selected when the goodness of fit reached 99 % ( $r^2 = 0.99$ ). If  $r^2$  did not reach 0.99 within the maximum number of iterations (for our test data 90, resulting in a max. tail length of 91 ms), the tail length resulting in the best fit was selected. Note that the addition of the anchoring period to the decaying time course results in an abrupt change in slope if the signal amplitude is not entirely back on the pre-stimulation level. This abrupt change (kink) cannot be fitted well with equation 1 and leads to low values for the goodness of fit ( $r^2 < 0.9$ ), which prevents the selection of too short periods for fitting. To avoid, that with increasing tail length the relative weight and quality of fit of the artifacts initial decaying period decreases, the sum of the weight factors used for the first 2 ms of the fitting period and the sum of all following weight factors (including tail and anchoring period) were kept equal. Figure 22 A (upper and lower panels) depicts two average artifact shapes with their respective fits (red curves).

**Amplitude parameters:** For each average artifact shape, the initial value for parameter  $A$  was estimated as the difference between the first value of the fitting period (at  $t = 0.04$  ms and  $t = 0.6$  ms in case of clipping) and the pre-stimulation value. We set initial values for scaling factors  $b$  and  $c$  to 0.1 and 0.01. The range for  $A$  is limited to the interval  $[0, \text{inf}]$  and  $[-\text{inf}, 0]$  for artifacts with positive and negative initial transient, respectively. Meaningful ranges for parameters  $b$  and  $c$  depend on the actual shape of the artifacts. In the present data set, this range was in the interval  $[0, 0.5]$ .

**Decay parameters and offset:** Initial values for the three decay parameters were set to 0.1 ( $\tau_1$ ), 0.02 ( $\tau_2$ ), and 0.01 ( $\tau_3$ ). Since both negatively and positively deflected artifacts have a strictly decaying exponential shape, we limited their range to  $[-\text{Inf}, 0]$ . The initial value for the offset variable  $O$  was the pre-stimulation value. The range of  $O$  was not limited.

### Fitting individual artifacts

Typically the artifacts evoked by a stimulation pulse with given parameters at an individual recording site have the same shape but differ in amplitude. Therefore, we fitted individual artifacts of a given recording site with a function having the same form as described in equation (1) for fitting the average artifact. In contrast to the latter case, we fixed all parameters except of the amplitude  $A_i$  and the offset  $O_i$  to the values taken from the function fitted to the average artifact. This results in in the function:

$$y(t) = A_i * (e^{\tau_1 * t} + b * e^{\tau_2 * t} + c * e^{\tau_3 * t}) + O_i, \quad (2)$$

with amplitude  $A_i$  as the only free parameter for fitting the individual stimulation artifacts. Initial value and boundaries for  $A_i$  were defined as described above for  $A$  (see *Amplitude parameters*). The offset parameter  $O_i$  was fixed to the mean value in the pre-stimulation period directly preceding the electrical stimulation onset (Fig. 22B: blue dashed line). Importantly, this fit was based only on the first 2 ms of each individual artifact (beginning at  $t=0.04$ ;  $t=0.6$  for clipped artifacts; see Fig. 21A).

### Signal reconstruction

With the individual artifacts amplitude parameter  $A_i$  and the parameters obtained from fitting the recording sites average artifact ( $b, c, \tau_1 - \tau_3$ ) the individual artifact shape was calculated over a period of 250 ms starting at  $t=0.04$  ms ( $t=0.6$  ms for clipped artifacts) using the function:

$$y(t) = A_i * (e^{\tau_1 * t} + b * e^{\tau_2 * t} + c * e^{\tau_3 * t}), \quad (3)$$

We then subtracted the result from the actual data, which removes the decaying period of the individual artifact (Fig. 22B/C). The remaining artifact onset was removed by replacing the data segment surrounding the stimulation onset and initial decaying period (between 0.12 ms before electric stimulus onset until 0.68 ms afterward) and replacing this period by linear interpolation between the last value before and the first value after the removed section, as described in Heffer and Fallon (2008)<sup>300</sup>. Also, we added to the interpolated section values of an equally sized data section (0.8 ms duration) after removing the mean of this section. The beginning of this equally sized data section was chosen randomly within the 500 ms preceding the actual electrical stimulation, but never closer than 50 ms to the stimulation. We added these fluctuations for the analysis of spiking activity, which we explain in more detail below. Figure 22 contains two exemplary average artifact shapes (Fig. 22A), as well as the average over the same data but the

artifact removed (Fig. 22D).

### **Artificial artifact generation**

For quantifying the effectiveness of our method concerning phase reconstruction, it was necessary to compare artifact removed data to non-stimulated data. For this, we generated artificial artifacts by randomly selecting 25 average artifact shapes out of a pool of 35 (monkey I: 19, monkey II: 16) and superimposed each average shape on 200 randomly selected data sections without electrical stimulation from a pool which contained 3162 data sections taken from monkey I and 1835 from monkey II. These data sections were 500 ms long, and the artifacts were superimposed randomly within the central 100 ms (200 - 300 ms). Each group of data sections containing the same average artifact shape ( $n = 200$ ) was treated as if they originate from the same recording site, and artifact removal was performed as explained above for real neuronal data.

### **Phase discrimination**

For phase estimation in the  $\gamma$ - and  $\beta$ - frequency range of the LFP, we first filtered in forward and backward direction three types of data sections: (1) data without electrical artifact, (2) the same data with an artificially superimposed artificial artifact, and (3) the same data but the artifact removed (all at 25 kHz sampling rate). We applied second-order Butterworth filters with cutoff-frequencies at 60 Hz and 120 Hz ( $\gamma$ -frequency band) and 12.5 Hz and 35 Hz ( $\beta$ -frequency band) respectively. Subsequently, we performed a Hilbert transform to estimate phases of the  $\gamma$ - and  $\beta$ - signals. The Hilbert transform thereby, delivers an estimate of the instantaneous phase  $\varphi(t)$  and amplitude  $A(t)$  at time  $t$  of the band-limited signals<sup>198,199</sup>.

### **Spiking activity**

For identifying spiking activity in the exemplary data, we used two procedures. For both the raw neuronal signal was high-pass filtered in forward and backward direction using an equiripple FIR-Filter with a pass-frequency of 300 Hz and a stop-frequency of 250 Hz. This filtering was performed for the (1) neuronal data, containing no electric stimulation, (2) the same data but with superimposed artifact (see 2.5) and (3) the artifact removed data. The first procedure required setting up a threshold, which we set at:

$$Thr = 3 * std(x) \quad (4),$$

where  $x$  denotes signal values. The second procedure determined the entire spiking activity (ESA) by taking the absolute value of the high-passed data followed by low-pass filtering with a Gaussian kernel ( $\sigma = 2$  ms, 10 ms width). For a comparison of standard spiking activity and ESA, see Drebitz et al. (2019)<sup>187</sup> and Supér and Roelfsema (2005)<sup>222</sup>. The ESA required the addition of high-frequency signal fluctuations to the interpolated section during signal reconstruction since a lack of these fluctuations would induce filter artifacts following both filter steps.

### Statistical procedures

We performed all statistical analyses using Wilcoxon signed-rank tests for comparing dependent and non-parametric samples. In the case of comparing absolute phase differences between original data, the same data with the superimposed artifact and data with this artifact removed, we corrected for multicomparison using the Bonferroni-correction. Absolute phase differences were taken at the time of the maximum median (across data sections) phase difference ( $\gamma$ -band: 0.64 ms and  $\beta$ -band: 3.8 ms after artifact onset). We calculated effect sizes based on the Wilcoxon signed-rank test by the following equation:

$$R = \frac{|Z|}{\sqrt{N}}, \quad (5)$$

with  $Z$  derived from the test statistics and  $N$ , indicating the total number of samples (here  $N = 10000$ ). Based on the literature, one can set benchmarks indicating the sizes of effects as being small, or not existing ( $R < 0.1$ ), medium ( $0.1 > R < 0.5$ ) or large ( $R > 0.5$ ). These values give only an orientation to assess the meaning of a given effect size and are benchmarks and not fix borders<sup>309,310</sup>.

### 5.1.4 Results

For characterizing the quality and reliability of artifact removal and signal reconstruction, we used data recorded in area V4 of two macaque monkeys (*Macaca mulatta*). These neuronal data contain artifacts (see Fig. 21/A; Fig. 22) due to electric stimulation with single, biphasic pulses (5.1.3 Materials and Methods, see Fig 21A for schematic illustration). We used the here described procedure to remove these artifacts offline and to reconstruct the original signals.

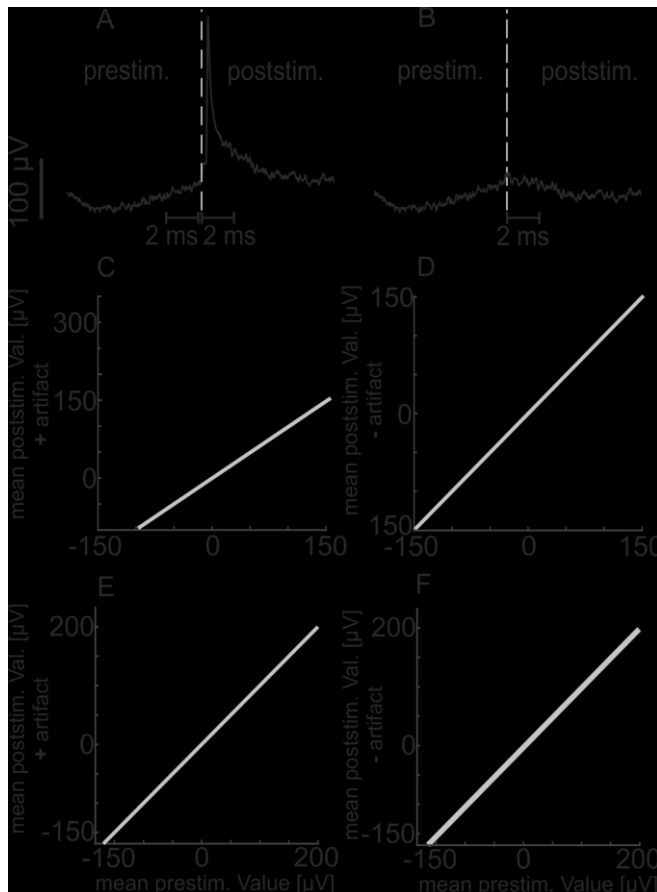


**Figure 23:** Effectiveness of artifact removal and signal reconstruction **A** Example of an individual artifact with the illustration of analysis windows for used for calculation of average pre- and post-stimulation signal levels. The windows are 2 ms wide with the prestimulation window ending 0.1 ms before stimulation onset and the post-stimulation window starting with stimulation onset (indicated by dashed vertical lines). **B** same as in A, but after artifact removal and signal reconstruction. **C** Scatterplot of the pre- and post-stimulation levels of artifacts of monkey I ( $n = 3162$ ). Note that signals in the poststim. windows still contained the artifacts. **D** same as in C but after artifact removal and signal reconstruction (affecting only post-stimulation signal levels). **E, F** same as in C, D but for monkey II ( $n = 1835$ ).

### Signal amplitude reconstruction

Due to the filter-amplifiers' broad pass-band starting at 1 Hz, the recorded signals have large low-frequency components. Therefore the signal levels immediately preceding and following the onset of the stimulation pulse are expected to be very similar if the artifact removal was successful. To test this, we computed the mean amplitude value within a two-millisecond window ending 0.1 ms before the electrical stimulus onset (Fig. 23A. prestim.) and a two-millisecond window beginning with stimulation onset (Fig 23A/B poststim.) and compared them. While the pre-stimulation level was estimated before the artifact removal, the post-stimulation level was estimated (1) for the data still containing the artifact (Fig. 23A) and (2) for the same case, but after artifact removal (Fig. 23B). To make artifact-induced deviations more visible, we rectified the values for the pre- and post-stimulation level of artifacts with a negative deflection by multiplying them by -1.

Figure 23C shows the expected strong deviation of the post-stimulus signal level from the pre-stimulation level in the direction of the stimulation artifact before artifact removal ( $n = 3162$ ; 19 recording sites of monkey I). Their values were significantly larger than the values at pre-stimulation level ( $\mu_{\text{pre}} = 2.54 \mu\text{V}$ ,  $\mu_{\text{post}} = 82.95 \mu\text{V}$ ;  $p < 10^{-20}$ ,  $Z = 48.55$ , Wilcoxon signed-rank

test). The same holds true for monkey II (Fig. 23E;  $n=1835$ , 16 recording sites) when comparing pre-stimulation to the post-stimulation level ( $\mu_{\text{pre}} = -0.54 \mu\text{V}$ ,  $\mu_{\text{post}} = 17.75 \mu\text{V}$ ;  $p < 10^{-10}$ ,  $Z = 32.12$ , Wilcoxon signed-rank test). Note, that because of averaging the signal over 2 ms, the values for the post-stimulation level are considerably smaller than the peak values of the corresponding artifacts. For both animals, the effect size of stimulation on the signal level was large (Monkey I:  $R = 0.61$ ; Monkey II:  $R = 0.53$ ).

Removing the artifacts lead to a close alignment of pre- and post-stimulation signal levels as shown by the scatter plots in Figure 23 D/F. The statistical analysis revealed that there was no significant difference between pre- and post-stimulation level after the artifact has been removed (Monkey I:  $\mu_{\text{pre}} = 2.54 \mu\text{V}$ ,  $\mu_{\text{post}} = 2.57 \mu\text{V}$ ;  $p = 0.3516$ ,  $Z = 0.93$ ; Monkey II:  $\mu_{\text{pre}} = -0.54 \mu\text{V}$ ,  $\mu_{\text{post}} = -1.08$ ,  $p = 0.0784$ ;  $Z = 1.7599$ ; Wilcoxon signed-rank test). Furthermore, effect sizes were only 0.01 and 0.03 for monkey I

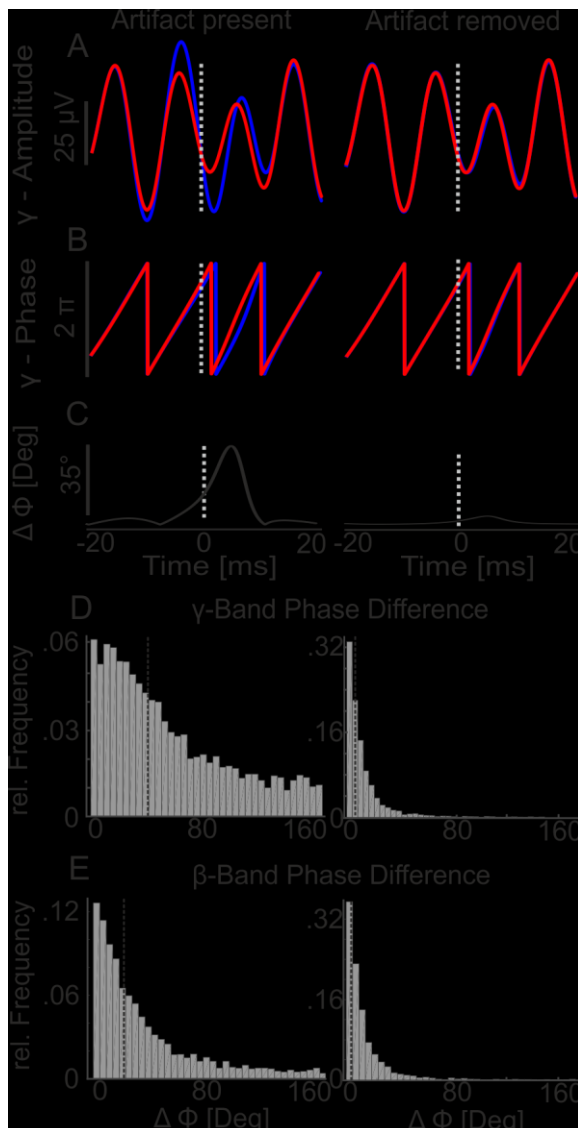


**Figure 24:** Efficacy of phase restoration. **A** The left panel shows an example LFP trace ( $\pm 20$  ms around artifact onset) without stimulation artifacts and filtered in the  $\gamma$ -frequency range (60 -120 Hz; red trace) together with the same LFP trace but affected by an artifact artificially superimposed to the raw signal before filtering (blue trace). The right panel displays the same data, but with the superimposed artifact removed from the raw trace before filtering. As a result, the blue curve for the reconstructed data is almost entirely concealed by the red original data trace. The dashed vertical lines indicate the onset of the superimposed artifact. **B** same conventions as in A, but for the time course of the instantaneous  $\gamma$ -phases of the corresponding LFP traces in A. **C** Time course of the absolute phase differences for the data shown in A and B. **D** Histogram of the maximum phase differences of all trials ( $n=5000$ ) between original data and the same data with an artifact superimposed (left panel) and the superimposed artifact removed (right panel). The values were taken at the time point of maximum average (median) phase difference across trials (0.64 ms after artifact superimposition for both panels) **E** same as in C but for the  $\beta$ -frequency band (12.5 – 35 Hz). Values were taken at 3.8 ms after the onset of the superimposed artifact for phase differences between original data and their artifact containing counterparts (left panel) and at 1.68 ms for phase differences between original data and their artifact removed counterparts (right panel).

and monkey II, respectively. Both values are considered as representing no effect anymore.

### Phase reconstruction

A sensitive measure for characterizing the time course of signals and an important measure in many investigations using LFP signals is the signal phase. Therefore, we investigated how well the phase of the original signal is reconstructed with the new method. To this end, we added each of 25 different, averaged artifacts to 200 randomly selected, artifact-free data sections of both monkeys. These superimpositions were then used for comparing the time course of signal phase between the reconstructed signal obtained after artifact removal and the original signal without superimposed artifact (for details of artificial artifact generation see 5.1.3). We performed this comparison in two frequency bands in the  $\beta$ - and the  $\gamma$ -frequency range (12.5 – 35 Hz, 60 – 120 Hz; respectively). Figure 24A shows the  $\gamma$ -frequency components of an exemplary data section before (left) and after (right) artifact removal. The red traces depict in both panels the  $\gamma$ -components of the original data, whereas the dark blue traces represent  $\gamma$ -components of the same raw data with an superimposed artifact (left) and after removal of this artifact (right). Note, that the differences between original data and artifact removed data were small (Fig. 24A right), which impedes the visibility of the dark blue trace in the right panel. For these signals, Figure 24B shows the time course of their phase. In this example, the absolute difference between original data and data with superimposed artifact reached a maximum of  $36.4^\circ$  (Fig. 24C left). After artifact removal, the deviation of the phase from its original time course did not exceed  $5.3^\circ$  (Fig. 24C right), which corresponds to a reduction of 85.4%. Note, that the absolute phase difference plots also depict an offset induced by the superimposed signal trace containing the artifact, which contains signal components within the band of interest that have not been averaged out completely (due to the limited number of trials) throughout its time course. These residual components lead to small phase shifts of the original signal components, which do not occur with real artifacts which contributes only frequency components of the artifact itself (defined by the sharp onset and exponential decay) close to the time of stimulation and no additional, persistent residues of neural signals. On average this offset was  $2.7^\circ$  in the  $\gamma$ -frequency range (median across all data sections and within a 150 ms window ending 50 ms before artifact superimposition).

The distribution of the absolute phase differences (at time of maximum average phase differences) in the  $\gamma$ -frequency range between all original data and their counterparts containing the superimposed artifacts is shown in the left panel of Figure 24D (offset corrected). The

median absolute phase difference between original and artifact-containing data at the time of maximum average phase differences is  $44.8^\circ$  (left panel, offset corrected). The same comparison between original and artifact removed data (Figure 24D right panel) revealed a median absolute phase difference of  $5.6^\circ$  (offset corrected), which corresponds to a reduction of median phase differences of 87.5 %. This reduction is highly significant ( $p < 10^{-15}$ , z-value = 55.56, Wilcoxon-signed rank test) and its effect size is large ( $R = 0.56$ ). The reduction is particularly evident when comparing the number of cases with phase differences larger than  $90^\circ$ . The superimposition of artifacts induced in 24.7 % of all data sections an absolute phase difference equal to or larger than  $90^\circ$ , whereas this is only true for 1.6 % of the artifact removed data sections.

The same pattern of results was observed in the  $\beta$ -frequency band (Fig. 24E) although with somewhat lower absolute phase differences for both, superimposed (Fig. 24E left) and artifact removed data (Fig. 24E right) when compared to their original counterparts. Again, the values are corrected for the offset ( $2.69^\circ$  in  $\beta$ -frequency band). The median absolute phase difference between original data and superimposed data was at  $23.29^\circ$  at the time of maximum phase deviation as compared to  $4.98^\circ$  (maximum) phase difference between original and artifact removed data. This difference still corresponds to a reduction of 78.63 % and was highly significant ( $p < 10^{-15}$ , z-value = 41.03, Wilcoxon signed-rank test) with a medium to large effect size ( $R = 0.41$ ).

### **Spiking activity**

Previously published approaches for artifact removal focused primarily on the restoration of the signal for reliable spike detection. While the here presented method was developed to restore the recorded signal with the focus on the signal components of the LFP, we also checked if it allows for reliable spike detection. Figure 25 depicts the high-frequency components ( $>300$  Hz) of two example sections containing spikes (Fig. 25A/B upper panels). We took these sections from periods without electrical stimulation, and hence no artifacts. The middle panels represent the same data sections but artificially superimposed with artifacts before high-pass filtering for isolating spiking activity. The first example was superimposed with a negatively deflected artifact and the second with a positively deflected one. The lower panels represent the same data sections, but the artifacts were removed before high-pass filtering. In both examples, the artifact induces an additional, large spike-like event (marked by asterisks in Fig. 25A/B, middle panel), which is lacking after artifact removal. At the same time, real spikes are

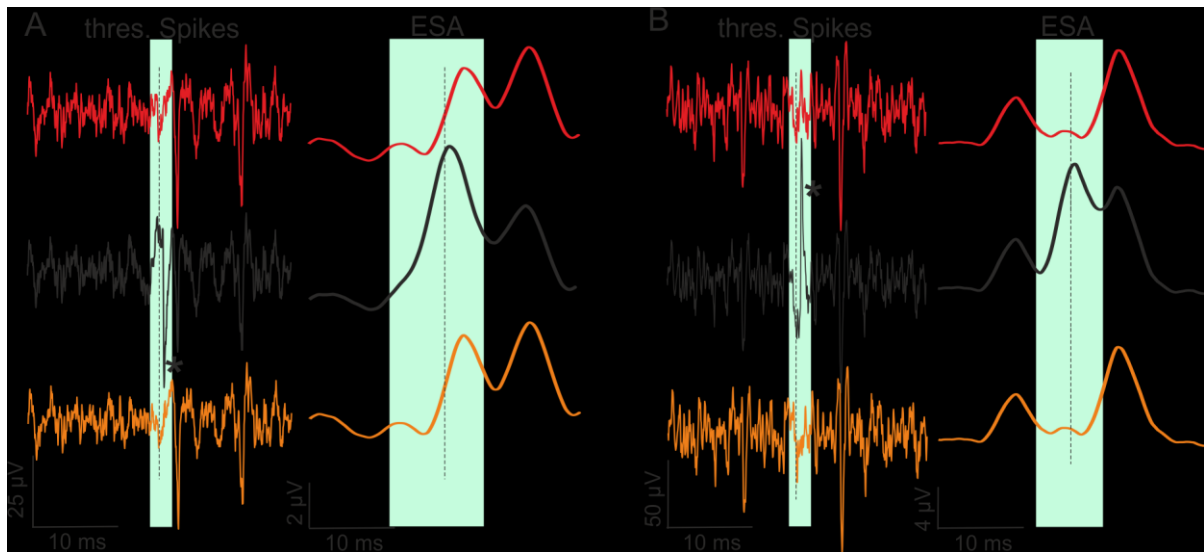


**Figure 25:** Comparison of spiking activity. *A* Example of a high-pass filtered signal trace containing two spikes (upper left panel) and the ESA for the same data section (upper right). The middle panel depicts the same data, but with an artificially superimposed (negatively deflecting) artifact in the raw signal before high-pass filtering. The orange traces in the lower panel represents the same data as used before but after removal of the artifact. *B* same conventions as for *A* but for a second example with a positively deflecting artifact. The vertical dashed lines indicate artifact onset and the green shading indicates periods where the artifact induced an additional spike (\*) and larger deviations of the ESA, which disappeared after artifact removal.

unperturbed by the artifact removal (Fig. 25A/B, lower panels).

As a second measure of spiking activity, we tested the effect of our method on the entire spiking activity (ESA). The ESA is a continuous signal instead of a point process and is more sensitive and robust in detecting spiking activity since it includes spikes from a larger part of the local population<sup>187</sup>. Furthermore, it does not require setting a threshold, which, on the other hand, makes it more vulnerable for remaining artifact components. The comparison of ESA obtained from data containing an artifact (middle panels) to the very same, original data (upper panels) shows how strongly the artifacts disturbs ESA. In contrast, the comparison of ESA computed from artifact removed data (lower panels, orange traces) to the original ESA (upper panels, red traces) exemplifies the efficiency of artifact removal even for this sensitive measure.

### 5.1.5 Discussion

The purpose of this work is to provide and characterize a new method for the removal of electrically evoked artifacts and the restoration of the entire neural signal. In contrast to established methods, this approach was developed to allow in particular for investigations of the LFP, which comprises rather slow components of neuronal activity.

For evaluation, we used real neuronal data containing artifacts that strongly disturbed the underlying neuronal signal. In a first step, we analyzed how well the method removed the artifact and restored the neural signal by comparing the signal level shortly before and after stimulation onset. The method described here, effectively reduced the highly significant and substantial effects of stimulation on the signal, such that there was no significant effect detectable anymore. As a second measure, we investigated the efficiency of phase reconstruction within the  $\gamma$ - and  $\beta$ - frequency range, in which stronger phase shifts occur than in lower frequency ranges when artifacts are artificially superimposed. These artifacts were constructed using average artifact shapes originating from actual neuronal data, such that conclusions on the effectiveness of removing these artifacts are expected to apply also to real experimental conditions in which the actual time course of the signal without artifact is unknown. We found that artifacts caused in the  $\gamma$ -frequency range a median absolute phase difference to the original data of  $45^\circ$  shortly after artifact onset. In the  $\beta$ -band, the median absolute difference was still  $25^\circ$ . After removing the artifact, these differences decreased sharply to only  $5.6^\circ$  in the  $\gamma$ -band and  $5^\circ$  in the  $\beta$ -band, corresponding to a reduction of the artifact induced absolute phase deviations by 87.5 % and 78.63 % respectively. Finally, we illustrated that similar to earlier approaches, the restored data enable reliable spike detection and ESA estimation.

Previous methods for removing electrically evoked artifacts have been developed - and are therefore very successful – for accurate spike detection. However, they have several disadvantages if the LFP is the focus of the investigation. A simple method is, for example, to cut out the period contaminated by artifact components and replace it with linear interpolation. This method has been used successfully by Heffer and Fallon (2008)<sup>300</sup> for replacing artifacts lasting on average only 170  $\mu$ s. On the other hand, the replacement of longer-lasting artifacts like those observed here and by others (e.g., Harding, 1991<sup>296</sup>; Wagenaar and Potter, 2002<sup>295</sup>) would result in a massive loss of signal components and strongly disturb the time course of the actual signal.

Another approach that is capable of removing such longer-lasting artifacts is the template subtraction. This method needs to average over a large number of stimulation artifacts to obtain a precise estimate of the actual artifact shape. Subsequently, this artifact template is subtracted from each individual stimulation period<sup>301-303</sup>. However, the inspection of our data revealed that individual artifact amplitudes sometimes differed by more than 100 % from the average. Varying artifact amplitudes have been reported in other studies as well<sup>300,305,306</sup>, indicating that this is a common characteristic. Subtraction of a template (or a fit based on the averaged artifact)

under these conditions would result in a strongly disturbed signal. It would contain residual artifact components for artifacts larger than the template and mirrored components for those that are smaller. The method presented here is capable of dealing with such substantial differences since it adapts the function to be subtracted to the amplitude of the individual artifact while keeping the characteristic shape for a given recording site constant.

A further approach capable of removing longer-lasting artifacts even when they change in amplitude across trials is based on subtracting an exponential function fitted to each stimulation artifact individually<sup>296,297</sup>. This method is well suited for studies focusing on short events such as spikes and short electrically evoked potentials (EEPs) that ride on a rather slowly decaying artifact. Since spikes and EEPs are defined on a much faster time scale than the slowly decaying part of an artifact, subtraction of a corresponding fit removes the components of the artifact but leaves fast spikes and EEPs unaffected, that do not coincide with the fast transient part of the artifact. In contrast, the LFP contains neural signal components with a time course on the same, rather slow time scale as parts of the artifact. Subtraction of a function fitting the superimposition of both the artifact and these neural signal components might result in dramatic changes of the actual LFP components. Our approach overcomes this problem in two steps. First, we use the time course of the average artifact for fitting an exponential function. This time course contains almost exclusively the components of the artifact since superimposed neural signal components were averaged out. Therefore the fitted function describes only the shape of the artifact and not components of the neural signal. Second, for the subtraction of this function from the individual artifacts, only the function's size (amplitude parameter  $A$ ) and not its shape (determined by all other parameters) is adapted when fitting this function to the individual artifact. These two steps avoid inclusion of neural signal components in the fit, which is subsequently subtracted and thereby avoid distortions of the actual signal. With the same objective, we only use the first, large part of the artifact (here the first two milliseconds) for adapting the fitted function to the individual artifacts amplitudes. Contrary to later parts of the superimposition, the artifact strongly dominates this first period and using it minimizes the impact of neural signal components on the fit, while it is sufficient for fitting its amplitude. In summary, the here presented method serves well for restoring the comparatively slow signal components as contained in the LFP.

Successful application of the method presented here requires that data and artifact fulfill a few prerequisites. First, equation (1) requires that the decay characteristic of the artifact is exponential. In previously published data<sup>296,297</sup> but also in our test data-set, an exponential fit explained the decay periods of the artifacts best. However, the method does not depend on a

specific function used for fitting and can be adapted easily if another function describes the artifact better. Second, the current method estimates the artifact duration based on the time it takes until the average neuronal signal decays back to pre-stimulation levels. This approach requires that the average of the underlying neuronal activity is flat and shows no systematic modulations (e.g., as a consequence of systematic sensory stimulation) with a fixed temporal relation to the electrical stimulus. If an artifact does not fulfill this requirement, the course of the systematic modulations can be obtained from trials without electrical stimulation and then be subtracted from the average artifact shape before fitting it with equation (1). Third, the method described here handles artifacts with changing sizes across stimulations of the same recording site successfully but requires that they have the same shape (apart from superimposed signal components). While the ability to adapt the size is necessary since we observed substantial changes across successive stimulations, we did not observe changes in the shape (decay characteristics) in our data-set. Well in line, also other studies did not report such changes, which appear unlikely since the decay characteristic of artifacts are considered to be a result of the static filter characteristics of the recording system<sup>296</sup>.

To conclude, we have shown that the method for artifact removal and signal reconstruction presented here is a powerful tool for artifact removal and signal reconstruction in data containing large and long-lasting, exponentially decaying electrical artifacts. It restores the actual time course of broadband signals, in particular, the LFP, including its phase and amplitude properties, and is at the same time capable of recovering spiking activity.

### **5.1.6 Acknowledgments**

We dearly want to thank Dr. Detlef Wegener for his valuable help and comments on this project. Furthermore, we thank Aleksandra Nadolski for the support and help with animal training and experiments. We also thank Katrin Thoß and Ramazani Hakizimana for animal care. Besides, we thank the German Research Foundation for supporting this work (DFG grants KR 1844/2-2, and KR 1844/4-1).

# General Discussion

In the following chapter, I will discuss the results of chapters 2 and 3 in more detail and provide an outlook on future experiments and research questions arising from the results presented here. The contents described in chapters 4 and 5 are not included in this general discussion since they are focused on methods to improve and enable data analysis of neuronal data under specific circumstances. The characteristics of these methods, as well as constraints and areas of application were considered in detail within the respective chapters.

## **Signal transmission between monkey areas V2 and V4 is causally dependent on gamma phase synchronization**

In chapter 2, I present the result of investigations on the causal relevance of  $\gamma$ -band synchronization for attention-dependent and selective processing of relevant information. For this, neuronal activity in area V4 was recorded while single electrical pulses to an upstream V2 population were applied. The rationale behind this study was to establish whether the impact of stimulation on neuronal activity and behavior delivers evidence in favor of or against a causal role of  $\gamma$ -synchronization for selective routing and processing.

The analyses revealed that the impact of stimulation on V4 neuronal activity but also on behavior was dependent on the current  $\gamma$ -oscillations in V4. The time in which stimulation caused significant modulations were almost identical regardless of the stimulated V2 population representing a non-attended distractor or an attended target stimulus for the individual animals. Between animals, these time points differed by around 5 -6 ms. Nevertheless, the effective phase of the V4  $\gamma$ -cycle for electrically evoked spikes to generate spikes was almost identical across animals. The highest spiking activity was caused when spikes arrived within the trough phase-period of the LFP  $\gamma$ -oscillation and lowest spiking activity for the peak phase-period, respectively.

It is widely accepted that the main contributor to the LFP is synchronized synaptic current flow, meaning that the trough of the LFP reflects the synchronous positive ion-influx at synapses into intracellular space (for a detailed review see: Buszaki et al., 2012<sup>190</sup>). From a physiological perspective, this phase of the neuronal activity cycle is the most plausible phase for incoming electrically evoked spikes to gain influence on the receiving neurons, since their membrane potential is approaching the threshold for generating spikes<sup>5,6,116,177,311</sup>.

In line with the here presented findings, other studies report a selective  $\gamma$ -synchronization

## General Discussion

between visual cortical areas representing an attended stimulus, while there was almost no  $\gamma$ -synchronization when the same stimulus was non-attended<sup>107,183,184,193</sup>. Furthermore, Ni and colleagues (2016)<sup>312</sup> showed that the strength of neuronal responses to a stimulus change depends on the ongoing  $\gamma$ -phase in V4.

Similar to our experimental design, Briggs and colleagues (2013)<sup>313</sup> used single electrical pulses to investigate the attentional modulation of synaptic efficiency between neurons located in the LGN and monosynaptically connected V1 neurons. These pulses were applied to neurons in the LGN and neuronal activity of V1 neurons recorded while the animals performed a spatial attention task. This task comprised conditions where attention was directed to or away from the recorded V1 neurons RFs. The electrical stimulation caused neurons in V1 to spike more often when attention was directed towards them. Furthermore, the temporal precision of these electrically evoked spikes was improved by attention. The authors concluded that attention increases the correlated (synchronous) synaptic activity within the receiving neuronal population to improve the processing of relevant information. However, they did not investigate whether these effects were related to the oscillatory activity in V1.

The results of  $\gamma$ -phase-dependent effects of stimulation on behavior and neuronal activity give strong evidence for a causal role of  $\gamma$ -synchronization for selective routing as proposed by the CTC-hypothesis<sup>177</sup> (chapter 1.5.3). Other theoretical approaches for explaining selective routing such as “the normalization model of attention” (chapter 1.5.1) and “balanced excitation and inhibition” (chapter 1.5.2) do not predict temporal synchronization. However, Montijn and colleagues (2012)<sup>314</sup> provided a unified concept which they named “hierarchical normalization and oscillation” that integrates the normalization model of attention and selective synchronization. This model is capable of reproducing and explaining physiological findings, which are not covered and hard to explain by the individual hypotheses alone<sup>314</sup>.

The model of balanced excitation and inhibition, neither predicts nor is it suited for an integration of  $\gamma$ -phase dependent routing. The model proposes that non-relevant inputs are filtered out based on the balance of excitatory and inhibitory inputs at those subsets of input connections representing the non-relevant information. Relevant information is gated to downstream neurons by disturbing this balance<sup>123</sup>. However, our results show that the stimulation of V2 neurons representing a non-relevant (distractor) shape affected behavior and neuronal activity in the same way as delivering pulses to a V2 population representing a relevant shape. One could argue that the electrically evoked spikes arrive as a narrow (in time) volley of spikes, which resembles transient input to the receiving neurons. The model incorporates the gating of such transient inputs, as required for bottom-up attentional mechanisms, based on the

## General Discussion

temporal disparity between excitatory and inhibitory connections. The faster excitatory connections deliver the transient inputs to the receiving neuron before the slower inhibitory connections are upregulated and restore the balance. However, this would hold for each electrically evoked volley of spikes at any time and would therefore not deliver the  $\gamma$ -phase-dependent effects we observed. Furthermore, the proposed unbalanced state for those subsets of inputs representing relevant information would allow all electrically evoked spikes originating in V2 populations representing a target shape to be effectively transmitted. However, our results show that the impact of stimulating a V2 population representing the relevant stimulus on neuronal activity in V4 and behavior was also strongly  $\gamma$ -phase-dependent.

## Outlook

Our data showed that the time neurons responded (in dependence on the V4  $\gamma$ -phase) to the incoming spikes evoked by stimulation varied between cortical layers in V4. It would be an interesting aspect for future research to perform similar experiments with multi-contact probes, which would allow simultaneous recordings across cortical layers. These probes can be used for investigating the pattern of signal flow in feedforward and feedback direction between cortical areas and would allow for layer-specific electrical stimulation. Another interesting aspect is to investigate the potential causal roles of synchronization in other frequency bands, such as in the  $\beta$ - or  $\theta$ -frequency bands. In our experimental setup, the impact of stimulation exclusively depended on the  $\gamma$ -frequency band. However, various studies reported strong correlated activity in lower frequency bands between neurons constituting feedback connections between cortical areas<sup>9,176,315–317</sup>. Primary feedback connections originate in infragranular layers of down-stream areas and avoid targeting neurons located in granular layers of the receiving up-stream areas<sup>46</sup>, indicating that the location of our recording sites in V4 (supra and granular layers) and of the stimulation sites in V2 (supragranular) was optimal for investigating feedforward but not feedback connections. The synchronization of neurons constituting the feedback connections in lower frequency bands has been attributed to the top-down control of attention<sup>318–322</sup>. The usage of multi-contact probes for recording and stimulation would allow for investigations of potential causal roles of such low-frequency oscillations for exerting top-down attention.

In line with the proposed usage of multi-contact probes for investigating how attention is mediated to upstream sensory areas, it would be beneficial to record from additional down-stream areas such as FEF or IT but also from subcortical structures. This would allow

## General Discussion

investigating whether top-down attention is mediated backward along visual areas of the visual processing pathways successively or whether attention is exerted instead in parallel on sensory areas via a subcortical relay station as, for example, the pulvinar.

### **Attention Configures Synchronization within Local Neuronal Networks for Processing of the Behaviorally Relevant Stimulus**

In chapter 3, I present the results of analyses regarding the attention dependent modulation of local neuronal networks for efficient stimulus processing. The rationale behind this was that in the scenario of competing stimuli within a pRF as described in chapter 2 and above, it is unlikely that the input selection mechanism can overcome all potentially disturbing influences of irrelevant inputs. The number of anatomical connections originating from afferent neurons representing those irrelevant inputs differs for individual neurons within the receiving population. Thus, several neurons are likely to receive a majority of afferent inputs from neurons representing irrelevant information. Therefore, the selective gating of relevant information might not be sufficient to overcome all potentially disturbing influences of irrelevant inputs. Thus, it would be beneficial to exclude from processing those neurons that are compromised by distractor related inputs.

Furthermore, it is well documented that attention modulates neuronal activity even when there is no need for selection, i.e., only one stimulus is present within an RF. Attention modulates neuronal responses for example by improving the SNR<sup>86,91,95-98,211,323</sup> and by increasing the local  $\gamma$ -synchronization<sup>102,103,324</sup>. These changes in neuronal response patterns are attributed to an improvement of stimulus representation<sup>96,119</sup>. Based on these considerations and experimental observations, we hypothesized that attention configures a local neuronal network by adjusting the pattern of functional coupling between individual neurons specifically for a given relevant stimulus. If this stimulus is accompanied by a competing stimulus, attention should exclude from processing those neurons that are compromised by the irrelevant stimulus to ensure effective processing. We furthermore assumed that attention modulates the functional coupling by changing the  $\gamma$ -synchronization between individual neurons as proposed by several theoretical models<sup>149,182,214,216,217</sup>. We tested these hypotheses by comparing the level of intra-areal  $\gamma$ -synchronization in response to a single stimulus with the level in response to the same stimulus accompanied by a distractor stimulus within the same pRF.

The results presented in chapter 3 show, that attention indeed configures the neuronal networks  $\gamma$ -synchronization specifically for the processing of a given stimulus. We found that the level

## General Discussion

of  $\gamma$ -synchronization between neurons was very similar in single stimulus conditions and conditions where this stimulus was accompanied by a distractor stimulus. The level of similarity was much higher than for the mean spiking activity of neurons. These results indicate that the pattern of  $\gamma$ -synchronization within a local neuronal network is crucial for the effective processing of relevant information. The relevance of  $\gamma$ -synchronization is further supported by the observation that the level of  $\gamma$ -synchronization preceding behavioral errors was significantly different from the level observed before correctly executed trials. In contrast, the level of multi-unit activity showed only small differences. Womeldorf et al., (2006)<sup>104</sup> showed that the level of  $\gamma$ -band power but also  $\gamma$ -band spike-field coherence is strongly correlated with the RTs of animals to a stimulus change. In trials where the recorded neuronal population represented an attended stimulus, both measures were higher in trials where monkeys reacted fast as compared to slowly executed trials. A reversed pattern was observed for conditions where the recorded population represented a non-attended stimulus. These results further support the idea of attention configuring a local neuronal network based on selective  $\gamma$ -band synchronization between individual neurons, even when there is only one stimulus present within the pRF.

We furthermore showed that pairs of neuronal populations with different stimulus preferences or weak responses to a stimulus synchronized their activity within the  $\gamma$ -frequency band if only one stimulus was presented. However, in the presence of a distractor stimulus, the strong  $\gamma$ -synchronization vanished. These pairs did not follow the general observation that the level of  $\gamma$ -synchronization is similar for conditions that require attending the same stimulus in isolation or accompanied by a distractor. This result indicates that neurons that might be compromised by non-relevant stimuli are excluded from the local processing network by desynchronizing their response patterns from the overall processing network. If the same neurons are not compromised (in single stimulus conditions), they are integrated into the processing network.

## Outlook

Thus, the question arises whether the information encoded by neurons not participating in processing the attended stimulus is lost, or if these neurons are integrated into an additional processing network engaged in processing the distractor, even if this stimulus is not attended. To address this, one could extend the experiment described in chapter 3 to additional V4 sites that represent the distractor stimulus exclusively. If neurons that receive primarily inputs of the distractor stimulus and neurons receiving their only input from the distractor form a separate processing network, they would likely synchronize their activity in the  $\gamma$ -frequency band as

## General Discussion

well. However, this pattern of synchronization should be distinct from the synchronization of the network processing the attended stimulus. This distinction could be implemented for example, by slightly different frequencies in which both neuronal processing networks synchronize. In addition, both networks could oscillate in a fixed phase offset to each other and thereby avoid generating spikes at the effective phase of the other processing network. A third potential way to keep the processing networks distinct is that both networks could alternate between periods with high and low  $\gamma$ -synchronization, i.e. only one of both processing networks is strongly  $\gamma$ -synchronized at a time.

Additionally, by comparing conditions with attention directed to one of the stimuli located in the recorded V4 RFs to conditions with attention directed to the opposite hemi field, one could investigate if and how attention prioritizes the processing of relevant information between networks encoding the attended and non-attended stimulus.

### Acknowledgments

First and foremost, I want to express my sincere gratitude to my advisor **Prof. Dr. Andreas K. Kreiter**. Without his continuous support, including the research, experiments, theoretical background, and all other vital aspects of science, this thesis would not have been possible. He helped me to improve my skills in these various fields of science and enabled me to perform the work presented here. However, it is not only the professional help and guidance of Prof. Kreiter, for which I am thankful. His style of communication, based on a partnership on eye level and a real interest in my work made me feel taken seriously and supported. I remember for example that I had severe problems finding the correct location of microelectrodes for performing the recordings required for this thesis at the very beginning of the Ph.D. Following another unsuccessful recording attempt, the two of us discussed each time for hours how to improve the approach and how to make sure the experiment runs successfully next time. However, his support was not constricted to the theoretical level only. We also spent much time each day by observing the neuronal signals, mapping potential receptive fields (which were not there), and this repeatedly over several weeks. After the automatic mapping procedure approved that we indeed found receptive fields, at the correct location within the visual cortex, ideally suited for the further experiments, we both were happy as children and patted each other on the back literally. This example is just one occasion of many happening over the years, but it does illustrate the excellent relationship and thus the pleasant working atmosphere prevailing thanks to Prof. Andreas Kreiter.

I also want to thank my second reviewer **Prof. Dr. Michael Koch** for taking the time to read and evaluate my thesis and giving his fair and helpful comments on my work. In line, I want to thank the rest of the Ph.D. committee for being part of my colloquium and enabling me to finalize my Ph.D.

In addition, I have and want to thank one of my best friends, ex-study fellow, and now also ex-colleague (**Dr.) Bastian Schledde**. We got to know each other and became friends during the master studies. From then on, our academic pathways converged. We shared our office, but also very often hotel rooms, or even a tent. Bastian was always the first person who was confronted with me being unmotivated or even disappointed with something not working out or even worse, me having problems with Matlab. Without him, I would not have the skills I have today. Especially at the very beginning of my Ph.D., I learned a lot from him regarding programming and data analysis in general. However, that is far from being all. We spend hours together talking, discussing, giving ideas and motivate each other during the years of working together. We did this while having lunch at the Mensa, being together on the squash court, or sitting in a bar while having one or two beers. Furthermore, I am pleased that we were able to work on a paper together, which crucially depended on his input, skills, and expertise. So again, thank you, Bastian!

**Dr. Detlef Wegener** is another person I want to thank sincerely. He was always available when I needed advice or wanted to talk about work or other vital topics of life. Without our evenings together enjoying the sun at the Weser River - and sometimes a few drinks, many ideas, which are part of this work, would not exist. In addition, I enjoyed working together with him, which gave me another perspective on how to organize a project and how to write a scientific paper. Furthermore, I want to thank **Dr. Iris Grothe**, **Rasmus Roese**, and **Dr. Marcus Haag** for their substantial share of my scientific development. Iris was my supervisor when I was still a master student. She introduced me to the work with animals, as well as data analysis, the theoretical background, and hypotheses concerning attention-dependent and selective information processing. Even after she left, we worked together on a paper, which she helped to improve

## Acknowledgments

actively with her knowledge and eagerness. Rasmus and Marcus were the experienced “older” Ph.D. students, which helped me to settle in the lab, to get started, animal training and many other essential aspects of the lab work. It was a pleasure to learn from and work with you!

**Lukas-Paul Rausch** started as a student working on his master project in our lab when I got to know him. In the course of his work in the lab, we closely worked together and got along very well personally, which became even better after he started his Ph.D. study. He now is an excellent friend and colleague, which I enjoy to discuss with about current or future projects during the countless Mensa lunches. I am thrilled to work with him. Without his ambitions and work ethics, this work would not be on the level it is now.

Other people I want to thank personally are **Dr. Daniel Harnack** and **Dmitriy Lisitsyn**. Both share my interest in neuroscience or better brain functions in general. We had hours of fruitful discussions/conversations about what our work is meaning, what and how it matters, and what the future might bring. Discussing work-related issues with them, may they have been of theoretical or practical nature was always helpful and inspiring.

**Aleksandra Nadolski** was responsible for me during my initial time in the lab of Prof. Kreiter in the course of my master studies. After I started my Ph.D. in the lab, she stayed at my side and gave substantial support to my work. She helped with animal training, experiments and other vital assistances. Without this support, it would not have been possible to finalize this work. Furthermore, I want to thank **Peter Bujatzek** with whom I had many inspiring discussions about improving experimental equipment with. He also helped me to assemble and improve the custom-made electrode-drives, although I remember it was not his favorite part of work, due to the small scale of components. I also want to acknowledge the work of **Katrin Thoß** and **Ramazani Hakizimana** for the caretaking of my two favorite monkey (and of course all others as well).

Without **Martin Nowak** and **Jürgen Zöllner**, the ingenious members of staff of the mechanical workshop, this thesis would be far from the point it is now. Without their professional expertise and knowledge, my abstract and sometimes unrealizable initial concepts for recording-chamber designs and other vital components used in the experiments would not have become reality.

I also want to express my special gratitude to **Janina Fisser** and **Lisa Jakobs**. Both brought me back to the ground level, when I was stressed or demotivated. It was always nice and important to hear their thoughts about my work, precisely because they are not working in a scientific environment. This helped to bring things back into perspective, which helped me to become more relaxed when something went wrong or not the way I expected.

Finally yet importantly, I also want to thank the rest of my friends, and of course, my family, for supporting me. There were times when I was frustrated or unmotivated because things went not as planned or did not work out. In those times, they were there to listen to my problems, but mostly for distracting me from work and related problems by showing me that there is another world outside the lab.

All of you made this work possible, and I am very thankful for your help!

## Bibliography

1. Helmholtz, H. von. *Treatise on Physiological Optics. Book* (Continuum, 1866). doi:10.1038/116088a0
2. von Helmholtz, H. *Handbuch der Physiologischen Optik, Dritter Abschnitt*. (Hamburg: Voss, 1911).
3. Carrasco, M., Ling, S. & Read, S. Attention alters appearance. *Nat. Neurosci.* **7**, 308–313 (2004).
4. Carrasco, M. Visual attention: the past 25 years. *Vision Res.* **51**, 1484–1525 (2011).
5. Fries, P., Nikolić, D. & Singer, W. The gamma cycle. *Trends Neurosci.* **30**, 309–316 (2007).
6. Fries, P. Neuronal gamma-band synchronization as a fundamental process in cortical computation. *Annu. Rev. Neurosci.* **32**, 209–224 (2009).
7. Simons, D. J. & Chabris, C. F. Gorillas in our midst: Sustained inattention blindness for dynamic events. *Perception* **28**, 1059–1074 (1999).
8. Van Essen, D. C., Anderson, C. H. & Felleman, D. J. Information processing in the primate visual system: an integrated systems perspective. *Science (80- )*. **255**, 419 (1992).
9. Bastos, A. M. *et al.* Visual areas exert feedforward and feedback influences through distinct frequency channels. *Neuron* **85**, 390–401 (2015).
10. Schmolesky, M. T. *et al.* Signal timing across the macaque visual system. *J. Neurophysiol.* **79**, 3272–3278 (1998).
11. Wässle, H. Parallel processing in the mammalian retina. *Nat. Rev. Neurosci.* **5**, 747–757 (2004).
12. Lee, C., Rohrer, W. H. & Sparks, D. L. Population coding of saccadic eye movements by neurons in the superior colliculus. *Nature* **332**, 357–360 (1988).
13. Sparks, D. L. Translation of sensory signals into commands for control of saccadic eye movements: role of primate superior colliculus. *Physiol. Rev.* **66**, 118–171 (1986).
14. Carpenter, M. B. & Pierson, R. J. Pretectal region and the pupillary light reflex. An anatomical analysis in the monkey. *J. Comp. Neurol.* **149**, 271–299 (1973).
15. Klein, D. C. & Moore, R. Y. *Suprachiasmatic nucleus: the mind's clock*. (Oxford University Press, USA, 1991).
16. Livingstone, M. & Hubel, D. Segregation of form, color, movement, and depth—Anatomy, physiology, and perception. *Science (80)*. **240**, 740–749 (1988).
17. Lund, J. S. Local circuit neurons of macaque monkey striate cortex: I. Neurons of laminae 4C and 5A. *J Comp Neurol* **257**, 60–92 (1997).
18. Lund, J. S. & Wu, C. Q. Local circuit neurons of macaque monkey striate cortex: IV. Neurons of laminae 1-3A. *J. Comp. Neurol.* **384**, 109–126 (1997).
19. Daw, N. W. *Visual development*. **9**, (Springer, 2006).

## Bibliography

20. Douglas, R. J. & Martin, K. A. C. Neuronal circuits of the neocortex. *Annu. Rev. Neurosci.* **27**, 419–451 (2004).
21. Douglas, R. J. & Martin, K. A. C. Mapping the matrix: the ways of neocortex. *Neuron* **56**, 226–238 (2007).
22. Shipp, S. Structure and function of the cerebral cortex. *Curr. Biol.* **17**, R443–R449 (2007).
23. Ungerleider, L. G. Two cortical visual systems. *Anal. Vis. Behav.* 549–586 (1982).
24. Mishkin, M., Ungerleider, L. G. & Macko, K. A. Object vision and spatial vision: two cortical pathways. *Trends Neurosci.* **6**, 414–417 (1983).
25. Goodale, M. A. & Milner, A. D. Separate visual pathways for perception and action. *Trends Neurosci.* **15**, 20–25 (1992).
26. Farah, M. Visual agnosia: Disorders of visual recognition and what they tell us about normal vision. (1990).
27. Freud, E., Plaut, D. C. & Behrmann, M. 'What' is happening in the dorsal visual pathway. *Trends Cogn. Sci.* **20**, 773–784 (2016).
28. Cloutman, L. L. Interaction between dorsal and ventral processing streams: where, when and how? *Brain Lang.* **127**, 251–263 (2013).
29. Ungerleider, L. G. & Haxby, J. V. 'What' and 'where' in the human brain. *Curr. Opin. Neurobiol.* **4**, 157–165 (1994).
30. Decety, J. & Grèzes, J. Neural mechanisms subserving the perception of human actions. *Trends Cogn. Sci.* **3**, 172–178 (1999).
31. Roe, A. W. *et al.* Toward a unified theory of visual area V4. *Neuron* **74**, 12–29 (2012).
32. Milner, D. & Goodale, M. *The visual brain in action*. (Oxford University Press, 2006).
33. Young, M. P. Objective analysis of the topological organization of the primate cortical visual system. *Nature* **358**, 152 (1992).
34. Weller, R. E. Two cortical visual systems in Old World and New World primates. *Prog. Brain Res.* **75**, 293–306 (1988).
35. Jeong, S. K. & Xu, Y. Behaviorally relevant abstract object identity representation in the human parietal cortex. *J. Neurosci.* **36**, 1607–1619 (2016).
36. Freud, E. *et al.* Three-dimensional representations of objects in dorsal cortex are dissociable from those in ventral cortex. *Cereb. Cortex* **27**, 422–434 (2017).
37. Hong, H., Yamins, D. L. K., Majaj, N. J. & DiCarlo, J. J. Explicit information for category-orthogonal object properties increases along the ventral stream. *Nat. Neurosci.* **19**, 613 (2016).
38. Zoccolan, D., Kouh, M., Poggio, T. & DiCarlo, J. J. Trade-off between object selectivity and tolerance in monkey inferotemporal cortex. *J. Neurosci.* **27**, 12292–12307 (2007).
39. Schroeder, C. E., Mehta, A. D. & Givre, S. J. A spatiotemporal profile of visual system activation revealed by current source density analysis in the awake macaque. *Cereb. cortex (New York, NY 1991)* **8**, 575–592 (1998).
40. Chen, C.-M. *et al.* Functional anatomy and interaction of fast and slow visual pathways

## Bibliography

- in macaque monkeys. *Cereb. Cortex* **17**, 1561–1569 (2006).
41. Maunsell, J. H. & van Essen, D. C. The connections of the middle temporal visual area (MT) and their relationship to a cortical hierarchy in the macaque monkey. *J. Neurosci.* **3**, 2563–2586 (1983).
  42. Shipp, S. & Zeki, S. The organization of connections between areas V5 and V1 in macaque monkey visual cortex. *Eur. J. Neurosci.* **1**, 309–332 (1989).
  43. Ungerleider, L. G. & Desimone, R. Cortical connections of visual area MT in the macaque. *J. Comp. Neurol.* **248**, 190–222 (1986).
  44. Zeki, S. & Shipp, S. The functional logic of cortical connections. *Nature* **335**, 311 (1988).
  45. Wilson, H. R. & Wilkinson, F. From orientations to objects: Configural processing in the ventral stream. *J. Vis.* **15**, 4 (2015).
  46. Felleman, D. J. & Van Essen, D. C. Distributed hierarchical processing in the primate cerebral cortex. *Cereb. cortex* **1**, 1–47 (1991).
  47. Kravitz, D. J., Saleem, K. S., Baker, C. I., Ungerleider, L. G. & Mishkin, M. Processing of Object Quality. **17**, 26–49 (2014).
  48. Brincat, S. L. & Connor, C. E. Underlying principles of visual shape selectivity in posterior inferotemporal cortex. *Nat. Neurosci.* **7**, 880–886 (2004).
  49. Rousselet, G. A., Thorpe, S. J. & Fabre-Thorpe, M. How parallel is visual processing in the ventral pathway? *Trends Cogn. Sci.* **8**, 363–370 (2004).
  50. Yau, J. M., Pasupathy, A., Brincat, S. L. & Connor, C. E. Curvature processing dynamics in macaque area V4. *Cereb. Cortex* bhs004 (2012).
  51. DeYoe, E. A. & Van Essen, D. C. Concurrent processing streams in monkey visual cortex. *Trends Neurosci.* **11**, 219–226 (1988).
  52. Nassi, J. J. & Callaway, E. M. Parallel processing strategies of the primate visual system. *Nat. Rev. Neurosci.* **10**, 360 (2009).
  53. Gattass, R. *et al.* Cortical visual areas in monkeys: location, topography, connections, columns, plasticity and cortical dynamics. *Philos. Trans. R. Soc. B Biol. Sci.* **360**, 709–731 (2005).
  54. Moran, J. & Desimone, R. Selective attention gates visual processing in the extrastriate cortex. *Science* **229**, 782–784 (1985).
  55. Marois, R. & Ivanoff, J. Capacity limits of information processing in the brain. *Trends Cogn. Sci.* **9**, 296–305 (2005).
  56. Franconeri, S. L., Jonathan, S. V & Scimeca, J. M. Tracking multiple objects is limited only by object spacing, not by speed, time, or capacity. *Psychol. Sci.* **21**, 920–925 (2010).
  57. Bao, P. & Tsao, D. Y. Representation of multiple objects in macaque category-selective areas. *Nat. Commun.* **9**, 1774 (2018).
  58. James, W. *The Principles of Psychology*. **2**, (Holt, 1890).
  59. Reynolds, W. M. & Miller, G. E. Current perspectives in educational psychology. *Handb. Psychol.* 1–20 (2003).

## Bibliography

60. Von Helmholtz, H. *Handbuch der physiologischen Optik*. **9**, (Voss, 1867).
61. Tsotsos, J. K. *A computational perspective on visual attention*. (MIT Press, 2011).
62. Awh, E., Belopolsky, A. V. & Theeuwes, J. Top-down versus bottom-up attentional control: A failed theoretical dichotomy. *Trends Cogn. Sci.* **16**, 437–443 (2012).
63. Eriksen, C. W. & Hoffman, J. E. Temporal and spatial characteristics of selective encoding from visual displays. *Attention, Perception, Psychophys.* **12**, 201–204 (1972).
64. Posner, M. I., Petersen, S. E., Fox, P. T. & Raichle, M. E. Localization of cognitive operations in the human brain. *Science (80-. )*. **240**, 1627 (1988).
65. Posner, M. I. Orienting of attention. *Q. J. Exp. Psychol.* **32**, 3–25 (1980).
66. Moore, C. M. & Egeth, H. How does feature-based attention affect visual processing? *J. Exp. Psychol. Hum. Percept. Perform.* **24**, 1296 (1998).
67. Melcher, D., Papathomas, T. V & Vidnyánszky, Z. Implicit attentional selection of bound visual features. *Neuron* **46**, 723–729 (2005).
68. Kanai, R., Tsuchiya, N. & Verstraten, F. A. J. The scope and limits of top-down attention in unconscious visual processing. *Curr. Biol.* **16**, 2332–2336 (2006).
69. Duncan, J. Selective attention and the organization of visual information. *J. Exp. Psychol. Gen.* **113**, 501 (1984).
70. Valdes-Sosa, M., Cobo, A. & Pinilla, T. Transparent motion and object-based attention. *Cognition* **66**, B13–B23 (1998).
71. Lavie, N. & Driver, J. On the spatial extent of attention in object-based visual selection. *Percept. Psychophys.* **58**, 1238–1251 (1996).
72. Hillstrom, A. P. Repetition effects in visual search. *Attention, Perception, Psychophys.* **62**, 800–817 (2000).
73. Kristjánsson, A., Wang, D. & Nakayama, K. The role of priming in conjunctive visual search. *Cognition* **85**, 37–52 (2002).
74. Maljkovic, V. & Nakayama, K. Priming of pop-out: II. The role of position. *Attention, Perception, Psychophys.* **58**, 977–991 (1996).
75. Wang, D., Kristjánsson, A. & Nakayama, K. Efficient visual search without top-down or bottom-up guidance: A putative role for perceptual organization. *Cogn. Sci. Tech. Rep* (2001).
76. Theeuwes, J. & Van der Burg, E. On the limits of top-down control of visual selection. *Attention, Perception, Psychophys.* **73**, 2092 (2011).
77. Hickey, C., Chelazzi, L. & Theeuwes, J. Reward changes salience in human vision via the anterior cingulate. *J. Neurosci.* **30**, 11096–11103 (2010).
78. Anderson, B. A., Laurent, P. A. & Yantis, S. Learned value magnifies salience-based attentional capture. *PLoS One* **6**, e27926 (2011).
79. Anderson, B. A., Laurent, P. A. & Yantis, S. Value-driven attentional capture. *Proc. Natl. Acad. Sci.* **108**, 10367–10371 (2011).
80. Treisman, A. M. & Gelade, G. A feature-integration theory of attention. *Cogn. Psychol.*

## Bibliography

- 12, 97–136 (1980).
81. Duncan, J. & Humphreys, G. W. Visual search and stimulus similarity. *Psychol. Rev.* **96**, 433 (1989).
  82. Nothdurft, H.-C. The role of features in preattentive vision: Comparison of orientation, motion and color cues. *Vision Res.* **33**, 1937–1958 (1993).
  83. Holmgren, J. E., Juola, J. F. & Atkinson, R. C. Response latency in visual search with redundancy in the visual display. *Percept. Psychophys.* **16**, 123–128 (1974).
  84. Estes, W. K. & Wessel, D. L. Reaction time in relation to display size and correctness of response in forced-choice visual signal detection. *Percept. Psychophys.* **1**, 369–373 (1966).
  85. Yantis, S. & Jonides, J. Abrupt visual onsets and selective attention: evidence from visual search. *J. Exp. Psychol. Hum. Percept. Perform.* **10**, 601 (1984).
  86. Schledde, B., Galashan, F. O., Przybyla, M., Kreiter, A. K. & Wegener, D. Task-specific, dimension-based attentional shaping of motion processing in monkey area MT. *J. Neurophysiol.* **118**, 1542–1555 (2017).
  87. Motter, B. C. Focal attention produces spatially selective processing in visual cortical areas V1, V2, and V4 in the presence of competing stimuli. *J. Neurophysiol.* **70**, 909–919 (1993).
  88. Roelfsema, P. R., Lamme, V. A. & Spekreijse, H. Object-based attention in the primary visual cortex of the macaque monkey. *Nature* **395**, 376–81 (1998).
  89. Ito, M. & Gilbert, C. D. Attention modulates contextual influences in the primary visual cortex of alert monkeys. *Neuron* **22**, 593–604 (1999).
  90. Luck, S. J., Chelazzi, L., Hillyard, S. A. & Desimone, R. Neural mechanisms of spatial selective attention in areas V1, V2, and V4 of macaque visual cortex. *J. Neurophysiol.* **77**, 24–42 (1997).
  91. Treue, S. & Maunsell, J. H. Attentional modulation of visual motion processing in cortical areas MT and MST. *Nature* **382**, 539–541 (1996).
  92. Yantis, S. & Serences, J. T. Cortical mechanisms of space-based and object-based attentional control. *Curr. Opin. Neurobiol.* **13**, 187–193 (2003).
  93. Tolhurst, D. J., Movshon, J. A. & Dean, A. F. The statistical reliability of signals in single neurons in cat and monkey visual cortex. *Vision Res.* **23**, 775–785 (1983).
  94. McAdams, C. J. & Maunsell, J. H. R. Effects of attention on the reliability of individual neurons in monkey visual cortex. *Neuron* **23**, 765–773 (1999).
  95. Mitchell, J. F., Sundberg, K. A. & Reynolds, J. H. Differential attention-dependent response modulation across cell classes in macaque visual area V4. *Neuron* **55**, 131–141 (2007).
  96. Mitchell, J. F., Sundberg, K. A. & Reynolds, J. H. Spatial attention decorrelates intrinsic activity fluctuations in macaque area V4. *Neuron* **63**, 879–888 (2009).
  97. Galashan, F. O., Saßen, H. C., Kreiter, A. K. & Wegener, D. Monkey area MT latencies to speed changes depend on attention and correlate with behavioral reaction times. *Neuron* **78**, 740–750 (2013).

## Bibliography

98. Cohen, M. R. & Maunsell, J. H. R. Attention improves performance primarily by reducing interneuronal correlations. *Nat. Neurosci.* **12**, 1594–1600 (2009).
99. Abbott, L. F. & Dayan, P. The effect of correlated variability on the accuracy of a population code. *Neural Comput.* **11**, 91–101 (1999).
100. Averbeck, B. B., Latham, P. E. & Pouget, A. Neural correlations, population coding and computation. *Nat. Rev. Neurosci.* **7**, 358–366 (2006).
101. Murthy, V. N. & Fetz, E. E. Oscillatory activity in sensorimotor cortex of awake monkeys: synchronization of local field potentials and relation to behavior. *J. Neurophysiol.* **76**, 3949–3967 (1996).
102. Fries, P., Reynolds, J. H., Rorie, A. E. & Desimone, R. Modulation of oscillatory neuronal synchronization by selective visual attention. *Science* **291**, 1560–3 (2001).
103. Taylor, K., Mandon, S., Freiwald, W. A. & Kreiter, A. K. Coherent oscillatory activity in monkey area v4 predicts successful allocation of attention. *Cereb. Cortex* **15**, 1424–1437 (2005).
104. Womelsdorf, T., Fries, P., Mitra, P. P. & Desimone, R. Gamma-band synchronization in visual cortex predicts speed of change detection. *Nature* **439**, 733–736 (2006).
105. Bichot, N. P., Rossi, A. F. & Desimone, R. Parallel and serial neural mechanisms for visual search in macaque area V4. *Science (80-. )*. **308**, 529–534 (2005).
106. Tallon-Baudry, C., Bertrand, O., Hénaff, M.-A., Isnard, J. & Fischer, C. Attention modulates gamma-band oscillations differently in the human lateral occipital cortex and fusiform gyrus. *Cereb. cortex* **15**, 654–662 (2004).
107. Gregoriou, G. G., Gotts, S. J., Zhou, H. & Desimone, R. High-frequency, long-range coupling between prefrontal and visual cortex during attention. *Science (80-. )*. **324**, 1207–1210 (2009).
108. Chalk, M. *et al.* Attention reduces stimulus-driven gamma frequency oscillations and spike field coherence in V1. *Neuron* **66**, 114–125 (2010).
109. Crick, F. & Koch, C. Some reflections on visual awareness. in *Cold Spring Harbor symposia on quantitative biology* **55**, 953–962 (Cold Spring Harbor Laboratory Press, 1990).
110. Niebur, E., Koch, C. & Rosin, C. An oscillation-based model for the neuronal basis of attention. *Vision Res.* **33**, 2789–2802 (1993).
111. Niebur, E. & Koch, C. A model for the neuronal implementation of selective visual attention based on temporal correlation among neurons. *J. Comput. Neurosci.* **1**, 141–158 (1994).
112. Azouz, R. & Gray, C. M. Adaptive coincidence detection and dynamic gain control in visual cortical neurons in vivo. *Neuron* **37**, 513–523 (2003).
113. Reynolds, J. H., Chelazzi, L. & Desimone, R. Competitive mechanisms subserve attention in macaque areas V2 and V4. *J. Neurosci.* **19**, 1736–1753 (1999).
114. Reynolds, J. H. & Desimone, R. Interacting roles of attention and visual salience in V4. *Neuron* **37**, 853–863 (2003).
115. Lee, J. & Maunsell, J. H. R. Attentional modulation of MT neurons with single or multiple stimuli in their receptive fields. *J. Neurosci.* **30**, 3058–3066 (2010).

## Bibliography

116. Kreiter, A. K. How do we model attention-dependent signal routing? *Neural Netw.* **19**, 1443–1444 (2006).
117. Desimone, R. & Duncan, J. Neural mechanisms of selective visual attention. *Annu. Rev. Neurosci.* **18**, 193–222 (1995).
118. Grothe, I. *et al.* Attention selectively gates afferent signal transmission to area V4. *J. Neurosci.* **38**, 3441–3452 (2018).
119. Moore, T. & Zirnsak, M. Neural mechanisms of selective visual attention. *Annu. Rev. Psychol.* **68**, 47–72 (2017).
120. Lee, J. & Maunsell, J. H. R. A normalization model of attentional modulation of single unit responses. *PLoS One* **4**, e4651 (2009).
121. Reynolds, J. H. & Heeger, D. J. The Normalization Model of Attention. *Neuron* **61**, 168–185 (2009).
122. Heeger, D. J. Normalization of cell responses in cat striate cortex. *Vis. Neurosci.* **9**, 181–197 (1992).
123. Vogels, T. P. & Abbott, L. F. Gating multiple signals through detailed balance of excitation and inhibition in spiking networks. *Nat. Neurosci.* **12**, 483–491 (2009).
124. Abeles, M. Role of the cortical neuron: integrator or coincidence detector? *Isr. J. Med. Sci.* **18**, 83–92 (1982).
125. Abeles, M., Bergman, H., Margalit, E. & Vaadia, E. Spatiotemporal firing patterns in the frontal cortex of behaving monkeys. *J. Neurophysiol.* **70**, 1629–1638 (1993).
126. Diesmann, M., Gewaltig, M.-O. & Aertsen, A. Stable propagation of synchronous spiking in cortical neural networks. *Nature* **402**, 529–533 (1999).
127. Kumar, A., Rotter, S. & Aertsen, A. Conditions for propagating synchronous spiking and asynchronous firing rates in a cortical network model. *J. Neurosci.* **28**, 5268–5280 (2008).
128. Shu, Y., Hasenstaub, A. & McCormick, D. A. Turning on and off recurrent balanced cortical activity. *Nature* **423**, 288–293 (2003).
129. Haider, B., Duque, A., Hasenstaub, A. R. & McCormick, D. A. Neocortical network activity in vivo is generated through a dynamic balance of excitation and inhibition. *J. Neurosci.* **26**, 4535–4545 (2006).
130. Shadlen, M. N. & Newsome, W. T. Noise, neural codes and cortical organization. *Curr. Opin. Neurobiol.* **4**, 569–579 (1994).
131. Troyer, T. W. & Miller, K. D. Physiological gain leads to high ISI variability in a simple model of a cortical regular spiking cell. *Neural Comput.* **9**, 971–983 (1997).
132. Perkel, D. H. *Detection of Functional Interactions Among Neurons: A Technique Using Repetitive Presentations of Stimuli.* (Rand Corporation, 1964).
133. Segundo, J. P., Perkel, D. H. & Moore, G. P. Spike probability in neurones: influence of temporal structure in the train of synaptic events. *Biol. Cybern.* **3**, 67–82 (1966).
134. Perkel, D. H., Gerstein, G. L. & Moore, G. P. Neuronal spike trains and stochastic point processes: II. Simultaneous spike trains. *Biophys. J.* **7**, 419–440 (1967).
135. Gerstein, G. L. & Perkel, D. H. Mutual temporal relationships among neuronal spike

## Bibliography

- trains: statistical techniques for display and analysis. *Biophys. J.* **12**, 453–473 (1972).
136. Toyama, K., Kimura, M. & Tanaka, K. Cross-correlation analysis of interneuronal connectivity in cat visual cortex. *J Neurophysiol* **46**, 191–201 (1981).
  137. Michalski, A., Gerstein, G. L., Czarkowska, J. & Tarnecki, R. Interactions between cat striate cortex neurons. *Exp. Brain Res.* **51**, 97–107 (1983).
  138. Gray, C. M. & Singer, W. Stimulus-specific neuronal oscillations in orientation columns of cat visual cortex. *Proc. Natl. Acad. Sci.* **86**, 1698–1702 (1989).
  139. Schwarz, C. & Bolz, J. Functional specificity of a long-range horizontal connection in cat visual cortex: a cross-correlation study. *J. Neurosci.* **11**, 2995–3007 (1991).
  140. Ts'o, D. Y. & Gilbert, C. D. The organization of chromatic and spatial interactions in the primate striate cortex. *J. Neurosci.* **8**, 1712–1727 (1988).
  141. Kruger, J. & Aiple, F. Multimicroelectrode investigation of monkey striate cortex: spike train correlations in the infragranular layers. *J. Neurophysiol.* **60**, 798–828 (1988).
  142. Espinosa, I. E. & Gerstein, G. L. Cortical auditory neuron interactions during presentation of 3-tone sequences: effective connectivity. *Brain Res.* **450**, 39–50 (1988).
  143. Aertsen, A. M., Gerstein, G. L., Habib, M. K. & Palm, G. Dynamics of neuronal firing correlation: modulation of "effective connectivity". *J. Neurophysiol.* **61**, 900–917 (1989).
  144. von der Malsburg, C. Pattern recognition by labeled graph matching. *Neural networks* **1**, 141–148 (1988).
  145. Barlow, H. B. Single units and sensation: a neuron doctrine for perceptual psychology? *Perception* **1**, 371–394 (1972).
  146. Sakurai, Y. Population coding by cell assemblies—what it really is in the brain. *Neurosci. Res.* **26**, 1–16 (1996).
  147. Palm, G. Neural assemblies-studies of brain functions. (1982).
  148. Von Der Malsburg, C. Nervous structures with dynamical links. *Berichte der Bunsengesellschaft für Phys. Chemie* **89**, 703–710 (1985).
  149. Aertsen, A. M., Gerstein, G. L., Habib, M. K. & Palm, G. Dynamics of neuronal firing correlation: modulation of 'effective connectivity'. *J. Neurophysiol.* **61**, 900–917 (1989).
  150. Palm, G. Cell assemblies as a guideline for brain research. *Concepts Neurosci.* **1**, 133–147 (1990).
  151. Hebb, D. O. *The organization of behavior: A neuropsychological approach.* (John Wiley & Sons, 1949).
  152. Braitenberg, V. Cell assemblies in the cerebral cortex. in *Theoretical approaches to complex systems* 171–188 (Springer, 1978).
  153. Edelman, G. M. & Mountcastle, V. B. *The mindful brain: Cortical organization and the group-selective theory of higher brain function.* (Massachusetts Inst of Technology Pr, 1978).
  154. Grossberg, S. How does a brain build a cognitive code? *Psychol. Rev.* **87**, 1 (1980).

## Bibliography

155. Singer, W. Activity-dependent self-organization of the mammalian visual cortex. (1985).
156. Edelman, G. M. *Neural Darwinism: The theory of neuronal group selection*. (Basic books, 1987).
157. Gray, C. M. & Singer, W. Stimulus-dependent neuronal oscillations in the cat visual cortex area 17. *Neurosci.* **22**, 434 (1987).
158. Eckhorn, R. *et al.* Coherent oscillations: A mechanism of feature linking in the visual cortex? *Biol. Cybern.* **60**, 121–130 (1988).
159. Gray, C. M., König, P., Engel, A. K. & Singer, W. Oscillatory responses in cat visual cortex exhibit inter-columnar synchronization which reflects global stimulus properties. *Nature* **338**, 334–337 (1989).
160. Engel, A. K., Koenig, P., Gray, C. M. & Singer, W. Synchronization of oscillatory responses: A mechanism for stimulus-dependent assembly formation in cat visual cortex. *Parallel Process. neural Syst. Comput.* 105–108 (1990).
161. Engel, A. K., Kreiter, A. K., König, P. & Singer, W. Synchronization of oscillatory neuronal responses between striate and extrastriate visual cortical areas of the cat. *Proc. Natl. Acad. Sci.* **88**, 6048–6052 (1991).
162. Milner, P. M. A model for visual shape recognition. *Psychol. Rev.* **81**, 521 (1974).
163. von der Malsburg, C. & Willshaw, D. Co-operativity and brain organization. *Trends Neurosci.* **4**, 80–83 (1981).
164. Kreiter, A. K. & Singer, W. Stimulus dependent synchronization of neuronal responses in the visual cortex of awake macaque monkeys. --->published as Keiter96b <--- **16**, 2381–2396 (1996).
165. De Oliveira, S. C., Thiele, A. & Hoffmann, K.-P. Synchronization of neuronal activity during stimulus expectation in a direction discrimination task. *J. Neurosci.* **17**, 9248–9260 (1997).
166. Thiele, A. & Stoner, G. Neuronal synchrony does not correlate with motion coherence in cortical area MT. *Nature* **421**, 366 (2003).
167. Dong, Y., Mihalas, S., Qiu, F., von der Heydt, R. & Niebur, E. Synchrony and the binding problem in macaque visual cortex. *J. Vis.* **8**, 30 (2008).
168. Roelfsema, P. R., Lamme, V. A. F. & Spekreijse, H. Synchrony and covariation of firing rates in the primary visual cortex during contour grouping. *Nat. Neurosci.* **7**, 982 (2004).
169. Lima, B., Singer, W., Chen, N.-H. & Neuenschwander, S. Synchronization dynamics in response to plaid stimuli in monkey V1. *Cereb. cortex* **20**, 1556–1573 (2009).
170. Gieselmann, M. A. & Thiele, A. Comparison of spatial integration and surround suppression characteristics in spiking activity and the local field potential in macaque V1. *Eur. J. Neurosci.* **28**, 447–459 (2008).
171. Jia, X., Xing, D. & Kohn, A. No consistent relationship between gamma power and peak frequency in macaque primary visual cortex. *J. Neurosci.* **33**, 17–25 (2013).
172. Merker, B. Cortical gamma oscillations: the functional key is activation, not cognition. *Neurosci. Biobehav. Rev.* **37**, 401–417 (2013).

## Bibliography

173. Bosman, C. A., Lansink, C. S. & Pennartz, C. M. A. Functions of gamma-band synchronization in cognition: From single circuits to functional diversity across cortical and subcortical systems. *Eur. J. Neurosci.* **39**, 1982–1999 (2014).
174. Roelfsema, P. R., Engel, A. K. & Singer, W. Visuomotor integration is associated with zero time-lag synchronization among cortical areas. *Nature* **385**, 157 (1997).
175. Steinmetz, P. N. *et al.* Attention modulates synchronized neuronal firing in primate somatosensory cortex. *Nature* **404**, 187 (2000).
176. Buffalo, E. A., Fries, P., Landman, R., Buschman, T. J. & Desimone, R. Laminar differences in gamma and alpha coherence in the ventral stream. *Proc. Natl. Acad. Sci.* **108**, 11262–11267 (2011).
177. Fries, P. A mechanism for cognitive dynamics: neuronal communication through neuronal coherence. *Trends Cogn. Sci.* **9**, 474–480 (2005).
178. Womelsdorf, T. *et al.* Modulation of neuronal interactions through neuronal synchronization. *Science (80-. )*. **316**, 1609–1612 (2007).
179. Börgers, C. & Kopell, N. J. Gamma oscillations and stimulus selection. *Neural Comput.* **20**, 383–414 (2008).
180. Akam, T. & Kullmann, D. M. Oscillations and filtering networks support flexible routing of information. *Neuron* **67**, 308–320 (2010).
181. Buehlmann, A. & Deco, G. Optimal information transfer in the cortex through synchronization. *PLoS Comput. Biol.* **6**, e1000934 (2010).
182. Tiesinga, P. H. & Sejnowski, T. J. Mechanisms for phase shifting in cortical networks and their role in communication through coherence. *Front Hum Neurosci* **4**, 196 (2010).
183. Grothe, I., Neitzel, S. D., Mandon, S. & Kreiter, A. K. Switching neuronal inputs by differential modulations of gamma-band phase-coherence. *J. Neurosci.* **32**, 16172–80 (2012).
184. Bosman, C. *et al.* Attentional stimulus selection through selective synchronization between monkey visual areas. *Neuron* **75**, 875–888 (2012).
185. Drebitz, E., Haag, M., Grothe, I., Mandon, S. & Kreiter, A. K. Attention configures synchronization within local neuronal networks for processing of the behaviorally relevant stimulus. *Front. Neural Circuits* **12**, 71 (2018).
186. Treue, S. & Martínez Trujillo, J. C. Feature-based attention influences motion processing gain in macaque visual cortex. *Nature* **399**, 575–579 (1999).
187. Drebitz, E., Schledde, B., Kreiter, A. K. & Wegener, D. Optimizing the Yield of Multi-Unit Activity by Including the Entire Spiking Activity. *Front. Neurosci.* **13**, 83 (2019).
188. Self, M. W., van Kerkoerle, T., Supèr, H. & Roelfsema, P. R. Distinct roles of the cortical layers of area V1 in figure-ground segregation. *Curr. Biol.* **23**, 2121–2129 (2013).
189. Mason, A., Nicoll, A. & Stratford, K. Synaptic transmission between individual pyramidal neurons of the rat visual cortex in vitro. *J. Neurosci.* **11**, 72–84 (1991).
190. Buzsáki, G., Anastassiou, C. A. & Koch, C. The origin of extracellular fields and currents — EEG, ECoG, LFP and spikes. *Nat. Rev. Neurosci.* **13**, 407–420 (2012).

## Bibliography

191. Okun, M., Naim, A. & Lampl, I. The Subthreshold Relation between Cortical Local Field Potential and Neuronal Firing Unveiled by Intracellular Recordings in Awake Rats. *J. Neurosci.* **30**, 4440–4448 (2010).
192. Rohenkohl, G., Bosman, C. A. & Fries, P. Gamma synchronization between V1 and V4 improves behavioral performance. *Neuron* **100**, 953–963 (2018).
193. Gregoriou, G. G., Gotts, S. J. & Desimone, R. Cell-type-specific synchronization of neural activity in FEF with V4 during attention. *Neuron* **73**, 581–594 (2012).
194. Doesburg, S. M., Roggeveen, A. B., Kitajo, K. & Ward, L. M. Large-scale gamma-band phase synchronization and selective attention. *Cereb. cortex* **18**, 386–396 (2007).
195. Doesburg, S. M., Green, J. J., McDonald, J. J. & Ward, L. M. Theta modulation of inter-regional gamma synchronization during auditory attention control. *Brain Res.* **1431**, 77–85 (2012).
196. Van Kerkoerle, T., Self, M. W. & Roelfsema, P. R. Layer-specificity in the effects of attention and working memory on activity in primary visual cortex. *Nat. Commun.* **8**, 13804 (2017).
197. Nandy, A. S., Nassi, J. J. & Reynolds, J. H. Laminar organization of attentional modulation in macaque visual area V4. *Neuron* **93**, 235–246 (2017).
198. Le Van Quyen, M. *et al.* Comparison of Hilbert transform and wavelet methods for the analysis of neuronal synchrony. *J. Neurosci. Methods* **111**, 83–98 (2001).
199. Rosenblum, M., Pikovsky, A., Kurths, J., Schäfer, C. & Tass, P. A. Phase synchronization: from theory to data analysis. in *Handbook of biological physics* **4**, 279–321 (Elsevier, 2001).
200. Nichols, T. E. & Holmes, A. P. Nonparametric permutation tests for functional neuroimaging: a primer with examples. *Hum. Brain Mapp.* **15**, 1–25 (2002).
201. Spath, H. *The cluster dissection and analysis theory fortran programs examples.* (Prentice-Hall, Inc., 1985).
202. Seber, G. A. F. *Multivariate observations* John Wiley & sons. *New York* (1984).
203. Gilbert, C. D. & Sigman, M. Brain states: top-down influences in sensory processing. *Neuron* **54**, 677–696 (2007).
204. Carandini, M. & Heeger, D. J. D. Normalization as a canonical neural computation. *Nat. Rev. Neurosci.* **13**, 51–62 (2012).
205. Park, H. J. & Friston, K. J. Structural and functional brain networks: from connections to cognition. *Science* **342**, 1238411 (2013).
206. Battaglia, D. *et al.* Dynamic effective connectivity and information routing in inter-areal brain circuits. *PLoS Comput Biol* **8**, e1002438 (2012).
207. Wildie, M. Establishing communication between neuronal populations through competitive entrainment. *Front. Comput. Neurosci.* **5**, 1–16 (2012).
208. Hahn, G., Bujan, A. F., Frégnac, Y., Aertsen, A. & Kumar, A. Communication through resonance in spiking neuronal networks. *PLoS Comput. Biol.* **10**, e1003811 (2014).
209. Harnack, D., Ernst, U. A. & Pawelzik, K. R. A model for attentional information routing through coherence predicts biased competition and multistable perception. *J.*

## Bibliography

- Neurophysiol.* **114**, 1593–1605 (2015).
210. Palmigiano, A., Geisel, T., Wolf, F. & Battaglia, D. Flexible information routing by transient synchrony. *Nat. Neurosci.* **20**, 1014 (2017).
211. McAdams, C. J. & Maunsell, J. H. Effects of attention on orientation-tuning functions of single neurons in macaque cortical area V4. *J. Neurosci.* **19**, 431–441 (1999).
212. Reynolds, J. H., Pasternak, T. & Desimone, R. Attention increases sensitivity of V4 neurons. *Neuron* **26**, 703–714 (2000).
213. Wegener, D., Freiwald, W. A. & Kreiter, A. K. The influence of sustained selective attention on stimulus selectivity in macaque visual area MT. *J. Neurosci.* **24**, 6106–6114 (2004).
214. König, P. & Schillen, T. B. Stimulus-dependent assembly formation. *Neural Comput.* **3**, 155–166 (1991).
215. Singer, W. Synchronization of cortical activity and its putative role in information processing and learning. *Annu. Rev. Physiol.* **55**, 349–374 (1993).
216. Segev, I. & Rall, W. Excitable dendrites and spines: Earlier theoretical insights elucidate recent direct observations. *Trends Neurosci.* **21**, 453–460 (1998).
217. Usrey, W. M., Alonso, J. M. & Reid, R. C. Synaptic interactions between thalamic inputs to simple cells in cat visual cortex. *J. Neurosci.* **20**, 5461–5467 (2000).
218. Engel, A. K., Gerloff, C., Hülsmann, C. C. & Nolte, G. Intrinsic coupling modes: multiscale interactions in ongoing brain activity. *Neuron* **80**, 867–886 (2013).
219. Brosch, M., Bauer, R. & Eckhorn, R. Stimulus-dependent modulations of correlated high-frequency oscillations in cat visual cortex. *Cereb. cortex (New York, NY 1991)* **7**, 70–76 (1997).
220. Legatt, A. D., Arezzo, J. & Vaughan, H. G. Averaged multiple unit activity as an estimate of phasic changes in local neuronal activity: effects of volume-conducted potentials. *J. Neurosci. Methods* **2**, 203–217 (1980).
221. Frien, A., Eckhorn, R., Bauer, R., Woelbern, T. & Gabriel, A. Fast oscillations display sharper orientation tuning than slower components of the same recordings in striate cortex of the awake monkey. *Eur. J. Neurosci.* **12**, 1453–1465 (2000).
222. Supér, H. & Roelfsema, P. R. Chronic multiunit recordings in behaving animals: Advantages and limitations. *Prog. Brain Res.* **147**, 263–282 (2005).
223. Torrence, C. & Compo, G. P. A practical guide to wavelet analysis. *Bull. Am. Meteorol. Soc.* **79**, 61–78 (1998).
224. Tallon-Baudry, C., Bertrand, O., Delpuech, C. & Pernier, J. Oscillatory  $\gamma$ -band (30–70 Hz) activity induced by a visual search task in humans. *J. Neurosci.* **17**, 722–734 (1997).
225. Lachaux, J. P., Rodriguez, E., Martinerie, J. & Varela, F. J. Measuring phase synchrony in brain signals. *Hum. Brain Mapp.* **8**, 194–208 (1999).
226. Carter, G., Knapp, C. H. & Nuttall, A. H. Estimation of the magnitude-squared coherence function via overlapped fast Fourier transform processing. *IEEE Trans. Audio Electroacoust.* **21**, (1973).

## Bibliography

227. Gail, A., Brinksmeier, H. J. & Eckhorn, R. Contour decouples gamma activity across texture representation in monkey striate cortex. *Cereb. Cortex* **10**, 840–850 (2000).
228. Schroeder, C. E., Tenke, C. E., Givre, S. J., Arezzo, J. C. & Vaughan, H. G. Striate cortical contribution to the surface-recorded pattern-reversal vep in the alert monkey. *Vision Res.* **31**, 1143–1157 (1991).
229. Mirabella, G. *et al.* Neurons in area V4 of the macaque translate attended visual features into behaviorally relevant categories. *Neuron* **54**, 303–318 (2007).
230. Desimone, R. Visual attention mediated by biased competition in extrastriate visual cortex. *Philos. Trans. R. Soc. Lond. B. Biol. Sci.* **353**, 1245–1255 (1998).
231. Ni, A. M., Ray, S. & Maunsell, J. H. R. Tuned normalization explains the size of attention modulations. *Neuron* **73**, 803–813 (2012).
232. Zhou, Z., Bernard, M. R. & Bonds, A. B. Deconstruction of Spatial Integrity in Visual Stimulus Detected by Modulation of Synchronized Activity in Cat Visual Cortex. *J. Neurosci.* **28**, 3759–3768 (2008).
233. Kreiter, A. K. & Singer, W. Stimulus-dependent synchronization of neuronal responses in the visual cortex of the awake macaque monkey. *J. Neurosci.* **16**, 2381 LP – 2396 (1996).
234. Maldonado, P. E. Dynamics of Striate Cortical Activity in the Alert Macaque: II. Fast Time Scale Synchronization. *Cereb. Cortex* **10**, 1117–1131 (2000).
235. Kreiter, A. K. & Singer, W. On the Role of Neural Synchrony in the Primate Visual Cortex. *Brain Theory -- Biol. Basis Comput. Princ.* **1**, 201–227 (1996).
236. Battaglia, D. *et al.* Dynamic effective connectivity of inter-areal brain circuits. *PLoS Comput. Biol.* **8**, e1002438 (2012).
237. Vinck, M., Womelsdorf, T., Buffalo, E., Desimone, R. & Fries, P. Attentional modulation of cell-class-specific gamma-band synchronization in awake monkey area V4. *Neuron* **80**, 1077–1089 (2013).
238. Tallon-Baudry, C., Mandon, S., Freiwald, W. A. & Kreiter, A. K. Oscillatory synchrony in the monkey temporal lobe correlates with performance in a visual short-term memory task. *Cereb. Cortex* **14**, 713–720 (2004).
239. Gregoriou, G. G., Rossi, A. F., Ungerleider, L. G. & Desimone, R. Lesions of prefrontal cortex reduce attentional modulation of neuronal responses and synchrony in V4. *Nat. Neurosci.* **17**, 1003–1011 (2014).
240. Masuda, N. Selective population rate coding: a possible computational role of gamma oscillations in selective attention. *Neural Comput.* **21**, 3335–3362 (2009).
241. Vinck, M. & Bosman, C. A. More gamma more predictions: gamma-synchronization as a key mechanism for efficient integration of classical receptive field inputs with surround predictions. *Front. Syst. Neurosci.* **10**, 35 (2016).
242. Martin, A. B. & von der Heydt, R. Spike Synchrony Reveals Emergence of Proto-Objects in Visual Cortex. *J. Neurosci.* **35**, 6860–6870 (2015).
243. Pouzat, C., Mazor, O. & Laurent, G. Using noise signature to optimize spike-sorting and to assess neuronal classification quality. *J. Neurosci. Methods* **122**, 43–57 (2002).
244. Quiroga, R. Q., Nadasdy, Z. & Ben-Shaul, Y. Unsupervised spike detection and

## Bibliography

- sorting with wavelets and superparamagnetic clustering. *Neural Comput.* **16**, 1661–1687 (2004).
245. Nenadic, Z. & Burdick, J. W. Spike detection using the continuous wavelet transform. *IEEE Trans. Biomed. Eng.* **52**, 74–87 (2005).
246. Bankman, I. N., Johnson, K. O. & Schneider, W. Optimal detection, classification, and superposition resolution in neural waveform recordings. *IEEE Trans. Biomed. Eng.* **40**, 836–841 (1993).
247. Yang, X. & Shamma, S. A. A totally automated system for the detection and classification of neural spikes. *IEEE Trans. Biomed. Eng.* **35**, 806–816 (1988).
248. Hulata, E., Segev, R. & Ben-Jacob, E. A method for spike sorting and detection based on wavelet packets and Shannon's mutual information. *J. Neurosci. Methods* **117**, 1–12 (2002).
249. Obeid, I. & Wolf, P. D. Evaluation of spike-detection algorithms for a brain-machine interface application. *IEEE Trans. Biomed. Eng.* **51**, 905–911 (2004).
250. Buzsáki, G. Large-scale recording of neuronal ensembles. *Nat. Neurosci.* **7**, 446 (2004).
251. Lebedev, M. A. & Nicolelis, M. A. L. Brain-machine interfaces: past, present and future. *TRENDS Neurosci.* **29**, 536–546 (2006).
252. Lewis, C. M., Bosman, C. A. & Fries, P. Recording of brain activity across spatial scales. *Curr. Opin. Neurobiol.* **32**, 68–77 (2015).
253. Decharms, R. C., Blake, D. T. & Merzenich, M. M. A multielectrode implant device for the cerebral cortex. *J. Neurosci. Methods* **93**, 27–35 (1999).
254. Galashan, F. O. *et al.* A new type of recording chamber with an easy-to-exchange microdrive array for chronic recordings in macaque monkeys. *J. Neurophysiol.* **105**, 3092–105 (2011).
255. Mendoza, G. *et al.* Recording extracellular neural activity in the behaving monkey using a semichronic and high-density electrode system. *J. Neurophysiol.* **116**, 563–574 (2016).
256. Gold, C., Henze, D. A., Koch, C. & Buzsáki, G. On the origin of the extracellular action potential waveform: a modeling study. *J. Neurophysiol.* **95**, 3113–3128 (2006).
257. Schwartz, A. B. Cortical neural prosthetics. *Annu. Rev. Neurosci.* **27**, 487–507 (2004).
258. Polikov, V. S., Tresco, P. A. & Reichert, W. M. Response of brain tissue to chronically implanted neural electrodes. *J. Neurosci. Methods* **148**, 1–18 (2005).
259. Liu, J. & Newsome, W. T. Local field potential in cortical area MT: stimulus tuning and behavioral correlations. *J. Neurosci.* **26**, 7779–7790 (2006).
260. Katzner, S. *et al.* Local origin of field potentials in visual cortex. *Neuron* **61**, 35–41 (2009).
261. Eckhorn, R. Stimulus-specific synchronizations in the visual cortex: linking of local features into global figures? in *Neuronal cooperativity* 184–224 (Springer, 1991).
262. Eckhorn, R. Principles of global visual processing of local features can be investigated with parallel single-cell-and group-recordings from the visual cortex. in *Information*

## Bibliography

- processing in the cortex* 385–420 (Springer, 1992).
263. Eckhorn, R. & Obermueller, A. Single neurons are differently involved in stimulus-specific oscillations in cat visual cortex. *Exp. Brain Res.* **95**, 177–182 (1993).
264. Self, M. W. *et al.* The effects of context and attention on spiking activity in human early visual cortex. *PLoS Biol.* **14**, e1002420 (2016).
265. Dougherty, K., Cox, M. A., Ninomiya, T., Leopold, D. A. & Maier, A. Ongoing alpha activity in V1 regulates visually driven spiking responses. *Cereb. Cortex* **27**, 1113–1124 (2017).
266. Fiorani, M., Azzi, J. C. B., Soares, J. G. M. & Gattass, R. Automatic mapping of visual cortex receptive fields: a fast and precise algorithm. *J. Neurosci. Methods* **221**, 112–126 (2014).
267. Grabska-Barwińska, A., Ng, B. S. W. & Jancke, D. Orientation selective or not?—Measuring significance of tuning to a circular parameter. *J. Neurosci. Methods* **203**, 1–9 (2012).
268. Grinvald, A., Lieke, E., Frostig, R. D., Gilbert, C. D. & Wiesel, T. N. Functional architecture of cortex revealed by optical imaging of intrinsic signals. *Nature* **324**, 361–364 (1986).
269. Rall, W. Electrophysiology of a dendritic neuron model. *Biophys. J.* **2**, 145 (1962).
270. Lemon, R. & Prochazka, A. *Methods for neuronal recording in conscious animals.* (Wiley, 1984).
271. Gray, C. M., Maldonado, P. E., Wilson, M. & McNaughton, B. Tetrodes markedly improve the reliability and yield of multiple single-unit isolation from multi-unit recordings in cat striate cortex. *J. Neurosci. Methods* **63**, 43–54 (1995).
272. Turner, J. N. *et al.* Cerebral astrocyte response to micromachined silicon implants. *Exp. Neurol.* **156**, 33–49 (1999).
273. Biran, R., Martin, D. C. & Tresco, P. A. Neuronal cell loss accompanies the brain tissue response to chronically implanted silicon microelectrode arrays. *Exp. Neurol.* **195**, 115–126 (2005).
274. Griffith, R. W. & Humphrey, D. R. Long-term gliosis around chronically implanted platinum electrodes in the Rhesus macaque motor cortex. *Neurosci. Lett.* **406**, 81–86 (2006).
275. Lacour, S. P., Courtine, G. & Guck, J. Materials and technologies for soft implantable neuroprostheses. *Nat. Rev. Mater.* **1**, 16063 (2016).
276. Salatino, J. W., Ludwig, K. A., Kozai, T. D. Y. & Purcell, E. K. Glial responses to implanted electrodes in the brain. *Nat. Biomed. Eng.* **1**, 862 (2017).
277. Hubel, D. H. & Wiesel, T. N. Sequence regularity and geometry of orientation columns in the monkey striate cortex. *J. Comp. Neurol.* **158**, 267–293 (1974).
278. Sceniak, M. P., Hawken, M. J. & Shapley, R. Visual spatial characterization of macaque V1 neurons. *J. Neurophysiol.* **85**, 1873–1887 (2001).
279. Ringach, D. L., Shapley, R. M. & Hawken, M. J. Orientation selectivity in macaque V1: diversity and laminar dependence. *J. Neurosci.* **22**, 5639–5651 (2002).

## Bibliography

280. Shapley, R., Hawken, M. & Ringach, D. L. Dynamics of orientation selectivity in the primary visual cortex and the importance of cortical inhibition. *Neuron* **38**, 689–699 (2003).
281. Berlucchi, G. The contributions of neurophysiology to clinical neurology: an exercise in contemporary history. in *Handbook of clinical neurology* **95**, 169–188 (Elsevier, 2009).
282. Humphrey, D. R. Representation of movements and muscles within the primate precentral motor cortex: historical and current perspectives. in *Federation proceedings* **45**, 2687–2699 (1986).
283. Celebrini, S. & Newsome, W. T. Neuronal and psychophysical sensitivity to motion signals in extrastriate area MST of the macaque monkey. *J. Neurosci.* **14**, 4109–4124 (1994).
284. Salzman, C. D., Murasugi, C. M., Britten, K. H. & Newsome, W. T. Microstimulation in visual area MT: effects on direction discrimination performance. *J. Neurosci.* **12**, 2331–2355 (1992).
285. Histed, M. H., Ni, A. M. & Maunsell, J. H. R. Insights into cortical mechanisms of behavior from microstimulation experiments. *Prog. Neurobiol.* **103**, 115–130 (2013).
286. Britten, K. H. & van Wezel, R. J. A. Area MST and heading perception in macaque monkeys. *Cereb. cortex* **12**, 692–701 (2002).
287. Krug, K., Cicmil, N., Parker, A. J. & Cumming, B. G. A causal role for V5/MT neurons coding motion-disparity conjunctions in resolving perceptual ambiguity. *Curr. Biol.* **23**, 1454–1459 (2013).
288. Ranck Jr, J. B. Which elements are excited in electrical stimulation of mammalian central nervous system: a review. *Brain Res.* **98**, 417–440 (1975).
289. Merrill, D. R., Bikson, M. & Jefferys, J. G. R. Electrical stimulation of excitable tissue: design of efficacious and safe protocols. *J. Neurosci. Methods* **141**, 171–198 (2005).
290. Histed, M. H., Bonin, V. & Reid, R. C. Direct activation of sparse, distributed populations of cortical neurons by electrical microstimulation. *Neuron* **63**, 508–522 (2009).
291. Parvizi, J. *et al.* Electrical stimulation of human fusiform face-selective regions distorts face perception. *J. Neurosci.* **32**, 14915–14920 (2012).
292. Tolias, A. S. *et al.* Mapping cortical activity elicited with electrical microstimulation using fMRI in the macaque. *Neuron* **48**, 901–911 (2005).
293. Wagenaar, D. A., Pine, J. & Potter, S. M. Effective parameters for stimulation of dissociated cultures using multi-electrode arrays. *J. Neurosci. Methods* **138**, 27–37 (2004).
294. Schiff, S. J. *et al.* Controlling chaos in the brain. *Nature* **370**, 615 (1994).
295. Wagenaar, D. A. & Potter, S. M. Real-time multi-channel stimulus artifact suppression by local curve fitting. *J. Neurosci. Methods* **120**, 113–120 (2002).
296. Harding, G. W. A method for eliminating the stimulus artifact from digital recordings of the direct cortical response. *Comput. Biomed. Res.* **24**, 183–195 (1991).
297. Erez, Y., Tischler, H., Moran, A. & Bar-Gad, I. Generalized framework for stimulus artifact removal. *J. Neurosci. Methods* **191**, 45–59 (2010).

## Bibliography

298. T O’Keeffe, D., Lyons, G. M., Donnelly, A. E. & Byrne, C. A. Stimulus artifact removal using a software-based two-stage peak detection algorithm. *J. Neurosci. Methods* **109**, 137–145 (2001).
299. Vöröslakos, M. *et al.* Direct effects of transcranial electric stimulation on brain circuits in rats and humans. *Nat. Commun.* **9**, 483 (2018).
300. Heffer, L. F. & Fallon, J. B. A novel stimulus artifact removal technique for high-rate electrical stimulation. *J. Neurosci. Methods* **170**, 277–284 (2008).
301. Wichmann, T. A digital averaging method for removal of stimulus artifacts in neurophysiologic experiments. *J. Neurosci. Methods* **98**, 57–62 (2000).
302. Hashimoto, T., Elder, C. M. & Vitek, J. L. A template subtraction method for stimulus artifact removal in high-frequency deep brain stimulation. *J. Neurosci. Methods* **113**, 181–186 (2002).
303. Montgomery Jr, E. B., Gale, J. T. & Huang, H. Methods for isolating extracellular action potentials and removing stimulus artifacts from microelectrode recordings of neurons requiring minimal operator intervention. *J. Neurosci. Methods* **144**, 107–125 (2005).
304. Fries, P., Reynolds, J. H., Rorie, A. E. & Desimone, R. Modulation of oscillatory neuronal synchronization by selective visual attention. *Science* (80-. ). **291**, 1560–1563 (2001).
305. Miller, C. A. *et al.* Electrical excitation of the acoustically sensitive auditory nerve: single-fiber responses to electric pulse trains. *J. Assoc. Res. Otolaryngol.* **7**, 195–210 (2006).
306. Litvak, L., Delgutte, B. & Eddington, D. Auditory nerve fiber responses to electric stimulation: modulated and unmodulated pulse trains. *J. Acoust. Soc. Am.* **110**, 368–379 (2001).
307. Findlay, J. W. A. & Dillard, R. F. Appropriate calibration curve fitting in ligand binding assays. *AAPS J.* **9**, E260–E267 (2007).
308. Lacouture, Y. & Cousineau, D. How to use MATLAB to fit the ex-Gaussian and other probability functions to a distribution of response times. *Tutor. Quant. Methods Psychol.* **4**, 35–45 (2008).
309. Cohen, J. *Statistical Power for the Behavioural Sciences*. Hillsdale. *NY Lawrence Erlbaum* (1988).
310. Field, A. *Discovering statistics using IBM SPSS statistics*. (sage, 2013).
311. Fries, P. Rhythms for cognition: communication through coherence. *Neuron* **88**, 220–235 (2015).
312. Ni, J. *et al.* Gamma-rhythmic gain modulation. *Neuron* **92**, 240–251 (2016).
313. Briggs, F., Mangun, G. R. & Usrey, W. M. Attention enhances synaptic efficacy and the signal-to-noise ratio in neural circuits. *Nature* **499**, 476–480 (2013).
314. Montijn, J. S., Klink, P. C. & van Wezel, R. J. A. Divisive Normalization and Neuronal Oscillations in a Single Hierarchical Framework of Selective Visual Attention. *Front. Neural Circuits* **6**, 1–17 (2012).
315. Xing, D., Yeh, C.-I., Burns, S. & Shapley, R. M. Laminar analysis of visually evoked

## Bibliography

- activity in the primary visual cortex. *Proc. Natl. Acad. Sci.* **109**, 13871–13876 (2012).
316. Roberts, M. J. *et al.* Robust gamma coherence between macaque V1 and V2 by dynamic frequency matching. *Neuron* **78**, 523–536 (2013).
317. Michalareas, G. *et al.* Alpha-beta and gamma rhythms subserve feedback and feedforward influences among human visual cortical areas. *Neuron* **89**, 384–397 (2016).
318. Miller, E. K. & Buschman, T. J. Cortical circuits for the control of attention. *Curr. Opin. Neurobiol.* **23**, 216–222 (2013).
319. Spaak, E., Bonnefond, M., Maier, A., Leopold, D. A. & Jensen, O. Layer-specific entrainment of gamma-band neural activity by the alpha rhythm in monkey visual cortex. *Curr. Biol.* **22**, 2313–2318 (2012).
320. Popov, T., Kastner, S. & Jensen, O. FEF-controlled alpha delay activity precedes stimulus-induced gamma-band activity in visual cortex. *J. Neurosci.* **37**, 4117–4127 (2017).
321. Clayton, M. S., Yeung, N. & Kadosh, R. C. The roles of cortical oscillations in sustained attention. *Trends Cogn. Sci.* **19**, 188–195 (2015).
322. Jensen, O., Gips, B., Bergmann, T. O. & Bonnefond, M. Temporal coding organized by coupled alpha and gamma oscillations prioritize visual processing. *Trends Neurosci.* **37**, 357–369 (2014).
323. Wegener, D. The influence of sustained selective attention on stimulus selectivity in macaque visual area MT. *J. Neurosci.* **24**, 6106–6114 (2004).
324. Rotermund, D., Taylor, K., Ernst, U. A., Kreiter, A. K. & Pawelzik, K. R. Attention improves object representation in visual cortical field potentials. *J. Neurosci.* **29**, 10120–10130 (2009).
325. Hamlin, H., Rakic, P. & Yakovlev, P. I. Stereotactic imprecision. *Stereotact. Funct. Neurosurg.* **26**, 426–436 (1965).
326. Frahm, J., Haase, A. & Matthaei, D. Rapid three-dimensional MR imaging using the FLASH technique. *J. Comput. Assist. Tomogr.* **10**, 363–368 (1986).
327. Zinke, W. Exploring Cognitive States of the Macaque Monkey with Functional MRI. (2013).
328. Bloyce, A., Qi, P.-Y., Dong, H. & Bell, T. Surface modification of titanium alloys for combined improvements in corrosion and wear resistance. *Surf. Coatings Technol.* **107**, 125–132 (1998).
329. Lausmaa, J. Mechanical, thermal, chemical and electrochemical surface treatment of titanium. in *Titanium in medicine* 231–266 (Springer, 2001).
330. Adams, D. L., Economides, J. R., Jocson, C. M. & Horton, J. C. A biocompatible titanium headpost for stabilizing behaving monkeys. *J. Neurophysiol.* **98**, 993–1001 (2007).
331. Orsini, E. *et al.* Early healing events around titanium implant devices with different surface microtopography: A pilot study in an in vivo rabbit model. *Sci. World J.* **2012**, (2012).
332. Wisbey, A., Gregson, P. J., Peter, L. M. & Tuke, M. Effect of surface treatment on the

## Bibliography

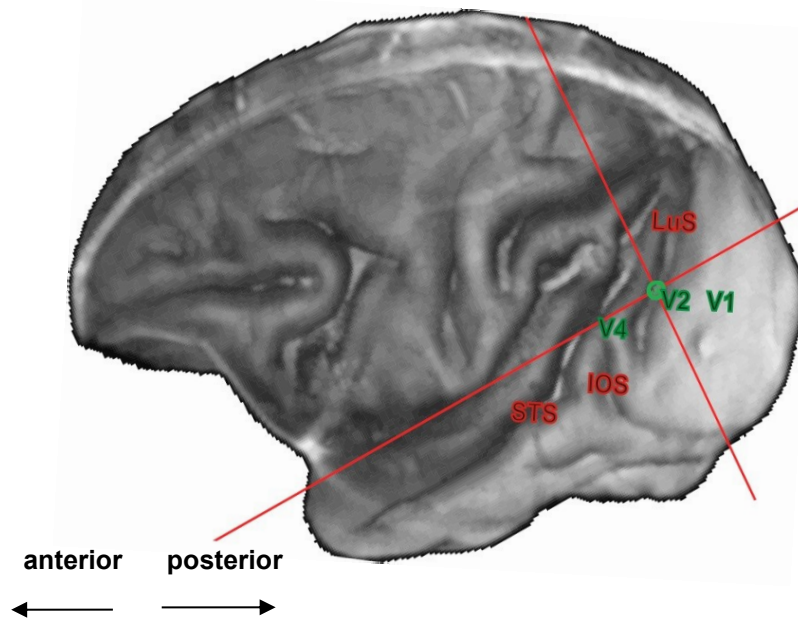
- dissolution of titanium-based implant materials. *Biomaterials* **12**, 470–473 (1991).
333. Vrouwenvelder, W. C. A., Groot, C. G. & De Groot, K. Histological and biochemical evaluation of osteoblasts cultured on bioactive glass, hydroxylapatite, titanium alloy, and stainless steel. *J. Biomed. Mater. Res. Part A* **27**, 465–475 (1993).
334. Fujishiro, Y., Hench, L. L. & Oonishi, H. Quantitative rates of in vivo bone generation for Bioglass® and hydroxyapatite particles as bone graft substitute. *J. Mater. Sci. Mater. Med.* **8**, 649–652 (1997).
335. Friedman, C. D., Costantino, P. D., Takagi, S. & Chow, L. C. BoneSource™ hydroxyapatite cement: a novel biomaterial for craniofacial skeletal tissue engineering and reconstruction. *J. Biomed. Mater. Res. Part A* **43**, 428–432 (1998).
336. Bosetti, M. & Cannas, M. The effect of bioactive glasses on bone marrow stromal cells differentiation. *Biomaterials* **26**, 3873–3879 (2005).
337. Telian, S. A., El-Kashlan, H. K. & Arts, H. A. Minimizing wound complications in cochlear implant surgery. *Otol. Neurotol.* **20**, 331–334 (1999).
338. Cass, S. P. & Mudd, P. A. Bone-anchored hearing devices: indications, outcomes, and the linear surgical technique. *Oper. Tech. Otolaryngol. Neck Surg.* **21**, 197–206 (2010).

### Supplementary Materials and Methods

The supplementary materials and methods chapter contains the description of surgical procedures, and the development of equipment, which are not described in the respective sections of the individual experiments. Nevertheless, they are of substantial relevance for performing them and are described below.

Simultaneous intra-cortical recordings in visual areas V2 and V4, as required for my dissertation project, impose several requirements, as well as restrictions on recording chamber design: (1) Both areas, are located close to each other (SFig. 1), such that only a single chamber can be placed above them. (2) This chamber needs to cover a distance of around 15 mm between recording sites in V4 and V2. (3) The lateral location of area V4 close to the ear impedes a sufficient embedment of the recording chamber in a dental acrylic surround. In conventional recording chamber designs, this dental acrylic surround encloses the actual recording chamber and provides the necessary attachment to the bone. Due to the insufficient space for such surrounds, I could not utilize existing chamber designs. We therefore designed and implanted a cylindrical and biocompatible titanium recording chamber, which was screwed into a trepanation and which does not require any additional dental acrylic surround. The technical specifications of the recording chamber are described in the following subchapter. Supplementary Figure 1 depicts the location of the recording chamber of monkey T, which is part of all studies included in this work. The structural MRI-image (3 T Allegra scanner, Siemens AG, Munich, Germany; 3D reconstruction with left hemisphere shown in front, azimuth: 261°, elevation: 30° with respect to the stereo tactical baseline or Frankfurt line<sup>325</sup>) shows a high resolution (0.25 mm<sup>3</sup> per voxel) image acquired by running multiple FLASH-sequences<sup>326</sup> (fast low angle shot; TR = 25 ms, TE = 2.09 ms, flip angle = 25°, bandwidth = 200 kHz, FoV = 96 mm<sup>2</sup>, matrix size = 192×192, voxel size: 0.25 mm<sup>3</sup>) prior to each recording session for another study performed by Dr. Wolfgang Zinke (for more details see Zinke (2013)<sup>327</sup> pp. 44-46). The green circle represents the midpoint of the subsequently implanted recording chamber, centered above the lunate sulcus (LuS). The figure also illustrates the locations of target areas for intra-cortical recordings (V4 and V2). The planning of recording chamber placement was equal for the second monkey taking part in my experiments.

## Implantation and Development of Recording Chamber



**Supplementary Figure 1:** Anatomical MRI-scan of monkey T brain. Highlighted in red are typical anatomical landmarks of the brain. Visual areas V2 and V4 are the target sites for intracortical recordings and are highlighted in green. The green circle in the midpoint of the red cross depicts the central axis of the recording chamber.

STS: Superior Temporal Sulcus,  
IOS: Inferior Occipital Sulcus,  
LuS: Lunate Sulcus

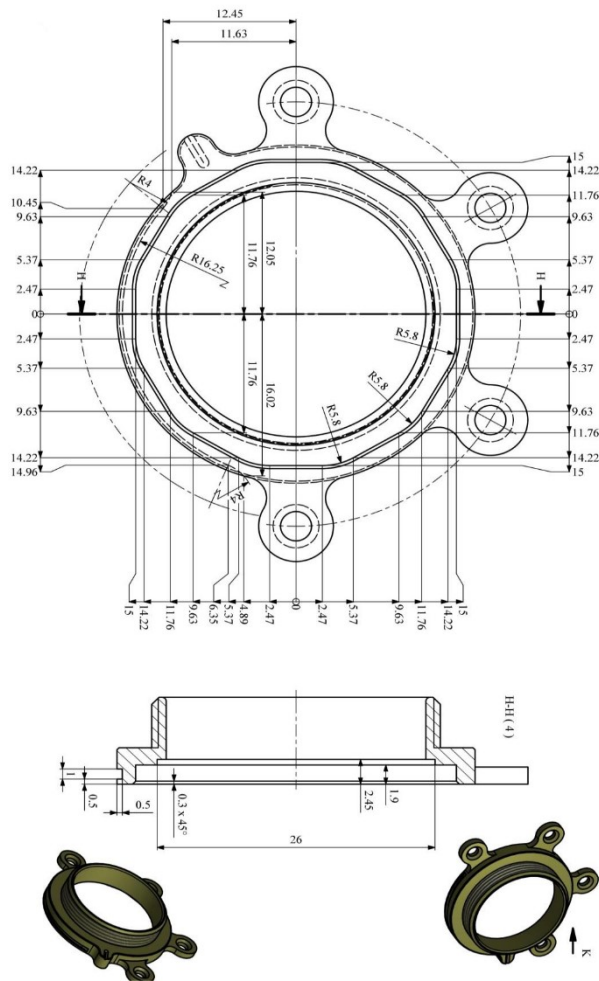
The design of recording chambers differed between animals due to experiences gained after the first implantation. In the following, both designs and surgical procedures will be described. Components differing between animals will be described separately. Otherwise, they were equal for both animals.

As for all experiments and procedures described in this work: The subsequently described experimental and surgical procedures were approved by the local authorities and were in accordance with the regulation for the welfare of experimental animals issued by the Federal Government of Germany and with the guidelines of the European Union (2010/63/EU) for care and use of laboratory animals.

The rationale behind the new recording chamber design was to produce and implant a biocompatible recording chamber, which does not require a dental acrylic surround. The first step of surgery was to perform a circular trepanation (25 mm diameter) above the previously identified areas of interest (SFig. 1, green circle illustrating center of recording chamber and trepanation) with a handheld trepan. Subsequently, a thread (0.7 mm) was cut into the bone using a 26 mm tap. A slightly larger (27 mm including thread, SFig. 2) titanium ring was screwed into the trepanation hole (screw-in ring). The thread of the screw-in-ring was added to the design for increasing the area of contact between bone and titanium and allow for proper bone attachment. Good integration of the titration cylinder into the skull bone



## Supplements



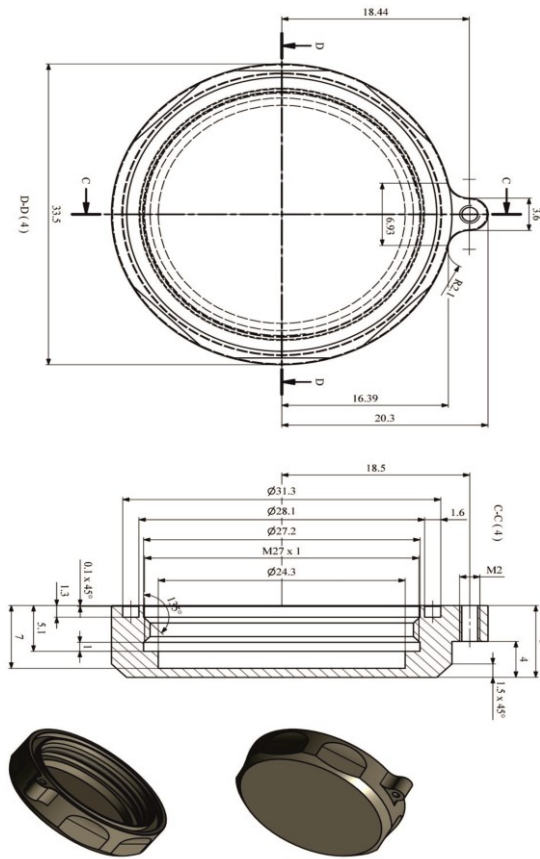
**Supplementary Figure 4:** Titanium ring that was glued on the screw-in ring (SFig. 2). The ring has a polygonal out-cut at the bottom side, which matches the outer edges of the screw-in ring. The six extensions (feet-like structures) contain holes through which bone-screws were inserted and screwed into the bone. The upper sketch is a top view. The middle sketch is a transverse section. The lower two pictures illustrate the final design seen from different angles. All dimensions are given in millimeters.

The technical drawing was made by Martin Nowak. Staff member at the technical workshop, department 2, University of Bremen.

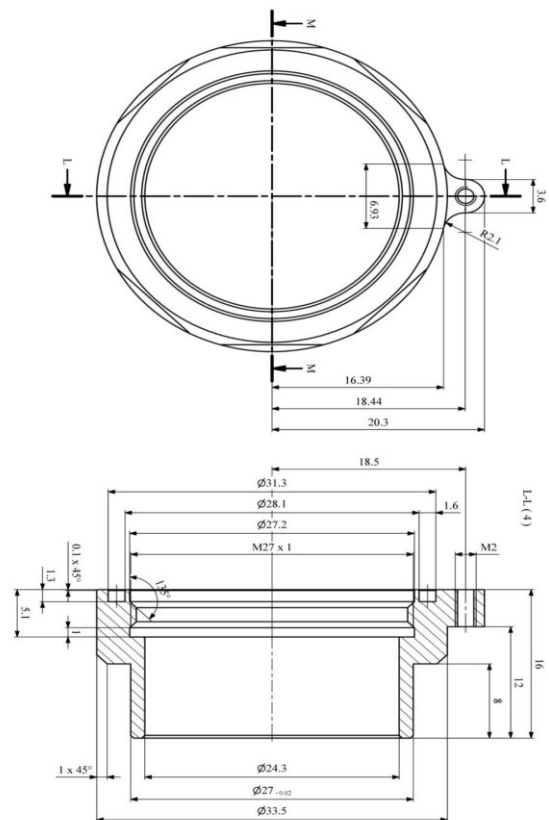
Technology GmbH, Pforzheim, Germany). The plug also contained a surrounding sealing ring (O-ring, 22 x 1 mm, FPM (fluorine caoutchouc), Franz Gottwald GmbH, Bremen, Germany), which fit into the circular groove of the screw-in-ring. The recording chamber was finally closed by a lid, which was fixated with a grub screw (to the second ring, SFig 4, SFig. 5). After

screw-in-ring, was glued during surgery (medical epoxy adhesive; Loctite M-31CL, Henkel Cooperation, Düsseldorf, Germany) onto the screw-in-ring. This second ring contained four “feet”-like structures at its outer edge. Each of these feet had a central hole, through which bone screws (2.7 mm diameter, 8 mm length, cortex screws, DePuy Synthes GmbH, Oberdorf, Switzerland) were screwed into the bone. These screws ensured a fixation of the implant during the period in which the bone contacted the implant. The access to the dura mater was then sealed with a biocompatible rubber plug (polyetheretherketone, product name: TECAPEEK MT blue, Ensinger GmbH, Nufingen, Germany; SFig. 12 B, left plug). This plug had a central hole with a countersinking and a standard M3 thread (metric ISO standard), through which pressure compensation during insertion (and retrieval) was accomplished. After sealing the recording chamber with the rubber plug, the M3-hole was sealed with a standard stainless steel countersunk screw (4 x 6 mm, SFig. 10 B). The length of the screw was adjusted before to the height of the sealing plug. For enhancing the biocompatibility of the screw, it was gold-plated (3 mg Au/l, Haftgoldbad (preplating gold bath) VA JE285, Jentner Plating

## Supplements



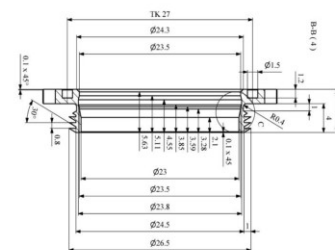
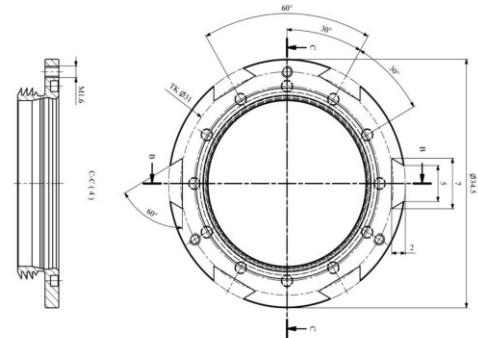
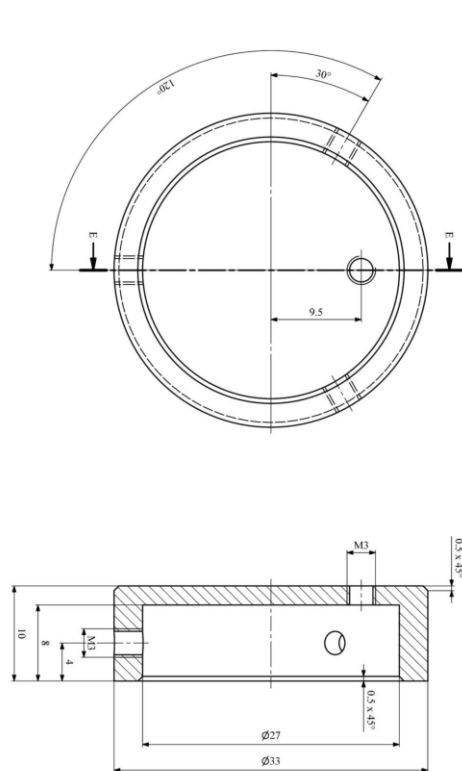
**Supplementary Figure 5:** Titanium lid, which sealed the recording chamber during the healing period. The upper panel shows a top view. The middle panel shows a transverse section (upside-down). The undermost pictures show the final lid design from different angles. To ensure a water tight closure, the lid contained a circular groove at the bottom into which a sealing ring was inserted. The cap was fixated by a topless screw to the rest of the recording chamber. All dimensions are given in millimeters. The technical drawing was made by Martin Nowak. Staff member at the technical workshop, department 2, University of Bremen.



**Supplementary Figure 6:** Adapter for microelectrode-drive. This cylindrical titanium shaft was screwed onto the before implanted recording chamber components (SFig. 4, SFig. 2). The uppermost panel depicts a top view, the bottom panel shows a transverse section (upside-down). The bottom side of the adapter is designed as the lid (SFig 5), with circular groove for inserting a rubber sealing ring. The adapter is fixated with a topless screw to the recording chamber. All dimensions are given in millimeters. The technical drawing was made by Martin Nowak. Staff member at the technical workshop, department 2, University of Bremen.

the implant was fixated and closed by the lid, a smooth slope was formed between the upper edge of the screw-in ring and skull bone using an osteoconductive and osteostimulative synthetic bone graft<sup>333-336</sup>. The bone graft consisted of hydroxyapatite in a polyethylene glycol and glycerin matrix (NovaBone Putty, NovaBone Products LLC, Jacksonville, FL, USA). The synthetic graft delivered a matrix for new formation of bone around the recording chamber. Subsequently, the skin was sutured above the implant. A similar procedure is used when implanting cochlear implants. The advantage of this approach is that beneath the skin, the

## Supplements



**Supplementary Figure 7:** The titanium cap is designed to tightly seal the recording chamber without carrying out rotation forces onto the rest of the recording chamber when opening or closing. The cap is fixated with three headless grub-screws to the recording chamber shaft. An additional hole at the top of the cap serves as opening for pressure compensation. In between recording sessions this hole is closed by a 6 mm M3 stainless-steel screw (Isometric). All dimensions are given in millimeters.

The technical drawing was made by Martin Nowak. Staff member at the technical workshop, department 2, University of Bremen.

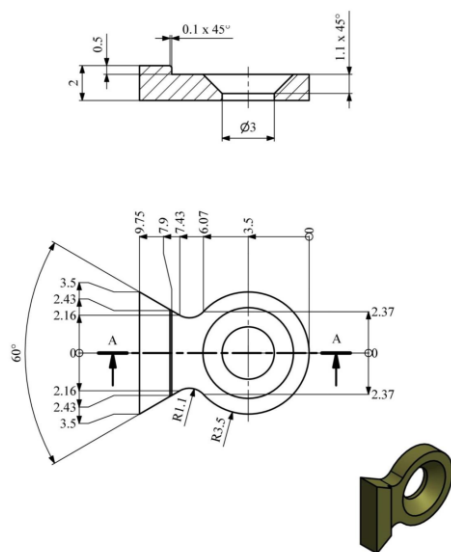
**Supplementary Figure 8:** Revised design of titanium screw-in-ring. The main changes in comparison to the original concept (SFig. 2) are the six dove-tail millings at the outer edges (of the collar) and the six blind holes (upper right panel) into which another component of the recording chamber can be mounted and glued. All dimensions are given in millimeters.

The technical drawing was made by Martin Nowak. Staff member at the technical workshop, department 2, University of Bremen.

implant, bone and contact area is protected from external influences, which helps to prevent bacterial infections<sup>337,338</sup>. After a healing period of three months, the skin was opened, the lid removed, and replaced by a 16 mm high cylindrical shaft also made of titanium (SFig. 6). This shaft is an adapter, which allows mounting of a microelectrode-drive to the recording chamber. It was screwed onto the implant (as the lid) and fixated with a grub screw. The implant (with adapter-shaft) was closed between recording sessions by a titanium lid (SFig. 7), which was plugged on the shaft and fixated with three lateral grub screws (Isometric M3 thread).

This first recording chamber design comprising a second titanium ring (SFig. 4) glued on the

## Supplements



**Supplementary Figure 9:** *Screw holder with dove tail that match the dovetail millings of the screw-in ring (SFig. 7). For the surgery different shaft heights of the dovetail were produced (here an example with 2 mm heights). All dimensions are given in millimeters. The technical drawing was made by Martin Nowak. Staff member at the technical workshop, department 2,*

screw-in-ring (SFig. 2) during surgery and closed by a lid (SFig. 5) formed a cavity below the skin (10 mm height in total). This turned out to impede the healing process.

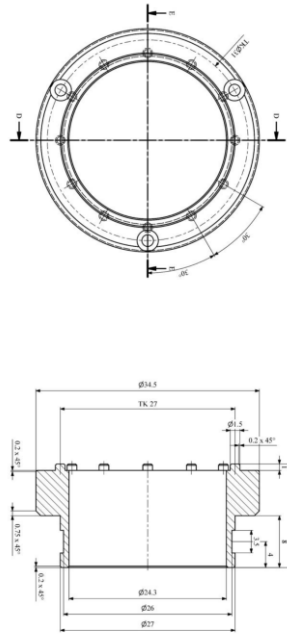
Therefore, I adapted the recording chamber design for the second monkey with a focus on a decreased height of the implant. The changes affected, in particular, the second titanium ring containing the feet-like structures at its outer edge and the thread for the lid. My second design does not contain this component anymore. The revised design of the screw-in ring (SFig. 8) contains six dovetail millings, into which screw holders (SFig. 9) were inserted and then glued using a medical epoxy structural adhesive (Loctite M-31CL, Henkel Cooperation, Düsseldorf, Germany). Different versions of these screw holders were produced, which differed in the height of the dovetail. Screw holder with 2 mm (as depicted in SFig. 9), 2.5 mm and 3.5 mm height were produced.

The heights were adapted to the distance of screw-in-ring to the bone surface (based on anatomical MRI-scans and CRT-scans). Furthermore, the holders were bent to an optimal angle to fit appropriately to the curvature of the skull bone at their planned location (of the screw-in ring). Following the curing of the adhesive, bone screws (2.7 mm diameter, 8 mm length, cortex screws, DePuy Synthes GmbH, Oberdorf, Switzerland) were screwed through the holes of the holders into the skull bone. The procedure to seal the implant was equal to that described above using the biocompatible rubber plug (SFig. 12 B, left blue plug). This second design does not comprise additional sealing by a lid, which decreased the total height of the implant to 2 mm (80 % decrease). The subsequent surgical procedures including artificial bone graft and suturing of the skin, were the same as described above.

This height-reduced implant design was planned without an upper thread. Thus, the adapter shaft for mounting the microelectrode drive had to be fixated differently after the healing period. The redesigned screw-in-ring (SFig. 8) contained 12 blind holes at its surface. Correspondingly, the revised adapter-shaft contained the matching 12 bolts. Furthermore, the

## Supplements

screw-in-ring contained three cannulations with isometric M3 internal thread (SFig 8 lower panel, most lateral holes at 0°, 120°, and 270°). The adapter-shaft contained three continuous cannulations without internal thread at the same locations (SFig 10: upper panel). The shaft was glued onto the screw-in ring with the afore-described medical adhesive, and the 12 bolts delivered additional fixation



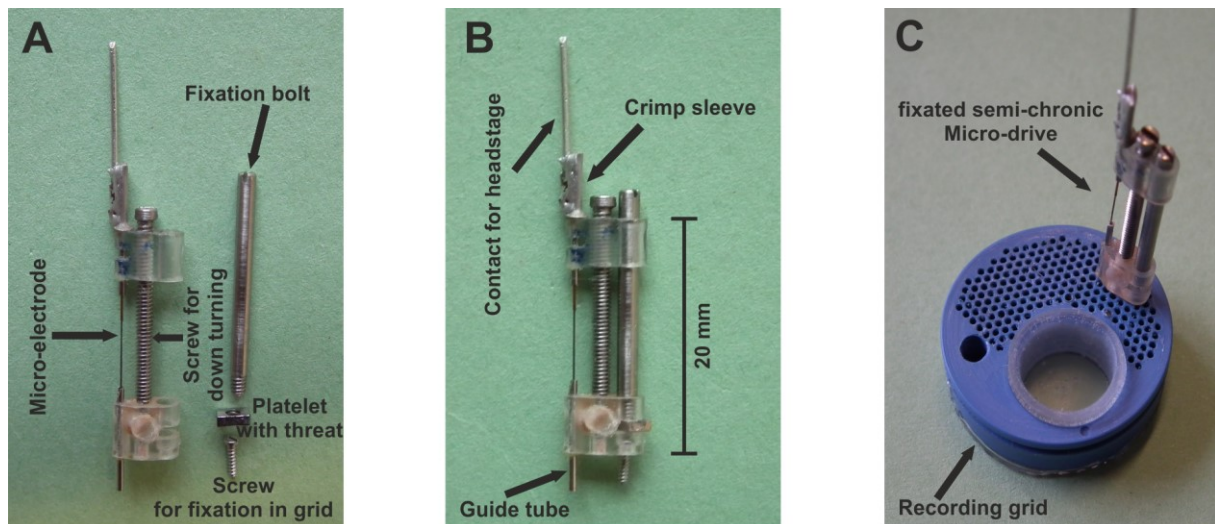
**Supplementary Figure 10:** Revised adapter-shaft design with 12 bolts and three cannulations without internal thread. The adapter-shaft was fixated to the screw-in-ring by adhesive and additionally screwed onto it. The upper sketch is a top view, the bottom sketch a transverse section, seen upside-down). All dimensions are given in millimeters. The technical drawing was made by Martin Nowak. Staff member at the technical workshop, department 2, University of Bremen.

(against shearing forces). Subsequently, three stainless cheese-head screws with internal hex (M 1.6 \*8, isometric) were inserted through the cannulation of the adapter-shaft and screwed into the respective holes with internal thread of the screw-in-ring. As for the first recording chamber design, the implant was closed by a lid between recording sessions (SFig. 7).

## Recording procedure and experimental design

In the following subsection, I will describe the details of semi-chronic recordings using custom-made electrode drives (SFig. 11). The drives were mounted with standard glass insulated tungsten microelectrodes (125  $\mu\text{m}$  diameter, 1 M $\Omega$ , FHC Inc., Bowdoin, ME, USA, SFig 11 A). The micro-drive design is a modified version of drives developed and published in my lab before<sup>254</sup>. Prior to the insertion of these drives, the rubber plug sealing the recording chamber during the healing period (SFig. 12 B, left blue plug) was replaced by a plug designed for simultaneous recordings in area V2 and V4 (SFig. 12 A for a design drawing; SFig. 12 B (right plug) and 12 C for photos, also SFig. 11 C with mounted custom made electrode-drive). This plug contains an array of small holes and a large hole and was made of the same biocompatible material as described before. I will refer to the rubber plug containing the array of 200 holes (0.65 mm diameter, SFig 12) with a center-to-center distance of 1 mm as recording grid. The custom-made micro-drive could be mounted into each of these small holes and fixated using a small self-tapping screw (SFig. 11 A/B; self-tapping, 5/32 Flat Fillister (Unified Thread Standard), JI Morris Company, Southbridge, MA, USA). Supplementary Figure 11C shows a

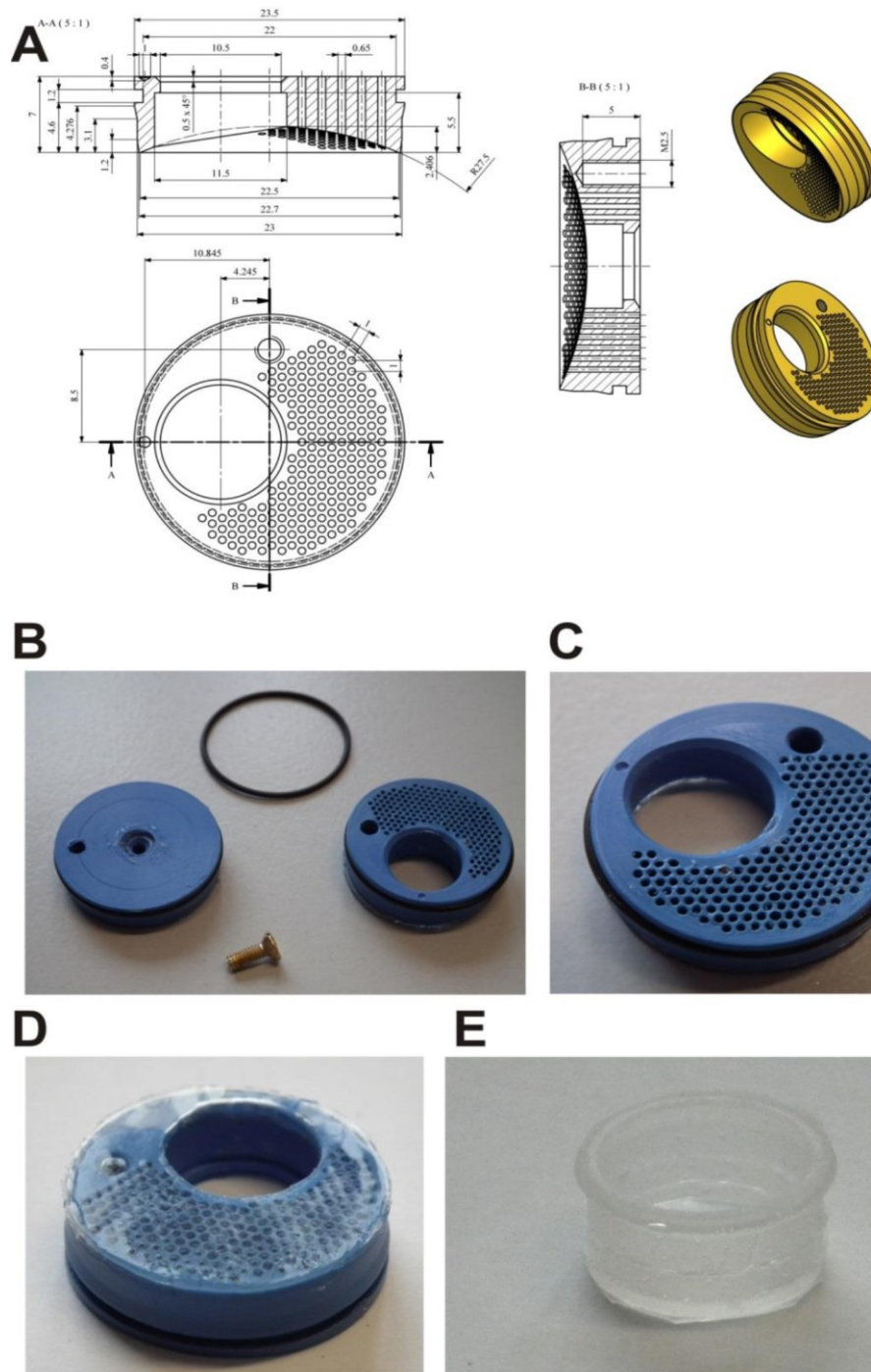
## Supplements



**Supplementary Figure 11:** *Components of the custom made semi-chronic micro-drive and the fixation to the recording grid. A.) Microelectrode drive with its components. The screw for turning down of the upper acrylic glass block was fixated with self-curing acrylic (Paladur, Heraeus Kulzer GmbH, Hanau, Germany) to the lower acrylic glass block. The micro-electrode is mounted and connected via crimp sleeve to a wire nail B.) Shown is the completely assembled micro-drive with the screw for fixation onto the recording grid and the platelet with threads for fixation of the bolt C.) Top-view of a micro-electrode drive inserted into the recording grid. Note, that for fixating the electrode drive to the grid, the bolt needs to be removed first, then the screw can be screwed into the grid. Afterwards the bolt can be inserted again and be screwed into the platelet. The recording grid also contains the silicone plug which is located above area V4.*

custom-made electrode drive (with microelectrode and contact for head-stage) mounted onto a recording grid. The bottom of the recording grid (SFig. 12 D) was sealed using a thin (0.25 mm, transparent) silicone sheeting (BM 20-3020, Bess Medizintechnik GmbH, Berlin, Germany), which was glued onto the grid using a one-component flowable silicone sealant (Dow Corning 734, Dow Corning Corporation, Midland, MI, USA). The silicone film with which grid and silicone sheeting were glued together was maximally 0.25 mm thick. The large hole within the grid providing access to area V4 was cut out of the silicone sheet following the complete hardening of the silicone sealant (SFig 12D). After the recording grid was inserted into the recording chamber, a plug cast from an addition-curing biocompatible silicone (SFig. 12 E SFig 11C; Biopor AB clear X, Dreve Otoplastik GmbH, Unna, Germany) was inserted into the V4 access hole for sealing it. The cast plug was subsequently glued into the grid using the one-component silicone (Dow Corning 734, Dow Corning Corporation, Midland, MI, USA). This replaceable plug ensured easy access to area V4 using an acute FHC-Microdrive system which can move up to 4 microelectrodes independently (FHC Inc., Bowdoin, ME, USA).

## Supplements



**Supplementary Figure 12:** Different versions of rubber plugs for sealing the recording chambers. **A** Technical drawings depicting the dimensions of both types of plugs. Depicted here is the plug used during recording periods with 200 holes for semi chronic recordings and the large hole enabling access to area V4. Note that the technical drawings differs in one aspect from the actually used plugs: The curvature of the bottom-side was not applied during production (as can be seen in D). All dimensions are given in millimeters. **B** Photo of both types of rubber plugs, either used during recording sessions (right) or healing period (left). Also depicted are the sealing O-ring (top) with which a tight closure of the recording chamber was achieved, as well as the screw with which the pressure compensation hole during healing period was sealed (bottom). **C** Rubber plug used during recording periods with mounted O- ring. **D** The surface contacting the dura was covered by a thin silicone sheet, of which the V4 hole was cut out. **E** The V4 hole was later sealed by a cast plug consisting of silicone and glued into the rubber plug with silicone.

The technical drawing was made by Martin Nowak. Staff member at the technical workshop, department 2, University of Bremen.